Development of Metamaterials for a Custom-fit Bicycle Helmet Liner

Submitted by: M.T. Moester S2639572
University of Twente, Engineering Technology (ET)
Department of Design, Production and Management (DPM)
Drienerlolaan 5, 7522NB, Enschede, The Netherlands
E-mail: m.t.moester@student.utwente.nl

October 27, 2022

Master Thesis

in partial fulfilment of the requirements for the degree of

Master of Science
in Mechanical Engineering
at the University of Twente department of Engineering Technology

UNIVERSITY OF TWENTE.

Examination committee:

Prof. Dr. I. Gibson	Advanced Manufacturing Sustainable Products & Energy Systems	Chair
Dr.Ir. M. Mehrpouya	Advanced Manufacturing Sustainable Products & Energy Systems	UT Supervisor
Dr.Ir. D.P. Saakes	Interaction Design	UT Supervisor

Acknowledgements

This thesis marks the end of my career as a student. The last 8 years have been quite the journey, with many ups and downs. These moments helped me improve myself and made me the person I am today. I am very proud of this work, however, I could not have done this by myself. I would like to express my great appreciation to Dr Mehrshad Mehrpouya and Dr Daniel Saakes, my research supervisors, for their encouragement and guidance during this research work. The time and patience they showed throughout the sessions, as well as the insightful criticisms, were essential. Their high standards have made me better at what I do. Additionally, I want to thank Jan te Kulve and Bert Vos for their assistance during the 3D scanning and all the experimental tests.

Last but not least, I would like to thank my family for making this all possible and for their incredible support throughout my life. To Aniek, my girlfriend, thank you for all your love and support. Also, special thanks to all my friends, who have been there whenever I needed them.

Max Moester
October 2022, Winterswijk, The Netherlands

Abstract

Cyclists are still one of the most vulnerable road users and have a considerable higher fatality rate than other road users. Therefore, the bicycle helmet was introduced in 1975, to provide the user head protection. Although bicycle helmets have been around for almost 50 years, the process to manufacture the helmets, and the approach to protect the human head, have undergone only minor changes. To date, the majority of the bicycle helmet liners are still manufactured with expanded polystyrene (EPS) foam. However, the foam is limited for energy absorption optimization due to its mechanical properties. Furthermore, the EPS liners are made for single impact events and can not undergo multiple impacts at the same location. Large impact energies permanently deform the EPS liner after which the helmet must be discarded as it can no longer provide sufficient protection. The current helmets are commonly available in four standard sizes. However, in reality, every human head has its unique shape and dimensions. As a result, the improper fit causes discomfort and results in a reduction of the protection capabilities. A unique design was necessary to allow additional room for the liner's performance while also increasing the helmet's fit. Moreover, a design that was able to undergo multiple impacts while providing the same specific energy absorption. In this work, the origami-based metamaterial: Miura-Ori was investigated. It presented promising energy absorption capabilities and allowed more room for optimization. The design of the metamaterial was realized by creating a parametric design model based on Taguchi's method L9. Nine distinctive samples were realized and additively manufactured via fused deposition modelling. The filament material, thermoplastic polyurethane, offered high specific energy absorption and allowed recoverable deformation. Prior to additive manufacturing, three geometrical parameters were selected: wall thickness, dihedral angle and cell wall ratio to investigate their influence on the energy absorption capabilities. This was accomplished by compressing the samples, out-of-plane, quasi-statically at a fixed strain rate. For improving the fit, 3D scanning equipment was used to capture the unique shape and dimensions of the human head. The 3D scans provided the fundamentals for the surface of the helmet liner. The final design presented a novel helmet liner that was able to undergo multiple impacts while offering recoverable specific energy absorption. Moreover, it offered more scope for optimization and the design demonstrated to provide an improved fit of the bicycle helmet.

Contents

List of Figures

List of Tables

Nomenclature

ECF	European Cyclists' Federation
TBI	Traumatic Brain Injury
PC	Polycarbonate
ABS	Acrylonitrile Butadiene Styrene
WHO	World Health Organisation
EPS	Expanded Polystyrene
AM	Additive Manufacturing
FDM	Fused Deposition Modeling
TPU	Thermoplastic Polyurethane
TPEs	Thermoplastic Elastomers
PPE	Personal Protective Equipment
PU	Polyurethane
PVC	Polyvinyl Chloride
MO	Miura-Ori
MOM	Miura-Ori Metamaterial
PLA	Peak Linear Acceleration
SEA	Specific Energy Absorption
a	Cell Wall Length a
b	Cell Wall Length b
t	Cell Wall Thickness
θ_A	Dihedral Angle
a/b	Cell Wall Ratio a/b
CWR	Cell Wall Ratio
TPU85A	NinjaFlex 85A
DoE	Design of Experiments
RE	Reverse Engineering
CAD	Computer Aided Design
STL	Standard Triangle Language
NURBS	Non-Uniform Rational B-Splines
GH	Grasshopper
Rhino	Rhinoceros 3D
S/N	Signal-to-Noise Ratios
α	Folding Angle
L9	Three-level Orthogonal Array
ANOVA	One-way Analysis of Variance
SS	Sum of Squares
MS	Group Means
D	Total Thickness Helmet Liner
C_T	Total Number of Cells
C_Y	Total Number of Cells in Y-direction
C_Z	Total Number of Cells in Z-direction
FFV	Force-Fitted Value
IV	Initial Value
PLA	Polylactic Acid
SOD	Standoff Distance
E_E	Existing E-steps
E_O	Optimised E-steps
L_R	Requested Length
L_A	Actual Length
FR_N	New Flow Rate
t_T	Target Thickness
t_M	Measured Thickness
ϵ_d	Densification Strain
ϵ_c	Compressive Strain
EA	Energy Absorption

σ_{eng}	Engineering Stress
F	Force
A_0	Original Area
ϵ_{eng}	Engineering Strain
δ_L	Displacement of Internal System
L_0	Height of the Sample
$\eta_E A$	Energy Absorption Efficiency
σ_{max}	Maximum Applied Stress before Densification
ODS	Onset Densification Strain
L	Length of Sample
H	Height of Sample
FD	Force-Displacement
$\rho*$	Relative Density
ρ_m	Cellular Density
ρ_s	Solid Density
EAE	Energy Absorption Efficiency

1 Introduction

The current coronavirus epidemic has resulted in a huge rise in cyclists, and European cities have spent about €1 billion on establishing additional cycle lanes, car-free streets, and improved traffic controls, according to the European Cyclists' Federation (ECF) [6, 7]. In general, cycling brings many positive benefits such as physical, social and mental health [8, 9]. Despite the benefits, unwanted actions can occur during cycling. To date, cyclists are still one of the most vulnerable road users and therefore more prone to severe injuries. Moreover, they have a considerable higher fatality rate than other road users [10]. The head is the most commonly injured part of all serious injuries [11]. For instance, in Germany, head related injuries were responsible for 23% of the reported cycling injuries [12]. Approximately, 40% of these cyclists did not wear a helmet. Prior research indicated that 48% of the non-helmeted cyclists suffered severe traumatic brain injury (TBI) [13]. It is the most serious injury and the leading cause of mortality, although surviving such an injury can result in lifelong neurological damage [10, 14].

In general, there is minimal protective equipment available for riders, but the bicycle helmet is the most significant. It was first introduced in 1975 and its main objective is to protect the human head. The design is built on four primary components: the chinstraps, an exterior shell that is relatively thin and often composed of polycarbonate (PC) or acrylonitrile butadiene styrene (ABS), detachable comfort padding, and the liner of the helmet [15]. The latter one being the most important part of the helmet and is often a deformable structure. Moreover, it is the part that is responsible for absorbing the majority of the impact energy. During a bicycle incident, the outer shell is the first part to encounter the impact energy and helps to spread the load by increasing the contact area. Subsequently, the compressive stress acting on the inner liner is decreased and as a result, the absorption of the impact energy is enhanced [16]. Since the introduction of bicycle helmets, the severity of head injuries have reduced significantly [17, 18]. These reductions can be identified as 51% reduction for head injuries and 69% for fatal head injuries [19]. Therefore, wearing helmets is endorsed by the World Health Organization (WHO) [20].

Although bicycle helmets have been around since the early 70s, the process to manufacture the helmets, and the approach to protect the human head, have undergone only minor changes. For instance, the helmet liners are still manufactured with material such as Expanded Polystyrene foam (EPS) [10, 21]. Additionally, the current procedure for sizing of helmets is not able to provide good fit for all users [22]. Cyclists from all over the world are limited to three to four helmet sizes that are purely based on mannequins called headforms [23]. However, in reality, every human head has its unique shape and dimensions. An uncomfortable fit can result in a considerable decrease in the protection provided by the human head, or poorer energy absorption [24]. Regarding the EPS foam, its high weight to performance ratio and low cost of manufacturing are the main reasons that manufactures are still utilising the material [25]. Although EPS is capable of providing sufficient protection, it has some drawbacks. The compression of the EPS, that occurs during a large impact, is irreversible. Therefore, the helmet is no longer able to absorb a following impact and its impact energy [16]. Subsequently, cyclists will unknowingly use helmets that should have been discarded. It is an unwanted situation as the helmets no longer provide the right head protection. Additionally, EPS has limitations for maximizing the specific energy absorption and undergoing multiple impacts at the same location.

The use of EPS, in combination with the current sizing approach, in bicycle helmets makes them limited for optimization for both the fit and protection. Hence, new emerging materials and structures were developed and applied to helmets, to improving the fit and optimise the energy absorption. Regarding the optimization of energy absorption, materials such as origami-based [26], (auxetic) metamaterials [27] and viscoelastic materials [28] were adapted into the helmets. The conventional manufacturing methods are not able to manufacture such complex geometries. Hence, novel methods were introduced that enabled the manufacturing of these materials and structures. It included methods such as 3D scanning [29] and additive manufacturing (AM) [30]. The usage of the latter method, fused deposition modelling (FDM), in particular, has significantly increased in the last couple of years. It has proven to be a low-cost solution that is capable of rapid prototyping functional parts while presenting a high accuracy and quality [31].

The FDM technique enables the use of a wide variety of base materials to manufacture functional products. One such material is thermoplastic polyurethane (TPU) that originates from thermoplastic elastomers (TPEs), which are known as a mix of polymers [16]. TPEs, or thermoplastic and elastomeric materials, have special qualities that offer a number of interesting material attributes. For example, it has excellent abrasion resistance and high flexibility but also high impact strength and a low relative density [32]. It is able to recover its deformation after which it can provide the same specific energy absorption. Furthermore, TPU has already been used in many different personal protective equipments (PPE) [30, 33, 34]. Moreover, it has proven to be a promising material for the manufacturing of helmets [35]. The fit and the impact absorption of a bicycle helmet are strongly connected to the bicycle helmet liner. Therefore, it is anticipated that a custom-fit and practical substitute for the EPS liner may be produced by enhancing the present design methodology, leveraging FDM and 3D scanning technologies, and adopting new developing materials.

1.1 Research Aim

The aim of this study can be described as two study goals. (1) To develop a novel method to improve the fit of the bicycle helmet and (2) To design a Miura-Ori metamaterial based helmet liner. The first part can be achieved by utilizing the novel approach of a 3D scanner equipment and reverse engineering. The second goal can be reached by leveraging the advantages of the Miura-Ori metamaterial and additive manufacturing.

1.2 Research Scope and Objectives

1.2.1 Research Scope

This study solely focuses on the design of the bicycle helmet liner; the outer shell and helmet straps are not considered. In terms of needs, this research does not include aerodynamics, aesthetics, heat transfer, or manufacturing costs. Furthermore, the helmet liner design is based on a single human head; nonetheless, the research gives a design foundation for others to follow. Additionally, no research has been conducted to determine which regions of the human head must be covered. The fused deposition modelling (FDM) technology is utilized in additive manufacturing. Experiments are carried out to explore the energy absorption capacities and the behavior of the helmet liner (i.e. quasi-static compression tests). This means that only pure compression is investigated and no research to tangential forces or translational accelerations. Subsequently, just a portion of the helmet liner is examined, not the entire helmet liner. Furthermore, numerical simulations are not performed and are outside the scope of this study. Finally, the final prototype is created using the FDM process and has the ideal structure as well as a simpler, tougher outer shell.

1.2.2 Research Objectives

To achieve the research aim indicated in section 1.1 and in accordance with the scope of the research, the following research objectives are described:

- Develop a design framework to capture the unique shape and dimensions of the human head.
- Develop a parametric design model to create the Miura-Ori metamaterial structures.
- Demonstrate the use of fused deposition modelling for manufacture the Miura-Ori metamaterial samples and final prototype.
- Experimentally test the Miura-Ori metamaterial to investigate the energy absorption capabilities.
- Use optimization methods to select the optimal set of geometrical parameters for the Miura-Ori metamaterial.
- Fabricate a prototype bicycle helmet including a helmet liner.

1.3 Research Outline

This research is broken into seven sections. Section 1 summarizes the research endeavor and its primary goals. Section 2 contains a thorough overview of the literature relevant to this argument. Section 3 describes many strategies that aided in the achievement of the objectives. These involve reverse engineering to get the unique head form and proportions, specifying the helmet liner surface, and designing experiments for the structural samples. Furthermore, the Miura-Ori metamaterial creation is described. Section 4 contains the experimental design for investigating the samples' energy absorption capacity. Additionally, a technique for post-processing the collected data is given, including computations and statistical analysis. Section 5 explains the outcomes of achieving the objectives. The parametric model, additive created structures, experimental findings, and prototype are all presented. Likewise, discussions about the outcomes are addressed. Section 6 summarizes the significant scientific contributions noted during the investigation and concludes with limits and recommendations for further development. The final section 7 is responsible for the appendices where the complete grasshopper models and additional figures are presented.

2 Background and Literature Review

2.1 Background of the Bicycle Helmet

The earliest bicycles were made available in the 1870s; they were high wheel bicycles with a huge front wheel and a tiny back wheel, see Fig. 1a. The people fell from their bicycle from a considerable height since it had a high saddle. As a result, many cyclists were severely injured and realized that there was a need for head protection. This moment sparked the idea for the first helmets. They were made from a crushable material and broke at impact [1]. It took approximately 100 years for a new design, a leather helmet, to be presented, see Fig. 1b. This helmet improved the durability and offered better protection, but almost no impact energy absorption [36]. The first helmets with a good energy absorption system started to appear about 1975. Expanded polystyrene (EPS) foam and a tougher outer polycarbonate shell were used to create the helmet, see Fig. 1c. Although it was the first bicycle helmet to be able to absorb some impact energy, the design was not optimum, and it was exceedingly heavy. This implied that lighter materials, like plastics, were required. Thus, in the latter part of the 1990s, thin, rigid plastic casings were developed. After being created by injection molding, the EPS foam was added to the shell, see Fig. 1d. This resulted in a light helmet that provided sufficient head protection. This marked the beginning of the modern bicycle helmets. Throughout the years, the general purpose of bicycle helmets stayed the same; providing sufficient head protection and preventing head injuries. Now, almost 50 years later, helmets have significantly changed in terms of aesthetics, aerodynamics and weight [37]. However, the majority of the helmet liners are still manufactured with the EPS foam.

Figure 1: The first ever head protection for high wheel bicycles [a], the leather striped bicycle helmet [b], the first EPS foam based bicycle helmet from Bell [c] and the current bicycle helmet made from EPS foam with a thin, harder outer shell [d]. Adopted from [1].

2.1.1 Bicycle Helmet Structure

To date, bicycle helmets consists of four main parts: the harder outer shell, the helmet liner, removable comfort paddings and the chinstraps [37]. In Fig. 2, an overview of a bicycle helmet with the above-mentioned parts is depicted. The outer shell is often manufactured from harder plastics such as Polycarbonate (PC) or Acrylonitrile Butadiene Styrene (ABS) [15]. Its main function can be described as enclosing the helmet liner. Moreover, during a bicycle incident, the outer shell is the first part to encounter the impact energy and helps to spread the load by increasing the contact area [16]. Moreover, it has a protective function to shield the helmet liner from getting damaged. The next part, the helmet liner, can be seen as the most important part of a bicycle helmet. The majority of the liners are still made from the EPS foam and act as the main energy absorption mechanism. Its primary function is to absorb the residual impact energy after it has been partly absorbed by the outer shell. The current EPS liners vary in thickness and type of foam, to optimize the weight and energy absorption of the bicycle helmets [10, 37]. Regarding the EPS foam, its high weight to performance ratio and low cost of manufacturing are the main reasons that manufactures are still utilizing the material [25]. Although EPS is capable of providing sufficient protection, it has some drawbacks. The compression of the EPS, that occurs

Figure 2: Overview of the main parts in a bicycle helmet.

during a large impact, is irreversible. Furthermore, if the impact occurs at the same location, the helmet is no longer able to absorb a following impact and its impact energy [16]. Subsequently, cyclists will unknowingly use helmets that should have been discarded. It is an unwanted situation as the helmets no longer provide the right head protection. Additionally, EPS has limitations for maximizing the specific energy absorption and undergoing multiple impacts at the same location. Hence, new emerging materials were invented and will be discussed in section 4. To assure that the helmet stays fixed on the human head during cycling, chinstraps have been invented. The straps are implemented into the helmet and can be closed by the buckle at the end of the strap. It is a reliable system that has low manufacturing costs, easy to open and close and can be adjusted to preference. Therefore, it is used for almost every bicycle helmet. The last part of the helmet are the removable comfort paddings. They provide the user some comfort to fill the gaps between the human head and the helmet liner. Usually constructed from soft foams like polyurethane (PU) foam or polyvinyl chloride (PVC), it is then tucked away under fabric padding [38]. They can be inserted or removed from the helmet to the preference of the user. It has no further function and has no influence on the energy absorption capabilities of the helmet.

2.1.2 Bicycle Helmets Sizing

Bicycle helmets are used worldwide, and each continent enforces its own safety standards. Currently, five international standards for bicycle helmets can be identified: AS/NZS-2512 (Australia), ASTM-F1447 and Snell B-95 (United States), CPSC (International) and the EN-1078:2012+A1 (Europe). Table 1 shows the agreements or differences in each standard with its own specific requirements. It is interesting to see that each standard must use another standard for the use of the head forms. It specifies the dimensions of the headforms that must be used while conducting the tests. Moreover, it forms the fundamentals for the design of the helmet liner [1]. The headforms within each standard were invented to represent the head dimensions and shapes of its continent. For instance, the headform of the European standard EN-960 is depicted in Fig. 3. The standard presents a list of head circumferences that correspond to the helmet sizes. In practice, these models should represent the entire target population. However, in reality every human head has its unique shape and dimensions, and therefore causes improper and poor helmet fit [39]. There are more sizes available, both bigger and smaller, but are often not produced due to the high manufacturing costs. Thai et al. discovered that the shape and dimensions of a human head are related to age, gender and ethnic background [40]. In fact, the majority of the bicycle helmets are manufactured for the Western market and therefore cause improper fit for Asian users. To see what was causing

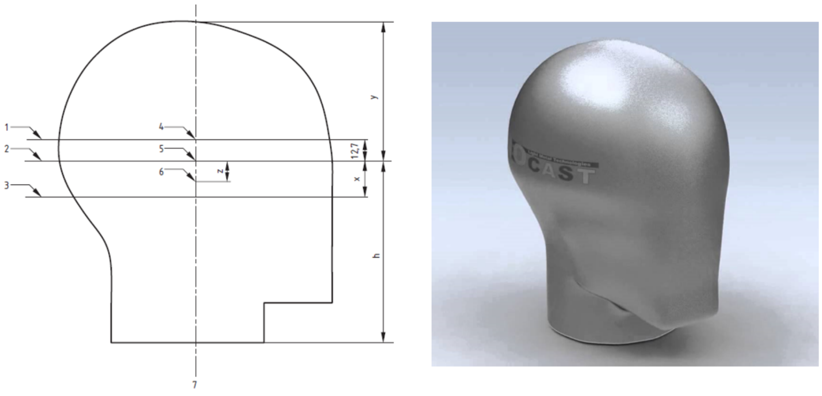

[a] [b]

Figure 3: The headform adopted from the European standard EN-960 [2]

this improper fit, Ball et al. compared the Asian head shapes to Caucasian head shapes [3]. They concluded that despite having the same head circumference, the shapes were unique, see Figure 4. Asian heads present a round shape, whereas Caucasian heads present a more oval shape. Moreover, the front and back of the heads differ greatly. This shows that the current bicycle helmets, which are only based on the head circumference, are not able to fit all the unique head shapes.

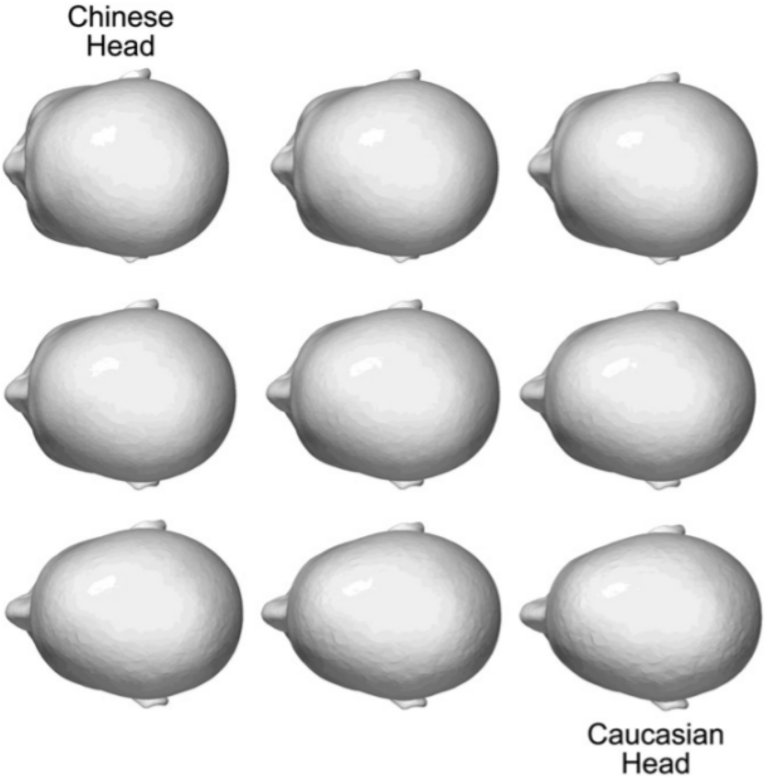

Figure 4: Comparison of the Asian and Caucasian head shapes adopted from [3].

Table 1: Comparison of International Safety Standards for Bicycle Helmets

Requirements	**AS/NZS-2063:2020** [41]	**ASTM-F1447** [42]	**EN-1078:2012+A1** [43]	**CPSC** [44]	**Snell B-95** [45]
Status	2020	2018	2012	1999	1995
Anvils	Flat (F)	Flat, Hemispherical and Kerbstone (F, H and K)	Flat and Kerbstone (F and K)	Flat, Hemispherical and Kerbstone (F, H and K)	Flat, Hemispherical and Kerbstone (F, H and K)
Drop Technique	Twin-wire drop rig	Guided free fall: wire, monorail or twin-wire	Guided free fall: twin- or triple-wire	Guided free fall: twin-wire or monorail	Guided free fall: two or more wires, one or more rails
Drop Height	1.45 and 1.80 m	2.0 m (F), 1.2 m (H and K)	1.5 m (F and K)	2.0 m (F), 1.2 m (H and K)	2.2+ and 2.0+ m (F), 1.3+ m (H and K)
Peak Acceleration	< 300 g < 200 g for 3.0 m/s < 150 g for 6.0 m/s	< 300 g for 6.2 m/s (F), 4.8 m/s (H and K)	< 250 g	< 300 g for 6.2 m/s (F), 4.8 m/s (H and K)	< 300 g for 100 and 110 J (F) < 300 g for 65 and 72 J (H and K)
Mass	< 700 gram	Light weight is desirable	Low weight and must be labeled on helmet	N/A	N/A
Field of Vision	Horizontally: min. 105 degrees from the longitudinal vertical median plane for both sides Front edge: 25 mm clearance above the basic plane	Horizontally: min. 105 degrees from the longitudinal vertical median plane for both sides	Horizontally: min. 105 degrees from longitudinal vertical median plane for both sides Upwards: min. 25 degrees from the reference plane Downwards: min. 45 degrees from the basic plane	Horizontally: min. 105 degrees from the longitudinal vertical median plane for both sides	Horizontally: min. 110 degrees from the longitudinal vertical median plane for both sides Upwards: min. 40 degrees from the reference plane
Strap Durability	N/A	N/A	Straps must maintain tension and be openable with one hand	N/A	N/A
Head Forms	AS-2512.1	ASTM-F2220	EN-960	ISO-DIS 6220-1983	ISO-DIS 6220-1983
Ventilation	Helmets should include features to transfer heat away from the head	Ventilation is desirable	Helmet should be ventilating, no additional measurements	N/A	N/A
Accessories	Spectacles permitted	Spectacles optional	Spectacles must be usable	Spectacles must be usable	Spectacles permitted

2.1.3 Bicycle Helmet Usage and Barriers

The use of bicycle helmets in Europe has been studied in greater detail to better understand how they fit. Furthermore, several barriers have been identified that causes users to not wear their helmets. Bicycle helmet adoption is still low, despite the fact that it offers the necessary protection in the case of a crash or accident while cycling and considerably lowers the risk of head injuries. A study done by DEKRA Accident Research [4] showed that the bicycle helmet use in Europe varies greatly, see Figure 5. The study focused on nine bicycle friendly European capitals. Two cases that stand out are Amsterdam and London, their helmet use rates are 1.1% and 60.8%, respectively. All other studied capitals show a similar rate, with an average of 18.25%. According to DEKRA, the high rate in London can be explained by the road situation. In London, all road users need to share the road and thus making cyclists the most vulnerable users [46]. For Amsterdam, however, it is interesting to see that together with Copenhagen both are known for their well-planned cycling infrastructure but show different helmet use rates. The Netherlands is known as the bicycle nation of the world [47]. As a result, a culture of bicycling has emerged, demonstrating Dutch people's confidence in both the bike infrastructure and their own abilities. As a result, Dutch cyclists do not feel the urge to wear a bicycle helmet. For Denmark, the higher rate in Copenhagen could be due to the many promotional campaigns that have been presented by the Danish Ministry of Transport during the last couple of years [48].

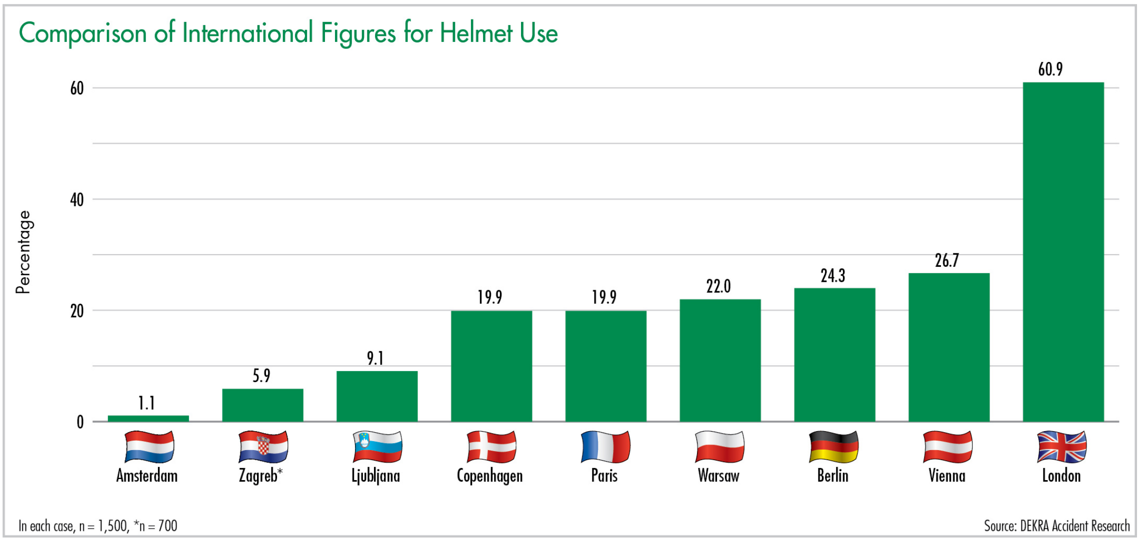

Figure 5: Overview of helmet use in the most bicycle friendly capitals in Europe, adopted from [4].

The explanations described above show that there is still no significant evidence of the low helmet use. Hence, other studies investigated the barriers for not wearing a bicycle helmet. For instance, Villamor et al. investigated the reasons behind the Dutch people not wearing a helmet [49]. They concluded that the main barrier was the discomfort of the bicycle helmets. Moreover, multiple studies confirmed that the majority of cyclists are reluctant to wear a bicycle helmet due to the discomfort [50, 51, 52]. This suggests that the low utilization rate can be due to discomfort. Fit, thermal comfort, and weight are a few elements that affect how comfortable something feels [53]. The fit of bicycle helmets is still a concern, despite the fact that the previous two have significantly improved in recent years [40]. A study done by Romanow et al. concluded that the fit of bicycle helmets has impact on its protection capabilities [54]. For instance, if the helmet is too large and does not match the shape of the head. As a result, it could fall off the head during an accident and leave the head unprotected. The use of the EPS foam in combination with the current sizing procedure suggest that there is need for a novel bicycle helmet liner. One that presents more scope for optimizing the energy absorption capabilities provides more comfort and, more importantly, increases the adaption of the bicycle helmets. To date, many attempts have been made, see table 2.

Table 2: Overview of previous works to improve the energy absorption capabilities or overall fit of the bicycle helmets.

Description	**Improvement**	**Base material**	**Structure**	**Manufacturing method**	**Year**	**Ref.**
Bicycle helmet with IMPAXX foam liner	EAC	Cellular	Closed cell foam	-	2013	[55]
Sport helmet with auxetic foam	EAC	Cellular	Auxetic open cell foam	-	2018	[56]
Bicycle helmet with Wavecell liner	EAC	Cellular copolymer	Wavecell	-	2019	[57]
Bicycle helmet with honeycomb liner	EAC	PETg and ABS	Honeycomb	Additive manufacturing: FDM	2020	[58]
Bicycle helmet with lattice liner	EAC	TPE Duraform Flex	Lattice	Additive manufacturing: SLA	2015	[16]
Bio-inspired helmet liner	EAC	-	Bio-inspired and compliant mechanisms	-	2018	[59]
Innovative helmet liner	EAC	ABS, TPU, PE and PP	arrowhead pattern auxetic structure	-	2022	[60]
Football Helmet liner	EAC	TPU	Miura-Ori metamaterial	Additive manufacturing: FDM	2021	[26]
Helmet liner	EAC	TPU	Origami-inspired	Additive manufacturing: Inkjet	2021	[61]
Custom-fit bicycle helmet	Fit-accuracy	Cellular	Closed cell foam	-	2018	[22]
HEXR bicycle helmet	Fit-accuracy and EAC	Polyamide-11	Honeycomb	Additive manufacturing: SLS	2019	[62]
Custom-fit bicycle helmet	Fit-accuracy	Cellular	Closed cell foam	CNC milling	2018	[63]
KAV bicycle helmet	Fit-accuracy and EAC	Nylon	Honeycomb	Additive manufacturing: FDM	2022	[64]

2.2 Bicycle Helmet Design

2.3 Miura-Ori Metamaterial

The ancient Japanese art 'Origami' has been around for many centuries. The word 'origami' is composed of two separated words: 'ori' and 'kami', which mean folding and paper, respectively. It is a technique to fold papers and changing it from two dimensions into three-dimensional geometries [65]. Origami patterns come in a broad range, yet they always follow the same basic guidelines. A single 2D sheet is the starting point for an origami construction, and the pattern is then tessellated in both directions to produce the required origami structure. The structure can also be tessellated to 3D, where it is then layered in the Z-direction, allowing for the identification of the structure as a metamaterial [5]. Originally solely used for decoration, origami has gained popularity in recent years and has developed into a superb structure for various technical fields, including aerospace, defense, and construction [66].The flexibility of origami-based buildings to be created as a flat structure while yet being able to fit into a curved area is what makes it intriguing [67]. The motion of the origami is often realized by folding the structure along the folding creases and allows endless folded configurations. However, only a few are used for engineering applications: Flasher, Kresling, Yoshimura, Waterbomb and Miura-Ori (MO) [66, 68, 69]. The latter is the most well-studied and widely used pattern in engineering applications and has been manufactured from metals, thermoplastic elastomers and composites. Moreover, the mechanical properties of this pattern have extensively investigated due to their ability to be optimized to preference. Mosleh et al. examined different anisotropic materials and they discovered that anisotropic materials showed promising properties for energy absorption applications [70]. For instance, the MO metamaterial (MOM) has anisotropic behaviour, which means that it presents contrasting mechanical properties in relation to the loading direction [71]. Therefore, the geometry of the MOM can be designed to adjust the mechanical properties to improve the energy absorption capabilities during compression. The geometry of an MO unit cell plays an important role for the mechanical properties. It consists of multiple geometrical parameters that have influence on the final mechanical properties, see Fig. 6. It is worth mentioning that the MOM is stacked with two different sheets of unit cells, sheet A and sheet B. They are tessellated in the X and Y-direction, which results in the sheets A and B, as shown in Fig. 7. For creating the MOM, the sheet must be tessellated in the Z-direction. It is often stacked with the stacking sequence 'ABABA' stacking sequence [5]. The stacking is only possible, for the geometric compatibility of the A and B sheets in the process of folding and unfolding, if both sheets satisfy the following geometrical parameters: $S_A = S_B$, $V_A = V_B$, $L_A = L_B$ and $H_B > H_A$.

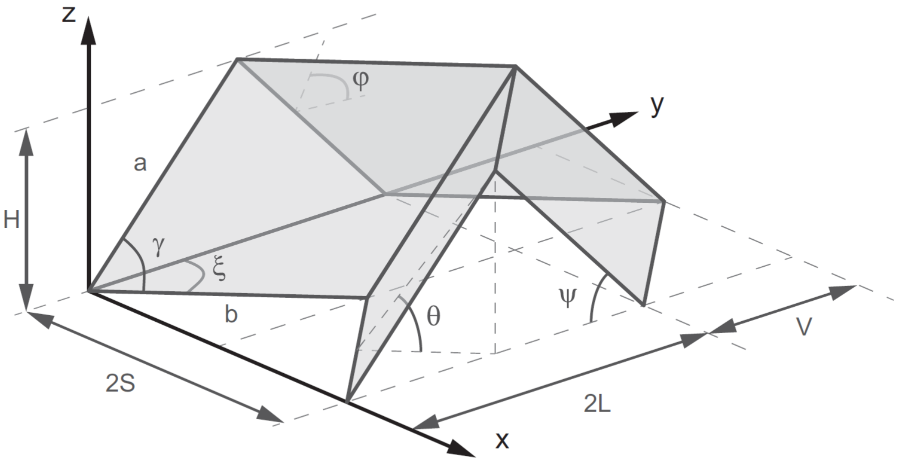

Figure 6: Overview of the geometrical parameters of the Miura-Ori unit cell adopted from [5].

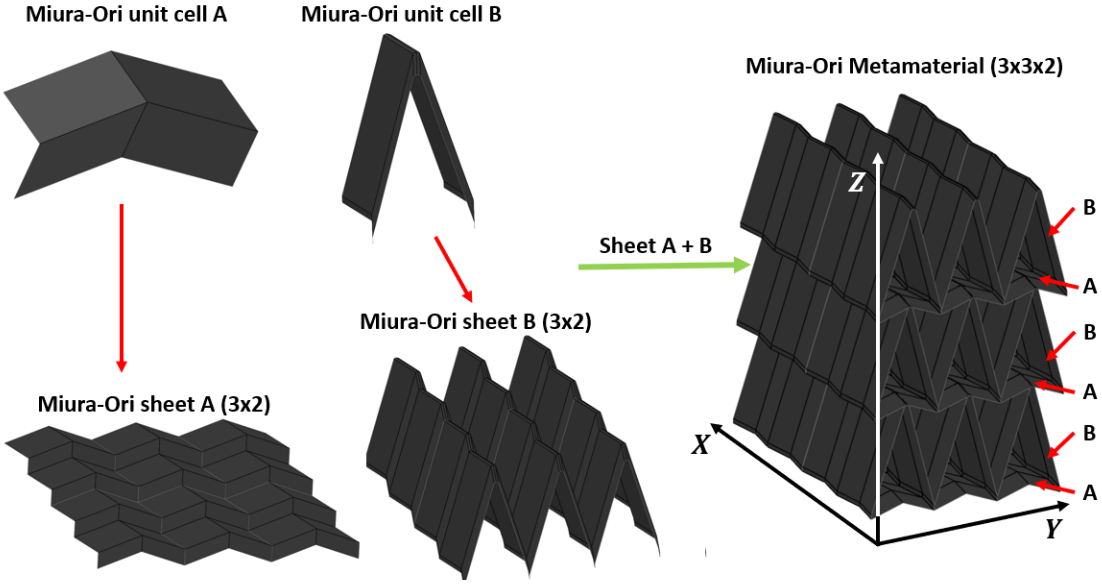

Figure 7: Schematic illustration of the construction of Miura-Ori sheet A and B after which it is stacked according to the stacking sequence: ABABA.

2.3.1 Geometrical Parameters

Figure 6 clearly shows that the MO unit cell consists of multiple geometrical parameters. To summarize, a total of eleven parameters were identified of which three parameters, cell height (H), cell depth (2S) and cell width (2L+V), define the volume. Regarding the other parameters, an overview is given in table 3.

Table 3: Overview of all the geometrical parameters of a Miura-Ori unit cell.

Parameter	**Symbol**
Cell wall length a	a
Cell wall length b	b
Dihedral angle 1	ψ
Dihedral angle 2	ϕ
Folding angle 1	ξ
Folding angle 2	θ
Parallelogram angle	γ
Cell wall thickness	t
Cell wall ratio	a/b

Not all parameters have the same level of importance and therefore parameters that do not have impact on the mechanical properties should not be included for optimization, as they will have a negative influence on the other parameters [5]. In a study done by Hanna et al., it was concluded that three of these parameters have large influence on the geometry, dihedral angle (1) ψ, folding angle (1) ξ and the cell wall thickness t. They investigated the optimal parameters to minimize the peak linear acceleration (PLA) for different football-related impact velocities [26]. 81 different MOM structures were additive manufactured via thermoplastic polyurethane (TPU) and quasi-static and dynamic tested. The results showed that the cell wall thickness (t) was the most influential and the folding angle ξ the least influential. In a different Harris et al. investigation, they examined metallic MOM structures at a set density to see how well they might absorb energy [72]. It is interesting to see that most of the geometrical parameters were fixed at a constant value except for the wall thickness, folding angle, cell depth and cell height. Once more, it was concluded that the wall thickness had great influence on the energy absorption capabilities. Xiang et al. investigated the influence of the angles and the compression behaviors of nylon MOM structures [73]. They created both uniform and graded specimens with different stacking orders. This was achieved by altering the acute angle (α), ranging from 50° to 65°, and the use of a polymer 3D printer. In the end, X. Xiang et al. discovered that the energy absorption was most optimal with an acute angle varying from 50° to 55°. Furthermore, the graded MOM structures showed a considerably higher energy absorption than the uniform specimens. Zhang et al., conducted quasi-static compression tests to investigate the differences between a honeycomb structure and the MOM structure [71]. As mentioned before, there are bicycle helmets that applied the honeycomb structure [74, 75, 76]. It is intriguing to note that one additional significant parameter was found in the Zhang et al. results. The ratio between the lengths of the cell walls a and b is known as the cell wall ratio (a/b). It was concluded that the increase of this ratio had very large impact on the specific energy absorption (SEA). As a result, the MOM structure presented a better energy absorption than the conventional honeycomb structure. They also confirmed this with the quasi-static results that were well-matched with the experimental results. In addition, Lv et al. carried quasi-static tests on the MO patterned sheet [77]. They changed the cell wall thickness (t), the dihedral angle (θ) and the acute angle (α). The results showed that by increasing the cell wall thickness or decreasing the dihedral angle, the energy absorption was better. Furthermore, they discovered that it resulted in a higher stiffness and by altering the acute angle caused a lower peak force.

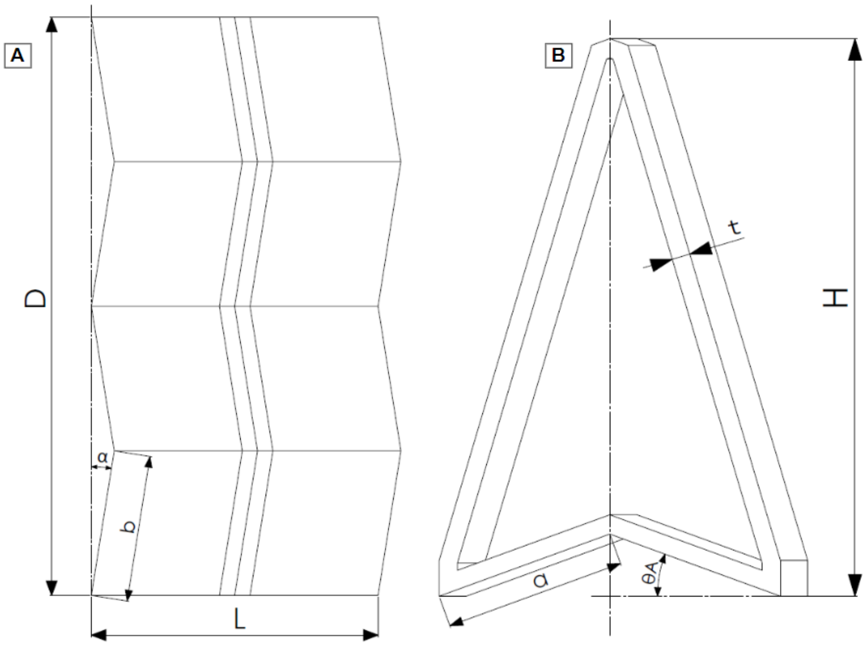

Figure 8: The selected geometrical parameters for investigating the specific energy absorption. The cell wall thickness (t), the dihedral angle (α_A) and the cell wall ratio (a/b).

2.4 Additive Manufacturing: Fused Deposition Modelling

For realizing the bicycle helmet liner, while using a different base material, additive manufacturing has been identified to be a promising candidate. Making 3D models with intricate geometries, like the MOM structure, is referred to as additive manufacturing. In the last couple of years, additive manufacturing has attracted much attention. The most popular is the fused deposition modelling (FDM) technique also known as 3D printing. The key benefits are defined as low-cost, wide variety of material filaments, part optimisation and offering many processing parameters. The FDM allows the control of a wide variety of printing parameters. Within each layer, several parameters can be defined such as the layer height, line width, printing temperature, printing speed and material flow

[31]. These parameters have significant influence on the quality and the mechanical properties of the 3D printed part. As illustrated in Fig. 9, the FDM technique enables the manufacturing of three-dimensional objects. Starting with a direct drive or Bowden system, the material filament is supplied. Both methods employ an extruder to force the filament into the heating element, but a direct drive approach was chosen for this study. The main reason is that it enables a wider choice of material filaments. The filament is pushed through the heating element, which is located before the nozzle. As a result, the filament gets heated and turns into a molten state, which enables the extrusion through the nozzle [31]. Finally, by stacking multiple layers of the molten material on the printing bed, the 3D model is printed. The height of the part is realised by moving the printing bed in the Z-direction, whereas the extruder with the nozzle is moved in X- and Y-directions. For the MOM structures, it is important that the MO sheets A and B are perfectly bonded to each other. It has already been proven to be successful by other studies [26, 30]. The production time is not crucial for this research because the goal is to develop a design model for the MOM cycling helmet liner. Moreover, FDM is a low-cost solution that can help to rapid prototype the helmet liner and allows multiple iterations of the design. During the design of the complex geometry, it is important to think about the use of supports. The FDM allows several types of supports that can be easily removed or dissolved, however, the MOM structures are not ideal for the use of supports. Moreover, it will be impossible to remove any kind of supports within this geometry, and therefore the best approach is to come up with a design that does not require supports.

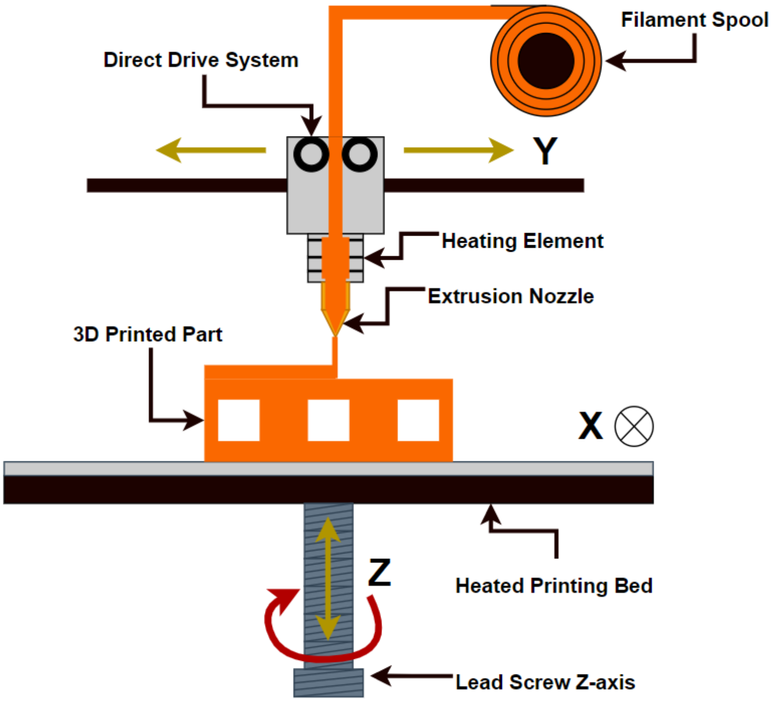

Figure 9: Overview of the fused deposition modelling technique.

2.4.1 Thermoplastic Polyurethane

The recent developments of flexible materials for additive manufacturing provided promising filaments that can be used to manufacture the bicycle helmet liner [78]. As observed in table 2, many studies have already applied such flexible material in their helmet designs. One such flexible material is thermoplastic polyurethane (TPU), one of the many classes that originate from thermoplastic elastomers (TPEs), which are known as a mix of polymers. The unique properties of TPEs, both thermoplastic and elastomeric, present various promising material features. For instance, excellent abrasion resistance and high flexibility but also high impact strength and a low relative density [32]. Furthermore, it is able to undergo multiple high strains during compression and still recover. The short relaxation time of the material enables it to quickly recover to its original state. Two promising candidates are selected; the NinjaTek NinjaFlex filament and the PolyMaker filament. Both are a TPU filament with different shore hardness, 85A and 95A respectively. They presents high flexibility and high elongation, which are both beneficial for energy absorption. In section 4.1, tensile tests will be conducted to select the right filament for additive manufacturing the MOM structures.

2.5 Conclusion: Research Gaps and Limitations

The number of bicycle helmets designs has been increased since the introduction of the first helmet in 1975. Although bicycle helmets have been around for almost 50 years, the process to manufacture the helmets, and the approach to protect the human head have undergone only minor changes. To date, the majority of the helmet liners are still manufactured with EPS foam. However, the foam is limited for energy absorption optimization due to its mechanical properties. Moreover, the sizing of the helmets is outdated and are still designed based on headforms. Due to the inappropriate and inadequate helmet fit experienced by many users, bicycle helmet use is restricted. This causes the users to sacrifice the helmet due to the discomfort, which is problematic. Cyclists that do not wear a helmet are more prone to severe head injuries. To overcome this problem, new emerging (meta)materials and structures were designed and applied to multiple helmets. The literature showed that there is indeed a promising metamaterial that can be used to design a bicycle helmet. The MOM has proven to be a promising candidate for a variety of applications. The MOM gives more scope in terms of optimisation and energy absorption capabilities. It presents numerous geometrical parameters which allows the MOM to be optimally designed. Although many studies showed the significance of the MOM, no one has applied to a bicycle helmet yet. Therefore, the purpose of this project is to create a MOM-based cycling helmet liner design and produce it using additive manufacturing. The MOM is based on the individual MO sheets A and B, which means that the base material can be freely chosen. From the literature review, it was clear that there is a potential base material that has not been applied before in bicycle helmet liners. The AM technique that will be used is FDM and allows the use of TPUs to manufacture parts. Finally, to make sure that the design is custom-fit, 3D scanning equipment will be used. It is believed that this will lead to wider adoption and reduce the number of severe head injuries. The literature review showed that there are still numerous research gaps and limitations in terms of designing a novel custom-fit bicycle helmet. To summarise all the findings, a list is provided below:

- The number of researches for manufacturing a novel custom-fit bicycle helmet with additive manufacturing is scarce.
- Studies prove that origami based metamaterials are promising candidates to be utilised in helmets, i.e. the Miura-Ori metamaterial. However, studies that have used it for bicycle helmets do not exist.
- Different set of geometrical parameters for the MOM structure have been investigated. However, the combination of wall thickness, dihedral angle and cell wall ratio have not been investigated yet.
- Bicycle helmets manufactured with flexible materials such as TPU are sparse. The use of the FDM technique in combination with this material must be investigated.
- According to studies, the barrier of bicycle helmet discomfort is the reason for the low rate of helmet use. For the past 30 years, the design, materials, and production process have not altered.
- The available helmet sizes can not fit the majority of the users. This is because the sizes are based on standard headforms only. Moreover, it confirms that the current procedure for sizing helmets is outdated.
- The 3D scanning technique shows can capture the unique and its dimensions of the human head. Only a few have applied this to bicycle helmet designs.

3 Methodology

This chapter explains the methodological approach that has been used for this research. It consists of unique methods for both computational and experimental work. The approach was based on the objectives that were set in section 1.2. First, to obtain an accurate 3D model of a human head, a novel method based on reverse engineering and a 3D scanner was described. Next, the Miura-Ori Metamaterial (MOM) samples were created by using the Design of Experiments (DoE) method. Moreover, the efficient method called Taguchi was utilised to determine the samples and to study the relationship of multiple input parameters. Subsequently, a novel method was used to create a parametric design of the MOM and application to the bicycle helmet liner. Furthermore, this method helped to validate the parameters that were used for the Taguchi samples. Finally, an approach was developed to ensure accurate manufactured MOM samples and eventually the prototype bicycle helmet liner.

3.1 Develop a Design Framework to Capture the Unique Shape and Dimensions of the Human Head

In chapter 2, it was concluded that the current process of determining bicycle helmet sizes is outdated [23]. The sizing is purely based on the circumference of the human head and does not account for the unique shapes and dimensions of the human head. Hence, a novel method was established to capture all the aspects of a human head: circumference, shape and dimensions. The methodology is adapted from a study done by Wang et al. [79]. They used the concept of reverse engineering (RE) to define the above aspects of the human head with help of a 3D scanner. In general, the process of RE can be described in three steps. The first step is using a 3D scanner, secondly processing and analyzing the data and finally constructing a CAD model. The aim of RE is to improve or re-innovate existing products [80]. It uses the existing product as the starting point, which in this case is the human head.

3.1.1 Method to Capture Unique Head Shape and Dimensions

The 3D scanner used for this research is the Artec Eva^{TM} and is shown in Fig. 10b. It is a handheld scanner that can be freely moved in space and creates highly accurate point clouds. The maximum accuracy is 0.1 mm and the maximum achievable resolution is 0.2 mm. It is able to capture a maximum volume of 61.000 cm^3, which is sufficient to capture a human head. The 3D scanner can capture 5 to 15 frames per second, and all these frames are eventually merged as a polygon mesh. The mesh can be exported in formats such as OBJ, PTX, STL or PLY. For this method to succeed, the hair of the person must be covered. Hence, a silicon swim cap was used to help hiding the hair and simultaneously reveal the true shape of the human head. After the swim cap was positioned, it was sprayed with anti-reflective spray. This is often used for objects that have a high reflective or mirroring surface and is proven to enhance the accuracy of the 3D scan [81]. The operator of the 3D scanner walks around the human to capture multiple frames. Next, the frames were merged in *Autodesk Meshmixer* and resulted in a solid 3D scan, see Fig. 11. All 3D scans were modified with the 'Smooth' function in Meshmixer to remove any inaccuracies or unwanted areas. It is clear to see that the 3D scan with hair (Fig. 11a) makes it difficult to recognize the shape of the human head. At the same time, the 3D scan with swim cap (Fig. 11b) highlights the unique shape of the human head. This is beneficial and allows to determining the surface for the helmet liner. The most promising 3D scan was exported as .STL file and imported into the computer-aided design (CAD) system *Rhinoceros 3D.*

3.1.2 Defining the Helmet Liner Surface on the Human Head

The design framework consists of two parts, where the first past has been described in section 3.1. This resulted in a very accurate 3D scan of the human head, which could be saved as .STL file and imported into Rhino. The second part resulted in the surface for the helmet liner. The human head was split from the body to create a smaller model. Subsequently, the mesh was rebuilt by using the function 'QuadRemesh' to create a quad mesh and significantly decreased the number of polygons. According to Wang et al. [79] it was important to obtain the Non-Uniform Rational B-Splines

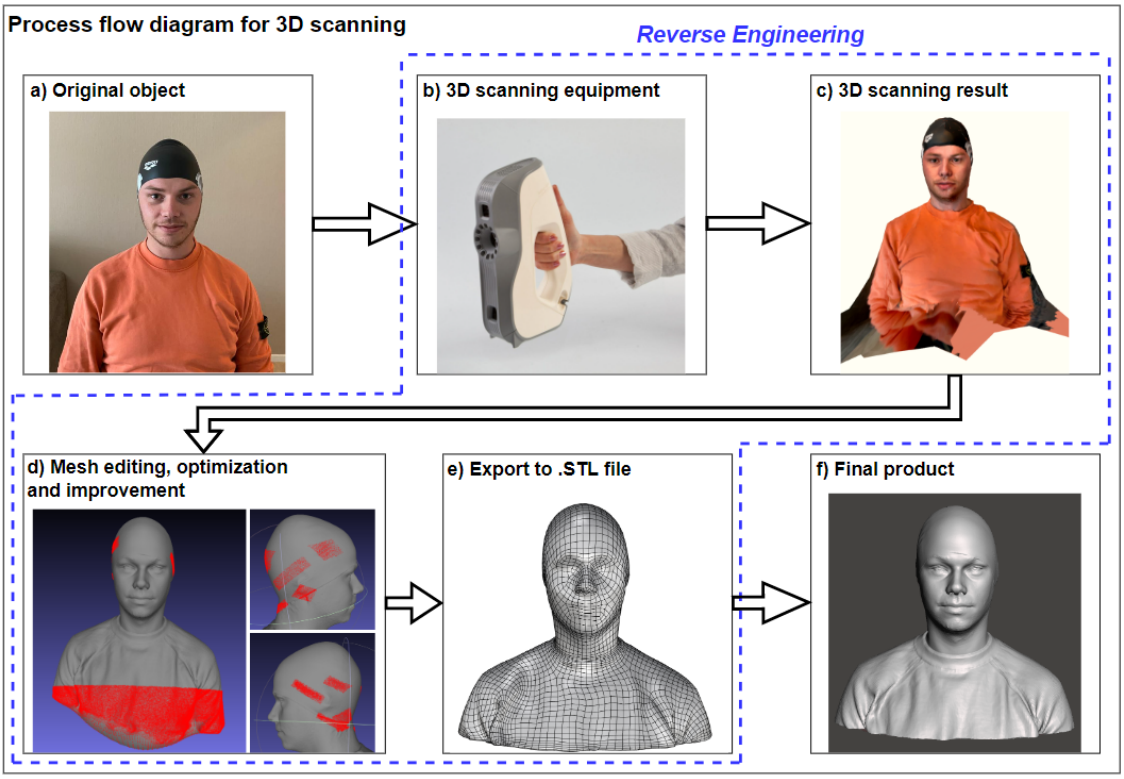

Figure 10: Process flow diagram of 3D scanning by using reverse engineering. a) Original object/part, b) 3D scanning equipment: Artec EVA, c) Scanning of object/part, d) Surface construction with Meshmixer, e) Exporting to .STL file and f) Final product of 3D scanning.

(NURBS). It creates a highly accurate mathematical representation of the 3D geometry and is often used for manufacturing products [82]. However, by using Rhino, it was possible to directly convert the mesh to a SubD model. A SubD model creates the same mathematical representation as a NURBS model, but allows for more control of the geometry. A major advantage of SubD models is the local control of the faces, whereas a NURBS model can only be controlled by its local points. This gave more opportunity and freedom to edit geometry quick and easy while maintaining a high accurate model. Next, the quad mesh was converted to a SubD model with help of the 'ToSubD' function. The complete transition from .STL to SubD model is illustrated in Fig. 12. The SubD model allowed to individually select curves, edges or faces. This helped to select the correct curves that were used to define the boundaries of the helmet liner area. The exact area that is covered by the helmet liner was based on existing bicycle helmet liners and the field of vision derived from the international safety standard EN-1078:2012+A1, see section 4. By defining the correct area via the SubD model, the area was cut from the human head. This created a new SubD model that only contained the helmet liner surface and matched the unique head shape. Moreover, the SubD model defines the base area for the helmet liner. An offset of 8 mm was required to cope with the average thickness of the hair. The model was divided into the lowest number of faces, while maintaining the unique head shape. A high number of faces would complicate the model and significantly increases the computational time. The final result, which is the SubD model as illustrated in Fig. 13, matches the human head shape and includes an offset of 8 mm. Furthermore, it has multiple control points that allow the SubD model to be shaped in more detail. This gives the opportunity to locally change the individual faces of the SubD model and therefore follow the shape of the human head more accurate.

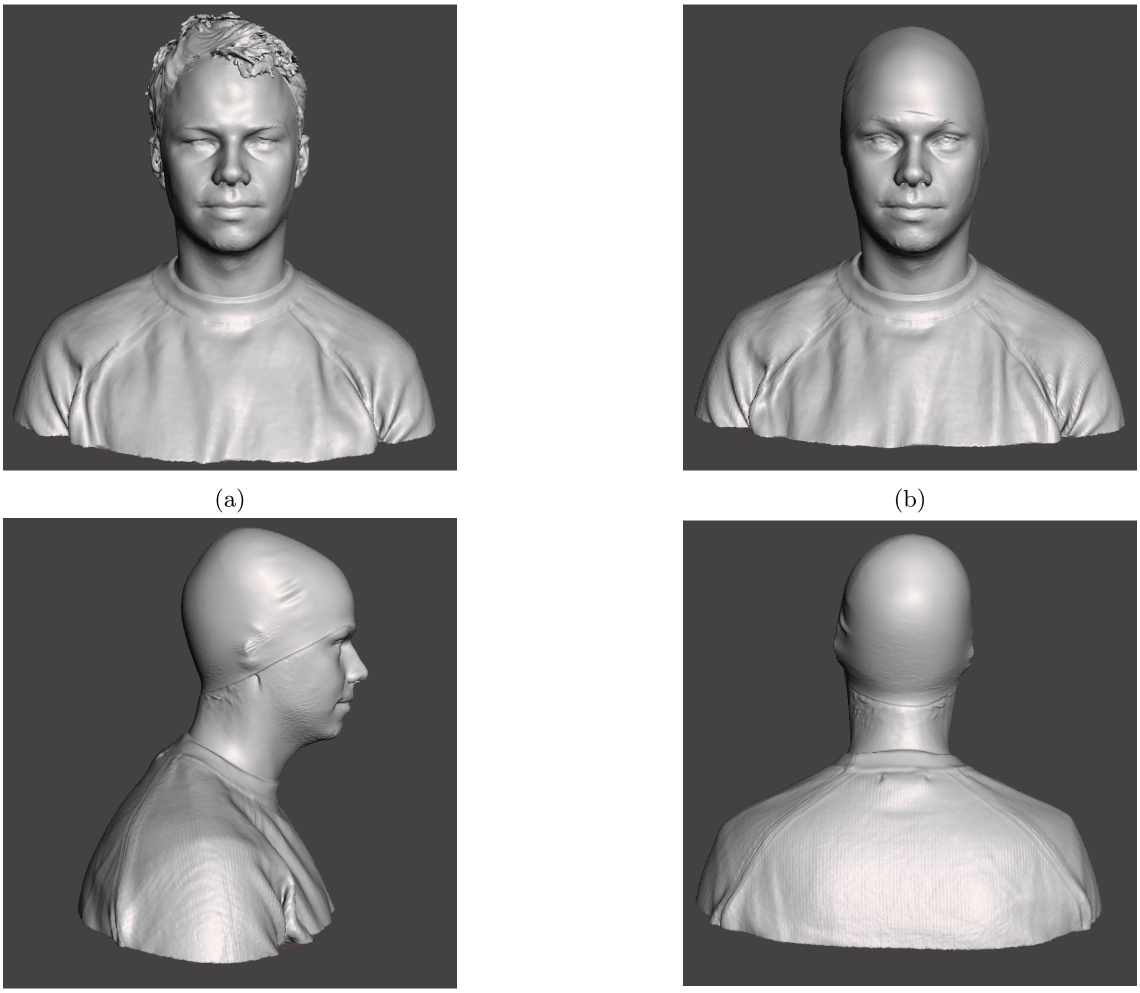
(a) (b)
(c) (d)

Figure 11: Overview of 3D scans produced by the Artec Eva$^{\text{TM}}$: a) human with hair, b) human with silicon swim cap, c) side view and d) back view.

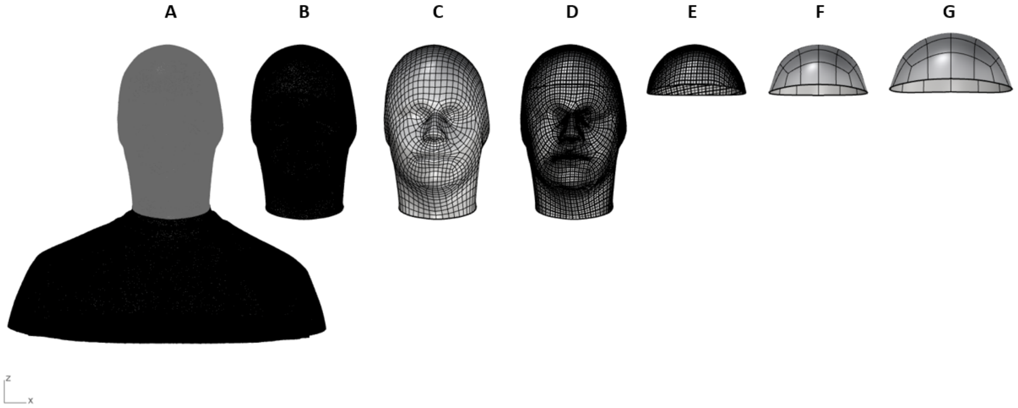

Figure 12: Conversion overview from [A] .STL file, [B] cut-off head, [C] QuadRemeshed head, [D] SubD model of head, [E] helmet liner area, [F] rebuild SubD model and [G] final SubD model with 8 mm offset.

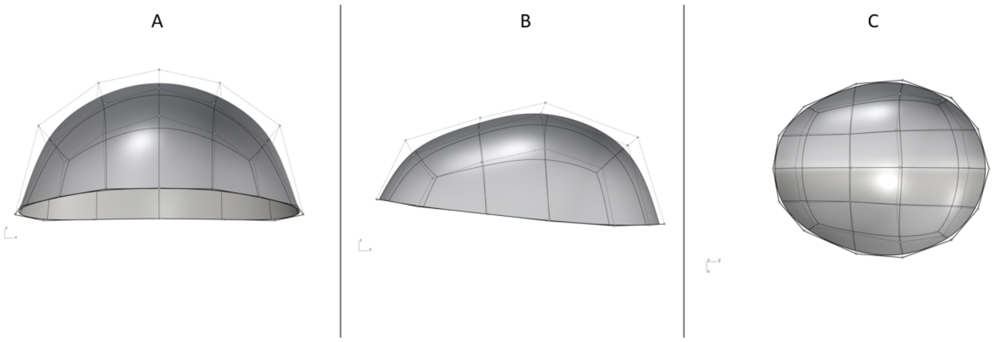

Figure 13: Representation of 8 mm offset SubD model based on the 3D scan of the human head

3.2 Establishing a Strategy to Design and Analyse MOM Structures

This section presents the method to define the MOM structures, which are used for the experimental work. From section 2.3, it is known that there are two types of MO sheets (A and B) that are stacked to create the MOM. These MO sheets are both designed with the same set of geometrical parameters. However, three parameters were chosen to be examined: wall thickness *(t)*, dihedral angle *(θ_A)* and the cell wall ratio *(a/b)*. In general, for investigating the effects of multiple parameters, full factorial Design of Experiments (DOE) is used. This method examines all the possible combinations of the three parameters. The total number of experiments is based on the below, equation (1). The E represents the total number of experiments, the X accounts for the number of levels for each parameter, and k the number of factors per level.

$$E = X^k \tag{1}$$

The number of experiments increases fast if more levels and factors are required. For instance, a full factorial DOE with three levels and factors results in a total of 27 experiments. In addition, to prove the repeatability and reliability, all experiments should be performed three times. That would result in a total of 81 experiments, which makes the investigation infeasible and very time consuming. Hence, the Taguchi's method was selected and is commonly used in multiple studies [26, 83]. It minimises the number of experiments and the time needed to examine the parameters in detail. Furthermore, Taguchi's method helps to understand the relation between the factors and parameters. When compared to the complete factorial with the previously mentioned set of levels and factors. It will yield 27 trials, including repeatability and dependability. This is a reduction of 66% in terms of number of experiments and time needed to fabricate the samples. The samples will be quasi-static compressed to investigate their energy absorption capabilities. The results are analysed by using MINITAB version 20, which includes the calculation of the Signal-to-Noise ratios (S/N) and the ANOVA analysis. An overview of the flowchart that is utilised for Taguchi's L9 is depicted in Fig. 14.

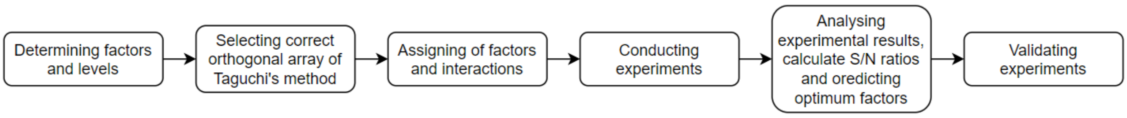

Figure 14: Flowchart for Taguchi's method

3.2.1 Design of Experiments: the Taguchi's Method L9

The MOM geometry cell consists of eleven parameters as described in section 2.3. Three parameters were selected that showed promising influence on the specific energy absorption capabilities of the MOM structure. With help of Taguchi's method, the parameters were examined in more detail, to discover their influence on the energy absorption capabilities. Additionally, three levels per parameter were identified and thus choosing the three-level orthogonal arrays (L9) from Taguchi's method was the most logical option. The reference levels were identified, from multiple studies and were linear divided into a low, mid and high level. Starting with the first factor: wall thickness *(t)*, which is related to the nozzle diameter. The nozzle diameter of the FDM printer was 0.4 mm and to maintain high accuracy and still be manufactured, it is not recommended to print smaller than 0.4 mm. Hence, it was set as the lowest level of the wall thickness factor. On the contrary, the highest level was set to 1 mm. This was examined by looking at the maximum limit of the wall thickness with respect to the characteristic shape of the MO cell. A wall thickness greater than 1.0 mm, will compromise the functionality and performance of the MOM. The mid level was automatically determined as the levels are linear divided, 0.7 mm. The second factor: dihedral angle (θ_A) was also selected to be further examined. There was very little literature about the effects of this angle. One study done by Hanna et al. [26] concluded that when $\theta_A = 20$, the MOM exhibited promising energy absorption capabilities. To better examine this factor and create a wider range of the angle levels, $\theta_A = 20$ was set to be the lowest level. Furthermore, to keep within the limits of the MOM geometry cell and not affecting the functionality, it is recommended to not go lower than 20 degrees, $\theta_A = 20$. Therefore, linear steps of 15 degree were selected and this resulted in a mid level of $\theta_A = 35$ and the highest level $\theta_A = 50$. Lastly, the factor: cell wall ratio *(a/b)*. The foremost reason for examining this parameter is because of a study done by Zhang et al. [71]. They discovered that by increasing the ratio, the specific energy absorption (SEA) would significantly be increased. The ratio is a division of the lengths a and b, which are explained in section 2.3. The mid level was determined by adopting the ratio from Zhang et al. which was 2.0. If the ratio is set to 1.0, it would result in two identical MO sheets, A and B. Therefore, the lowest level was set to 1.5 and thus the highest level to 2.5. The orthogonal array for the Taguchi's method is shown in table 4.

Table 4: Orthogonal array L9 for Taguchi's method.

Symbol	**Geometry parameters**	**Unit**	**Levels** 1	2	3
t	Wall thickness	mm	0.4	0.7	1.0
θ	Dihedral angle	deg	20	35	50
a/b	Cell wall ratio	-	1.5	2	2.5

3.2.2 Analysis of Taguchi L9 Samples

The data of the Taguchi's method was analysed by using the software MINITAB Version 20.0. This technique evaluates the S/N ratio, which measures the performance together with the effects of noise. Moreover, the sensitivity of the examined factors was compared to a criterion. To analyse the final results, a one-way analysis of variance (ANOVA) has been selected. The specific energy absorption (SEA) of the MOM samples was chosen as the criterion against which the results would be assessed in this investigation. It combines the two most important aspects of the MOM optimisation; the mass and the maximum energy absorption capacity. The SEA is calculated by dividing the total energy absorbed per experiment divided by its mass, see equation (2):

$$SEA = \frac{EA_{total}}{mass} \tag{2}$$

In general, Taguchi offers three S/N ratio; minimise, nominal and maximise the response [84]. For this study, a high SEA is preferred and therefore the 'larger-the-better' (S/N_{max}) ratio was used. This ratio is calculated by using the following equation (3):

$$S/N_{max} = -10\log_{10}\left[\frac{\sum_{i=1}^{N}(\frac{1}{y_i^2})}{N}\right] \tag{3}$$

The N the number of the experiment including repetition, y is the response of the variables and i the experiment. Furthermore, by using the one-way ANOVA, the influence in percentage per factor could be obtained. The higher the percentage, the more influence it has on the SEA value. To calculate this value, first the Sum of Square (SS) must be determined for each parameter:

$$SS = -10 \log_{10}\Big[\frac{\sum_{i=1}^{N}(\frac{1}{y_i^2})}{N}\Big] \tag{4}$$

In addition to the SS, the total SS value that represents the whole L9 orthogonal array can be calculated. This is done by using the following equation (5):

$$SS_T = -10 \log_{10}\Big[\frac{\sum_{i=1}^{N}(\frac{1}{y_i^2})}{N}\Big] \tag{5}$$

Both the SS and the total SS value for each examined parameter gives a better insight of what their contribution to the SEA is, expressed in percentages.

3.3 Generation of a Parametric Design Model for MOM Structures

Traditional CAD software have difficulties to generate complex 3D origami structure models. Moreover, parameter analysis often requires a large number of repetitive modeling and adjustments. Hence, *Rhinoceros 3D* (Rhino) and a plugin named *Grasshopper®* (GH) were utilised to rapid model the MOM structures. It is known as a graphical algorithm editor that is strongly connected to Rhino. It can create parametric automated models via a node diagram with multiple variables and parameters. The live result is then visualized in the main window of Rhino. One of the main advantages of using GH is the possibility to quickly change inputs, after which the 2D/3D geometry is automatically updated. Furthermore, it allows to generating predefined patterns on complex surfaces, such as the shape of the human head. In section 2.3, it was described that the MOM consists of MO sheets A and B. These sheets were constructed in GH where after they could be multiplied in the X, Y and Z-direction. To be consisted with other studies, the dimensions were set to 60 x 60 *mm* and the total thickness (D) of the samples was set to 15 *mm*, as this was observed in other bicycle helmet liners [57]. Additionally, the selected parameters for the Taguchi's method were defined and with help of GH; the samples were analysed and validated.

3.3.1 Develop a Parametric Design Model to Create the MOM Structures

The generation of the MO sheets in GH were created by defining a set of five input parameters such as the cell wall ratio a/b, the dihedral angle θ_A, wall thickness t, the length b and the folding angle α, see Fig. 6 in section 2.3. Further, the number of cells could be defined in all three directions, X, Y and Z-direction, see Fig. 54. From section 2.3, it was clear that for the geometric compatibility of the A and B sheets in the process of folding and unfolding, both sheets must satisfy the following: $S_A = S_B$, $V_A = V_B$, $L_A = L_B$ and $H_B > H_A$. An overview of the input parameters to realize the digital modeling process is shown in Fig. 15. By adjusting these parameters, the geometry unit cell of the MOM could be changed to preference. This resulted in a fast method to define all structures, after which they were propagated in all three directions. As a result, a parametric model was created that consisted of four parts: MO sheet A, MO sheet B, generation of MOM, and analysis of dimension and parameters. The complete parametric design model can be found in appendix 7.1.6.

3.3.2 Sheet A

First, sheet A was generated by defining two parallelograms, after which they were mirrored. The parallelogram was defined by the cell wall ratio a/b, the length b and the angle α. It started by using the input parameters as shown in Fig. 15 and with help of several mathematical expressions, multiple points could be defined. This was done by the command 'Pt' after which these points were then used to convert them to surfaces by using the command 'Srf4Pt'. Next, these surfaces were mirrored with help of the command 'Mirror' and this created the sheet A that is illustrated in Fig. 7 in section 2.3. The complete model for the generation of sheet A is shown in appendix 7.1.1.

3.3.3 Sheet B

For the second part, sheet B was created by using the sub-model that is shown in appendix 7.1.2. Prior to the creation of this model, it should be recalled from section 2.3 that for the geometric compatibility of sheets A and B in the process of folding and unfolding, both sheets must satisfy the following: $S_A = S_B$, $V_A = V_B$, $L_A = L_B$ and $H_B > H_A$. Hence, sheet B was based on the output parameters of sheet A and therefore has similar results. Once more, by calculating the correct points and converting these points to surfaces after which it was mirrored, sheet B was created and is illustrated in Fig. 7 in section 2.3.

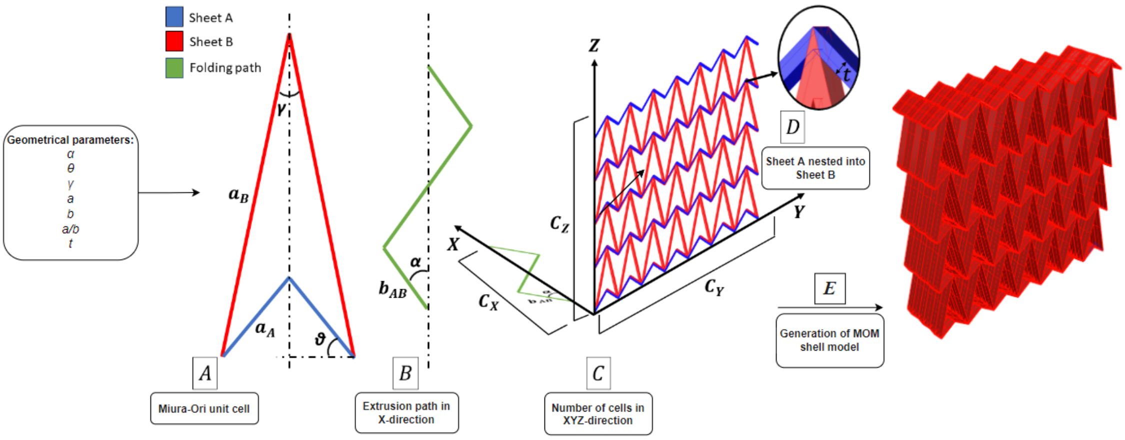

Figure 15: Schematic overview of the digital modeling process to generate the MOM structure.

3.3.4 MOM Generation and Force-Fitting to 60x60x15 mm

After creating sheets A and B of the MO pattern, it was possible to generate the MOM structure, see appendix 7.1.3. Prior to that, the MO unit cell was created, see Fig. 6. By using the command 'BBox' on the unit cell, the geometry was contained inside a box that helped to set the boundaries. This box described the height, length and width of the MOM unit cell. Moreover, after using a second command called 'Box Corners', it was possible to extract the corners of the BBox. From a study done by Harris et al. [85], it was clear that the stacking sequence of sheets (ABABA) should be constructed by nesting the top of sheet B in the bottom of sheet A. This was done to assure that they would share a common apex. Next, this requirement was implemented in GH and allowed the stacking of the unit cells in a correct way. In this way, the BBox that defined the unit cell was decreased in height to complement the requirement and with the next command 'ArrBox', a box array was created. The inputs of this command were the geometry of the unit cell, the redefined BBox and the input parameters 'cells in X, Y and Z'. Regarding the wall thickness of a cell, it was set to propagate inwards while keeping the outer perimeter the same. To investigate the factors and levels of Taguchi's method, all samples must have the same dimensions, 60 x 60 x 15 mm. In GH, a command called 'SrfMorph' allows a geometry to be mapped onto a predefined surface; a 2D rectangle of 60 x 60 mm. Furthermore, a thickness can be defined, which results in a box that matched the desired sample dimensions. The mapping of the MOM geometry was executed by connecting the geometry and its corresponding 'BBox' to the 'SrfMorph'. Furthermore, by using the input parameters from Taguchi's method, GH was able to force-fit all nine samples. The total number of cells per sample *(C_T)* can be calculated by using equation (6):

$$C_T = 2C_Y C_Z - C_Z \tag{6}$$

It is a rather simple multiplication of which C_Y represents the number of cells in Y-direction and C_Z the number of cells in Z-direction. However, it is important to maintain the same number of cells that have been discovered for the erroneous samples as for the forced samples. In this way, the input parameters were satisfied. This approach was used for all nine samples.

3.3.5 Analysis and Validation of the Geometry Parameters

In section 3.3.4, a novel approach was defined to force the structures to fit within the desired sample dimensions. By doing this, the geometrical parameters of the MOM structures were slightly deviated. To assure that these deviations would not affect the performance of the structures, a maximum deviation of 5% was set as the limit. A new GH model was created to analyse the dimensions and the geometrical parameters of the MOM structures, see appendix 7.1.4. The aim was to validate the MOM samples after force-fitting the samples into the desired dimensions. Moreover, to confirm that the errors were not greater than 5%. A simple equation (7) was used and can be expressed as follows:

$$Error = \frac{FFV - IV}{IV} \times 100\% \tag{7}$$

where FFV stands for the force-fitted value and IV for the initial value. In the GH model, it was possible to analyse the factors and levels of Taguchi's L9; the dihedral angle θ_A, the folding angle α and the cell wall ratio a/b. The latter one requires the lengths of side a and b whereas the other two are analysed by checking the angle in degrees. The GH model can be found in the appendices, section 7.1.4. In the model, several commands were used such as the commands; 'BRep', 'DeBRep' and 'ListItem'. The command 'BRep' creates a composition of multiple surfaces from a geometry. Subsequently, the command 'DeBRep' was used to deconstruct it into all its faces, edges and vertices. Not all the segments are needed, and hence the command 'ListItem' was used to individually select the segments that were required.

3.4 Manufacturing of Prototype Bicycle Helmet Liner

The prototype will consist of the MOM structured liner and a simplified outer shell. Both parts are additive manufactured with the FDM technique from TPU and polylactic acid (PLA). Prior to that, a method was developed that enables the layering of the MOM structure onto the earlier defined head surface. This method consisted of a parametric design model and was created in GH. To recall, the helmet liner should be 3D printed without any supports due to the manufacturing time and material costs. Multiple attempts have been made to design the helmet liner with help of flat patterns, which allow the liner to be 3D printed flat. The liner can then be formed into its final shape by placing it into the outer shell. For both the AM processes, a set of printing parameters was investigated to ensure the most optimal settings for manufacturing the prototype.

3.4.1 Novel Method to Layer MOM Structure in Helmet Liner

The SubD model that was defined in section 3.1.2 functions acts as the fundamentals for the helmet liner. In a study done by Luximon et al. [3], a standoff distance (SOD) was presented and could be described as the space between the helmet liner and the human head. They concluded that this space should be between 4 and 8 mm, also considering the average hair thickness that was defined by Ellena et al. [22]. These requirements were implemented into the GH model and was done by applying an offset. The model for the helmet liner consisted of three sub-models such as SOD, unifying the axes and applying the MOM structure to the helmet liner, the complete GH can be found in appendix 7.1.5. Prior to that, the axes from the surfaces of the individual helmet liner must unified, to make sure that the MOM structures are unified. In the GH model, the command 'UnifyUV' was which required two inputs: a guide surface and the surface(s) that should be unified. First, the SubD model of the helmet liner was broken into multiple surfaces by using the command 'Brep'. Next, the guide surface was selected by using the command 'Listitem' on the surfaces of the SubD model. This enabled the individual selection of the surfaces with help of a slider, see Fig. 16. Additionally, the surfaces that should be unified were selected from the Brep into the UnifyUV.

After unifying all the axes of the helmet liner, the SOD could be implemented. A choice was made to apply the maximum SOD of 8 mm and was achieved by applying an offset on the SubD model. As depicted in Fig. 18a, the surfaces of the helmet liner were all unified. The red axis was responsible for the direction of the MOM structure whereas the blue axis denoted the direction of the helmet liner thickness. The final sub-model is the most important one as it was

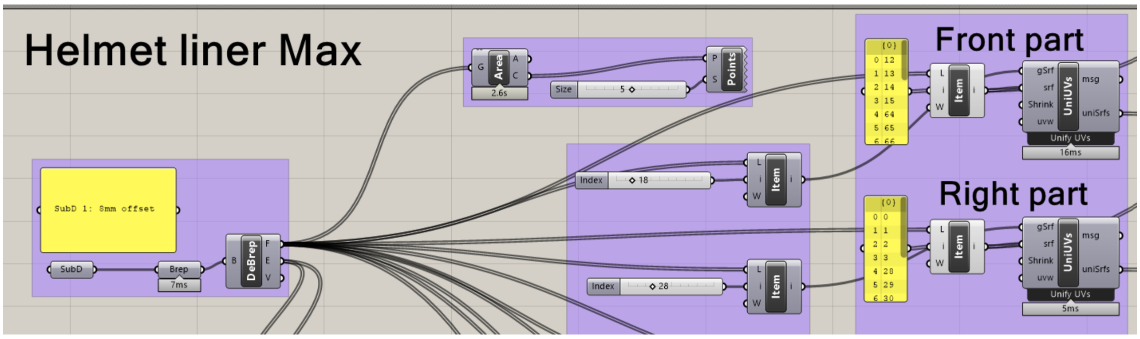

Figure 16: Grasshopper sub-model of unifying all the axes of the helmet liner.

responsible for layering the MOM structure on the helmet liner area. The command 'SrfMorph' can morph a predefined structure on a specific surface. To achieve this, multiple inputs were required: the geometry, the bounding box, the surface and the UVW domains, see Fig. 17. The input geometry will be the finale MOM structure including its bounding box that defines the boundaries. Furthermore, the target surface is the earlier defined surface with the unified axes. Finally, the UVW domains were reparameterised which means that the domains are set from 0 to 1. In other words, the actual lengths of the surfaces are changed to better evaluate the surfaces. As a result, the volume of the helmet liner, that will be filled with the MOM structures can be seen in Fig. 18b. In the end, the most optimal MOM structure will be applied to these volumes, and thus creating the MOM helmet liner.

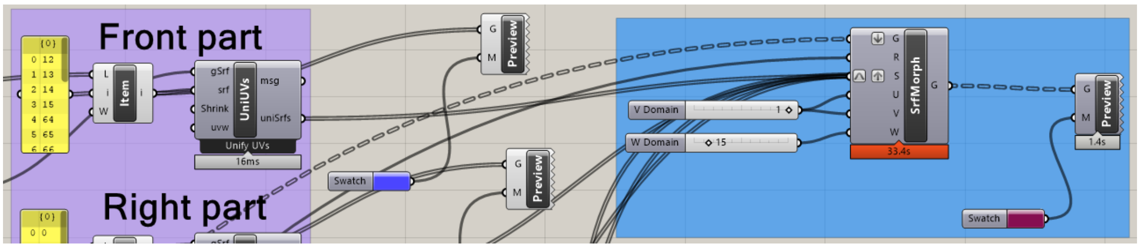

Figure 17: Grasshopper sub-model that morphs the MOM structure onto the helmet liner surface.

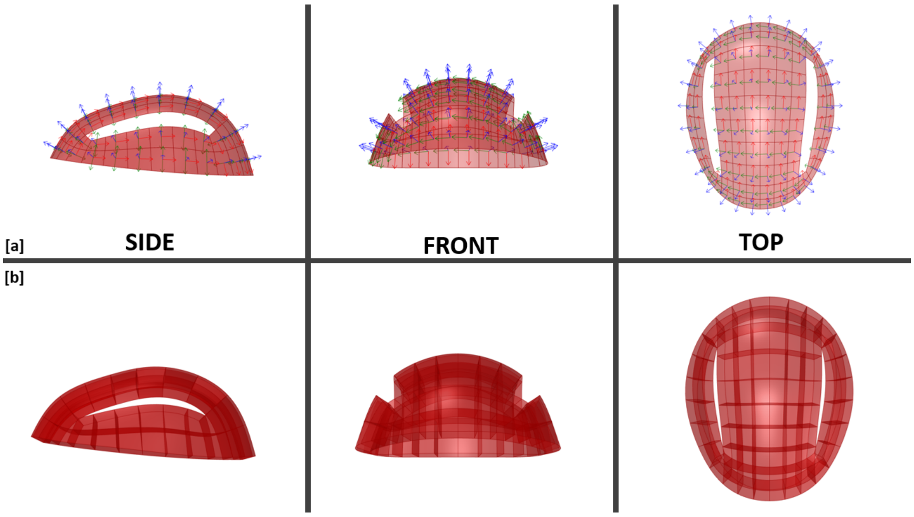

Figure 18: The helmet liner is divided into multiple surfaces after which the axes were unified [a] and the initial result of the surface morph displaying the volume for the MOM structures [b].

3.4.2 Approach to Generate Prototype without 3D Printing Supports

Printing without supports is preferable as it significantly reduces the printing time, filament material and the manufacturing costs. However, it is often difficult to find a solution. For instance, the MOM structure should be curved, to be able to fit within the outer shell and follow the shape of the human head. To achieve this without supports impossible and therefore it is believed that for manufacturing the prototype, it must be divided into multiple parts. Additionally, the parts must be flat patterned after which they can be manufactured without any supports. The helmet liner area, defined in the previous section, was divided into five parts: front, back, top, right and left part, see Fig. 19a. Next, the individual parts where flat patterned by using the command 'Squish' in the GH model. This command enables the flattening of non-developable 3D SubD models and converts them to 2D flat patterns. As depicted in Fig. 19b, the five parts of the helmet liner are now 2D flat patterns. The next step was to investigate what the most suitable approach is to apply the MOM onto the five parts.

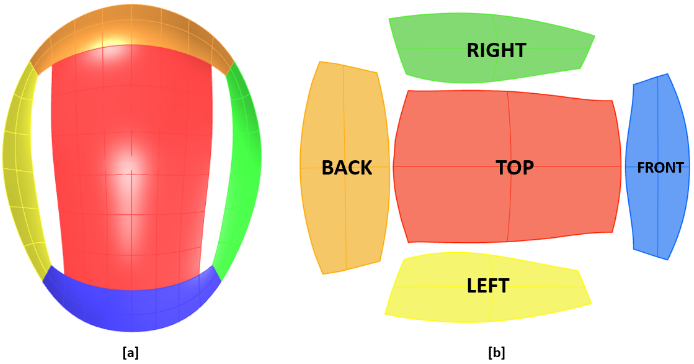

Figure 19: The helmet liner design divided into five parts [a] and the five parts illustrated as flat patterns [b].

Three different approaches were identified and are depicted in Fig. 20. The first approach is the overhang, where the MOM is scaled to completely cover the helmet liner part, see Fig. 20a. It is beneficial as it leaves the MOM structure unharmed and therefore maintaining its function. However, it is larger than the dimensions of the part which makes it very difficult to fit within the predefined area and outer shell. The next approach, graded, deforms the structure to exactly fit within the desired part. The individual unit cells are graded to conform the shape of the part. In Fig. 20b, it can be seen that the structure gradually changes from both sides to the middle. In this way, the part is completely filled with the structure. The third approach is the trimmed one, it uses the same steps as the overhang but cuts the MOM structure at the perimeter of the helmet liner part, see Fig. 20c. As a result, the desired area is filled with the MOM structure but there is a possibility that it will decrease the functionality and performance. The final approach is called: inset and scaled the MOM structure to a level where it fits within the helmet liner part, see Fig. 20d. Although it is able to fit within the predefined area, it discards the optimal geometrical parameters. Furthermore, it is the approach with the lowest fill rate and large gaps are left that are not filled with the MOM structure. For manufacturing the prototype, the graded approach [d] and the trimmed [c] will be used as these method enables the helmet liner part to be completely filled with the MOM and keeping the majority of the MOM unit cells unharmed.

3.4.3 Optimization of Printing Parameters to Fabricate Functional Prototype

The MOM samples and the prototype were 3D printed with the FDM printer: Creatily Ender 5 Pro (Creality 3D Technology; Shenzhen, Guangdong, China). The printer was equipped with a BondTech Direct Drive V3 (BondTech, Värnamo, Sweden) to ease the printing process of TPU85A. A complete overview of the 3D printing setup can be found in appendix 7.2. The samples and the prototype were designed in Rhinoceros 7 (Robert McNeel, USA) after which they were saved as a Standard Triangle Language (STL) file. Next, the STL files were imported into Ultimaker

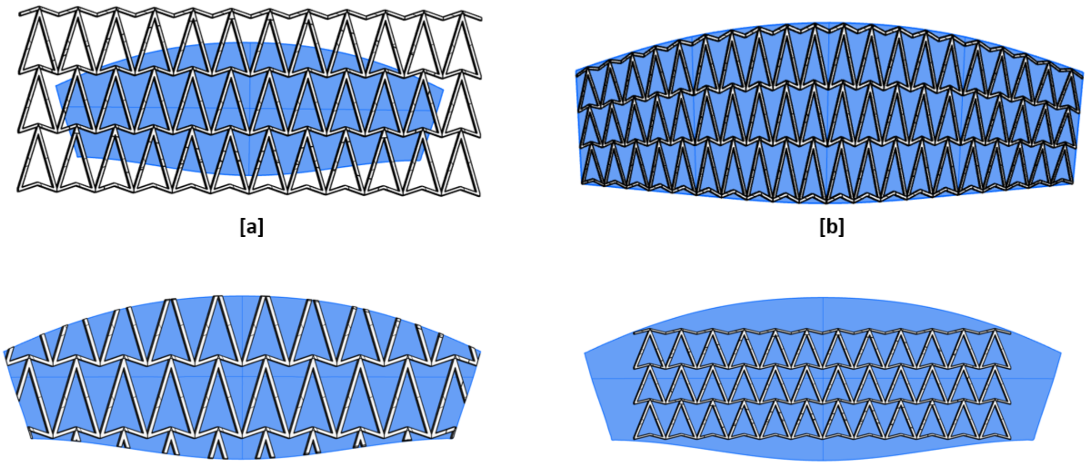
[a] [b] [c] [d]

Figure 20: Overview of possible approaches to additive manufacture the flat patterned MOM structures: Overhang [a], Graded [b], Trimmed [c] and Inset [d].

Cura 5.0.0 (Ultimaker; Utrecht, The Netherlands) and sliced to generate the G-code that must be transferred to the FDM printer. The filament used for 3D printing the MOM structures and the prototype was NinjaTek NinjaFlex TPU85 1.75 *mm* (Fenner Inc., Manheim, USA). In table 5, the recommended printing parameters are shown, which were provided by NinjaTek.

Table 5: The standard printing parameters for Ninjaflex TPU85A provided by NinjaTek.

Parameter	**TPU85A**
Filament	NinjaFlex 1.75 mm
Filament color	Steel Gray
Printing temperature (°C)	225 - 250
Build plate temperature (°C)	$\leq$ 50
Print speed (mm/s)	10 - 20
Infill speed (mm/s)	15 - 35
Cooling	From layer 2

Because TPU is a tough material to print, an analysis was conducted to determine the best set of printing conditions. Although these printing parameters have been provided by the manufacturer, many disagreements were found. The optimisation was done by using Cura, which helped to investigate the individual parameters. Parameters such as the layer height, the line width and the printing plate temperature were not optimised. These were adopted from other studies, the layer height was set to 0.2 *mm* [86]. The line width was set to the diameter of the nozzle, which is 0.4 *mm* and the printing plate temperature was set as provided by NinjaTek, 50°C. The first parameter that was investigated were the extruder E-steps, i.e. the extruder steps per mm, see Fig. 21a. The aim was to improve the accuracy of the movement done by the extruder. This was done by measuring 120 *mm* from the entry of the extruder on the filament, see Fig. 21b. Next, a command was sent to the printer that requires the printer to extrude 100 *mm* with a speed of 50 *mm/min.* Ideally, the remaining length of the filament should be 120 - 100 = 20 *mm*; however, it was clear that the existing E-steps were not optimised for the TPU85A filament. To check the existing E-steps, another software called 'Pronterface' was used. By connecting the FDM printer to the software, it showed the existing E-steps: 710.62 which resulted in 150 *mm*. This was 50 *mm*

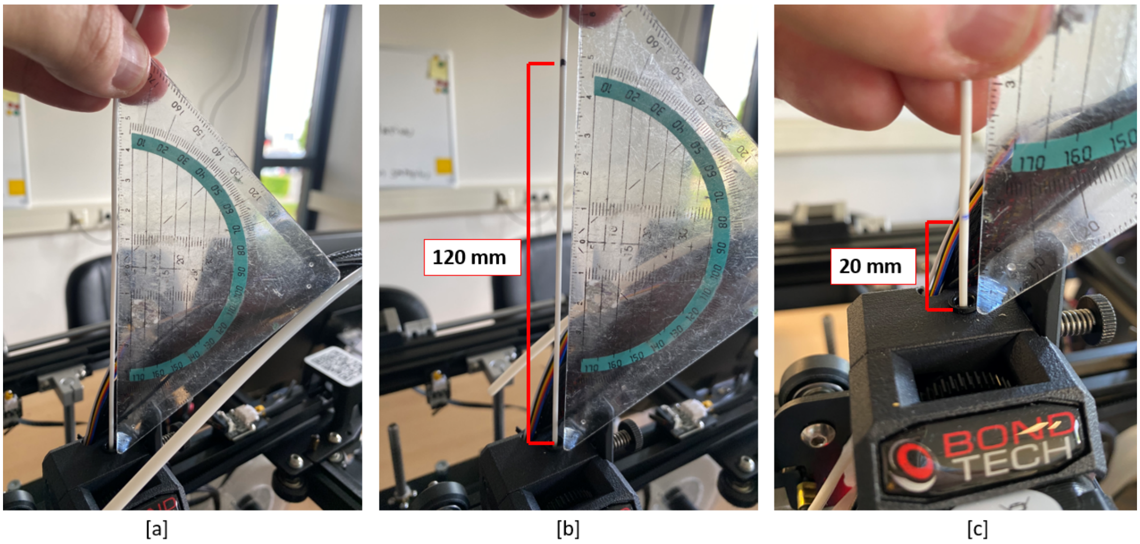

Figure 21: Optimisation of the E-steps setup [a], marking the 120 mm distance on the filament [b] and the remaining length of the filament after extruding a distance of 100 mm [c].

more than the desired 100 *mm*. By using equation (8), the optimised E-steps could be calculated.

$$E_O = \frac{L_R}{L_A} \times E_E \tag{8}$$

where E_O are the optimised E-steps, L_R the requested extrusion length of 100 *mm*, L_A for the actual extrusion length and E_E stands for the existing E-steps. The results showed that the optimised E-steps were 473 and, as depicted in Fig. 21c, exactly 20 *mm* was left. This concluded that the new E-steps were validated and imported to the FDM printer by using Pronterface.

The next parameter that was investigated, was the hot end temperature. The supplier provided a temperature ranging between the 225 and 250 °C. To see which temperature was the most optimal for the TPU85A, a temperature tower was used. This is a 3D part that consists of multiple bridges which can be individually programmed, see Fig. 22a. There are five segments in total (A-E) and each segment was printed with a different temperature. In table 6, it can be seen that the first segment was printed at 225 degrees whereas the last segment was printed at 250 °C, i.e. 5 °C increase per segment. It was observed that the increase of the temperature caused the segments to be more glossy. Furthermore, the bridges were not all printed correctly; segments A, B and E showed much stringing whereas segments C and D had none to little stringing, see Fig. 22b. Moveover, the overhangs differed in accuracy and quality, where segments C and D presented good overhangs. The results showed that a temperature of 235 °C was the most optimal and resulted in the most accurate bridge.

Table 6: The individual temperatures per segment for optimising the hot end temperature.

Segment	**A**	**B**	**C**	**D**	**E**	**F**
Hot End Temperature [°]	225	230	235	240	245	250

The stringing, that was observed at the temperature tower, is strongly connected to the retraction speed of the FDM printer. In general, the filament is melted, after which it is extruded throughout the orifice of the nozzle. A drawback of using TPU based filaments, is that they tend to ooze and drip filament while the extruder is not pushing the filament. The aim of optimising the retraction speed is to remove the stringing, oozing as good as possible. Two different parameters were investigated: the retraction distance (the length in *mm* of which the filament is pulled back out of the nozzle) and speed (the speed in *mm/s* at which the retraction is carried out). Once more, in table 7 the retraction distances per segment are shown. The retraction tower was used

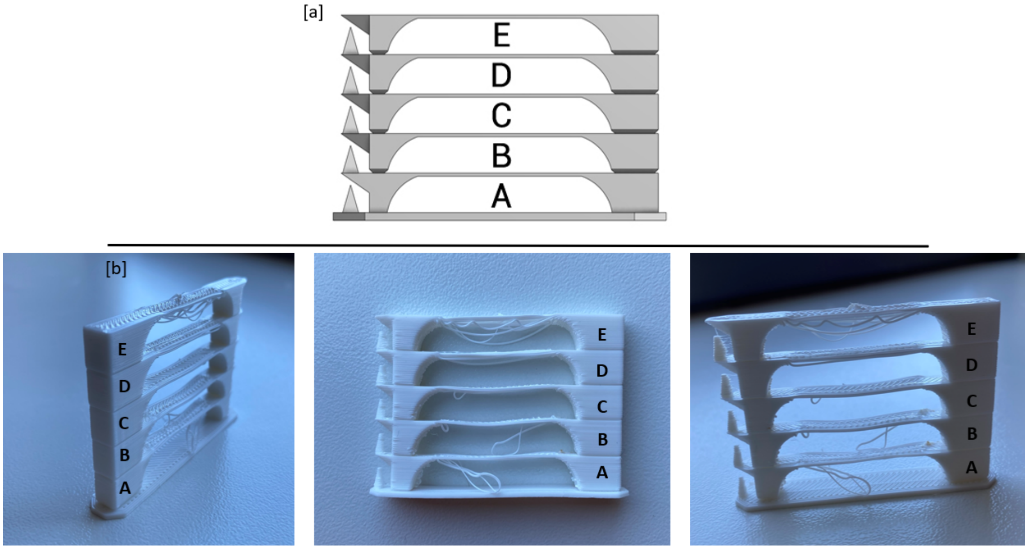

Figure 22: Optimisation of the hot end temperature via the temperature tower [a], the results per segment, with the optimum at 235°C [b].

and consisted of six segments which each had their individual retraction distance and speed, see Fig. 23a. It was observed that a retraction distance ranging from 0.1 to 2.6 *mm* was not optimal and presented excessive stringing, see Fig. 23b1. The stringing decreased from a distance of 2.8 *mm* and was most optimal at a retraction distance of 3.6 *mm* whereas increasing the distance to more than 3.6 *mm* caused the FDM to string again, see Fig. 23b3. Regarding the retraction speed, a speed of 30 *mm/s* was observed to be the optimal.

Table 7: The retraction distances for the individual segments divided into three groups.

Segment	**A**	**B**	**C**	**D**	**E**	**F**
Retraction Distance 1 [mm]	0.1	0.3	0.5	0.7	0.9	1.1
Retraction Distance 2 [mm]	2.0	2.2	2.4	2.6	2.8	3.0
Retraction Distance 3 [mm]	3.0	3.2	3.4	3.6	3.8	4.0

The third processing parameter that was optimized for the TPU85A filament was the printing speed. The printing speed was optimized for printing walls only, as there was no need for infill at the MOM structures. To recall, the wall width is set to 0.4 *mm* which is equal to one wall. Hence, it is important to find the optimal printing speed, to ensure that the quality of the walls is correct. According to NinjaTek, the printing speed should be set to 10 - 20 *mm/s*; however, it is defined for walls. To optimise this parameter, a speed tower was used and is depicted in Fig. 24a. The tower is divided into five segments (A-E) where the printing speed in *mm/s* can be set. The first segment was set at a speed of 20 *mm/s* whereas the final segment was set to 40 *mm/s*, see table 8. It was observed that the first segment presented the good, uniform layers with no stringing. It was clear that by increasing the speed, the wall thickness decreased, and the layers became rippled, including some stringing. The printing speed was in agreement with the existing value that was provided by NinjaTek.

Table 8: The printing speeds for the individual segments of the speed tower.

Segment	**A**	**B**	**C**	**D**	**E**
Printing Speed [mm/s]	20	25	30	35	40

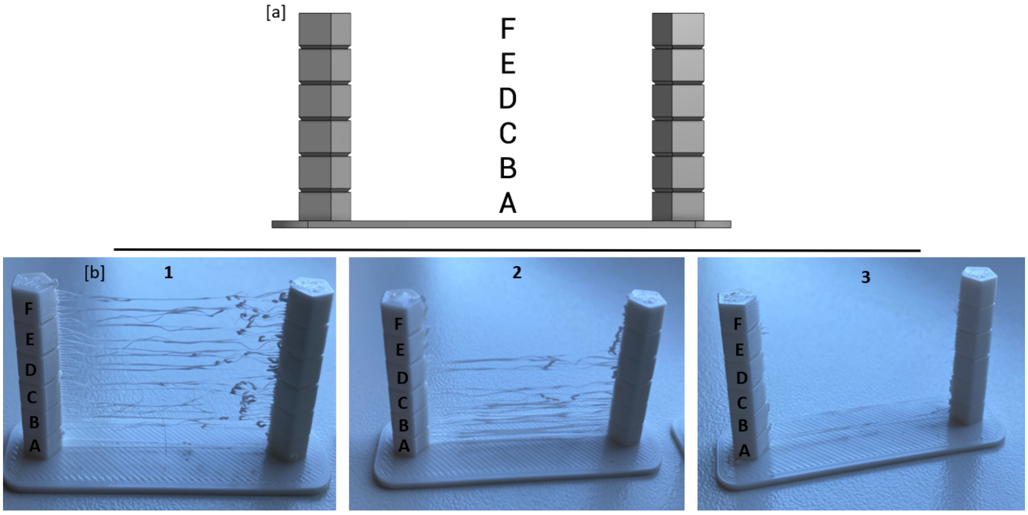

Figure 23: The retraction tower divided into six segments [a], the optimisation of the retraction distance divided into three groups 1,2 and 3 with the optimum at 3.6 mm [b].

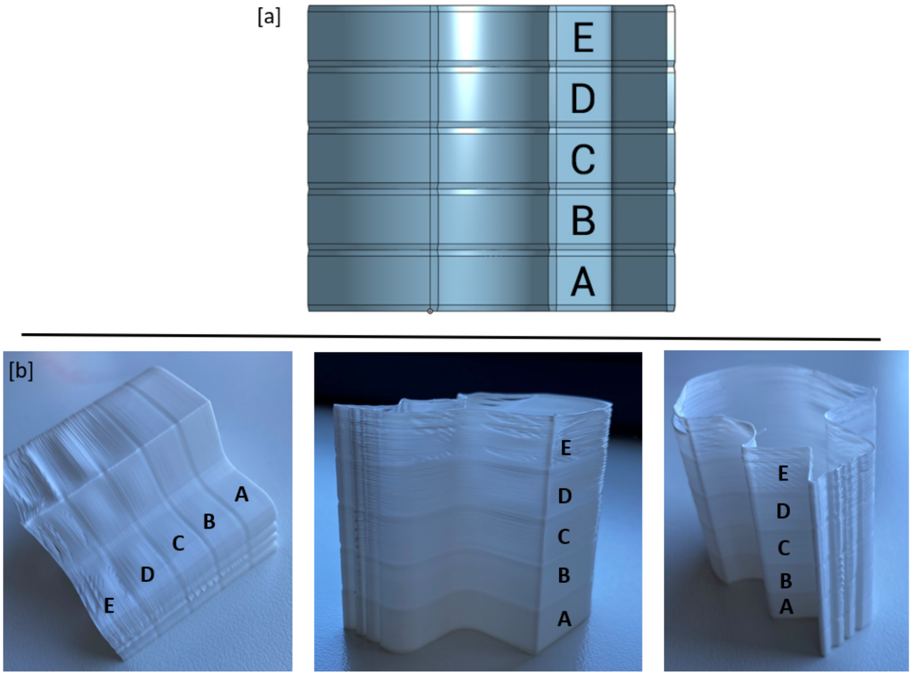

Figure 24: The speed tower divided into five segments [a], the optimisation of the printing speed with the optimum at 20 mm/s [b].

To see if the desired wall thickness was achieved, a thickness gauge was used (Mitutoyo 7300S Dial Thickness Gauge). This device enables precise measurements of the wall thickness from additive manufactured parts. It has a small flat anvil where the part can be placed, after which the trigger is used to enable the gauge. The aim was to see what the most optimal flow rate (%) was for achieving a predefined wall thickness of 0.4 *mm* and as depicted in Fig. 25a, a single wall cube was 3D printed, see Fig. 25b. It was observed that the initial wall thickness was 0.7 *mm*, which is an increase of 0.3 *mm*, see Fig. 25c. The flow rate was too high and was corrected by using equation (9).

$$FR_N = \frac{t_T}{t_M} \times 100\% \tag{9}$$

where FR_N stands for the new flow rate, the t_T for the target wall thickness and t_M denotes the measured wall thickness. The result showed that the new flow rate was 57.14% and was implemented into the Cura slicer. Once more, the single wall cube was printed with a wall thickness of 0.4 *mm* and as seen in Fig. 25d, the measured wall thickness was indeed 0.4 *mm*.

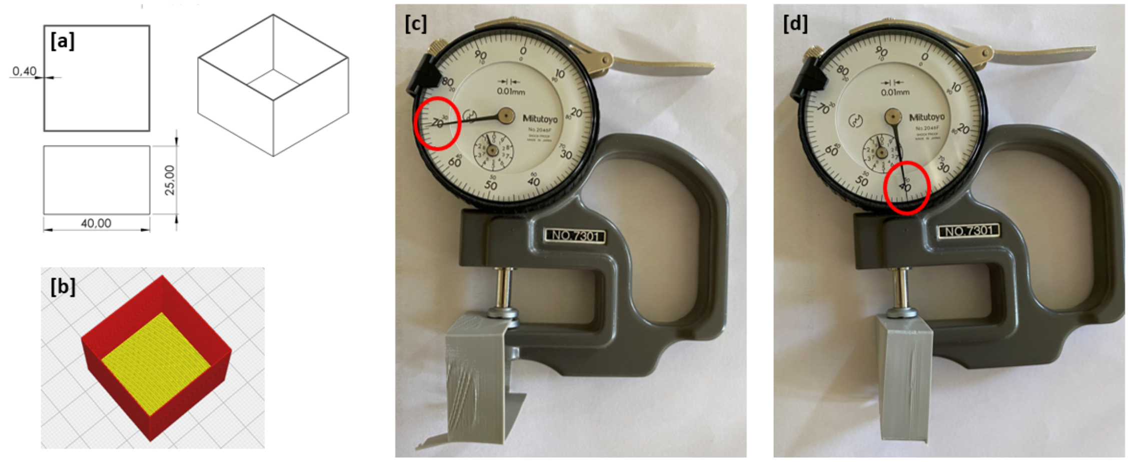

Figure 25: The optimisation of the wall thickness with help of a single wall cube [a], the initial wall thickness with the existing flow rate [b] and the correct wall thickness after optimising the flow rate [c].

The printing parameters that have been optimised during this investigation will be used to print the MOM structures and prototype liner. It was observed that each parameter was different to the printing parameters provided by NinjaTek. In table 9, an overview is listed of the existing and the optimised printing parameters. In the end, the optimised settings were used to print the MOM structures and the prototype liner.

Table 9: Overview of the optimised printing parameters.

Printing parameters	**NinjaTek**	**Existing**	**Optimised**
Extruder Steps [-]	-	710.62	473
Hot End Temperature [°C]	225		235
Layer Height [mm]	-	-	0.2
Line Width [mm]	-	-	0.4
Printing Speed [mm/s]	10 - 20	-	20
Build Plate Temperature [°C]	50	-	50
Retraction Distance [mm]	-	-	3.6
Retraction Speed [mm/s]	-	-	30
Flow Rate [%]	-	100	57.14

4 Experimental Evaluation

4.1 Tensile Test

To investigate the mechanical properties of the filament, tensile tests were conducted. The results can be used for future research to conduct numerical simulations where material models must be created. For this work, two different filaments were investigated: TPU85A and TPU95A. In general, no international standard exist for testing additive manufactured polymers however, the last couple of years more standards proved to be sufficient to test them. One of these standards is the ISO37:2017 which describes a method to determine the tensile properties of thermoplastic rubbers [87]. In the standard, multiple specimen types are defined but to minimize the printing time and material use, type II was selected. The recorded data from the tensile test can be used to create stress-strain curves. These can be used to determine the following properties: elastic modulus (E), ultimate tensile strength (σ_U) and elongation at break (ϵ_B). The printing parameters per filament are denoted in the table 10 below.

Table 10: Overview of the printing parameters per filament

Parameter	**TPU85A**	**TPU95A**
Filament	NinjaFlex 1.75mm	PolyMaker 1.75mm
Filament Color	Snow white	White
Nozzle [mm]	0.4	0.4
Printing Temperature [°C]	235	205
Printing Bed Temperature [°C]	50	50
Layer thickness [mm]	0.2	0.2
Layer width [mm]	0.4	0.4
Infill Density [%]	100	100
Flow Rate [%]	57	85
Retraction Distance [mm]	3.6	3.2
Retraction Speed [mm/s]	30	30
Printing Speed [mm/s]	20	35

4.2 Methodology

The aim of the tensile test is to study the mechanical properties of both TPU85A and TPU95A samples. The specimens were designed according to type II of the ISO37-2017 standard as depicted in Fig. 26a. It can be seen that the total length of the specimens was 75 *mm* and the thickness was 2 *mm*. The TPU85 specimens were produced with the NinjaTek Ninjaflex TPU85A 1.75 mm filament whereas the TPU95A specimens with the Polymaker TPU95A filament. All specimens were 3D printed in the XY-plane with the FDM printer: Creatily Ender 5 Pro (Creality 3D Technology; Shenzhen, Guangdong, China). The specimens were designed with help of SOLIDWORKS 2020 (Dassault Systemes, USA) after which it was saved as a stereolithography (STL) file. Next, the STL file was imported into Ultimaker Cura 5.0.0 (Ultimaker; Utrecht, The Netherlands) and sliced to generate the G-code that was transferred to the FDM printer. The tensile tests were configured by using a ZwickRoell Z5.0kN (Zwick/Roell, Germany) uniaxial testing machine. This machine has a 5 kN load cell with two hydraulic clamps, of which the lower one was fixed, and the upper one could translate in Z-direction. The pressure of both the clamps was set to 4.0 bar and the specimens were tested at a constant speed of 5 mm/min. Fig. 26b shows that the specimens were centered between the two clamps and aligned with the load cell. Each specimen was reproduced three times. This was done to ensure the reliability and repeatability of the experimental tests, but also of the printing accuracy.

The investigated properties were obtained by using MATLAB version 2022a (The MathWorks, Inc., Natick, Massachusetts, United States). The results are show in table 11 and it can be seen that the TPU85A filament complies with the properties given by the manufacturer. The calculated Young's modulus of TPU85A was 13.98 *MPa* which is an increase of 16.5% compared

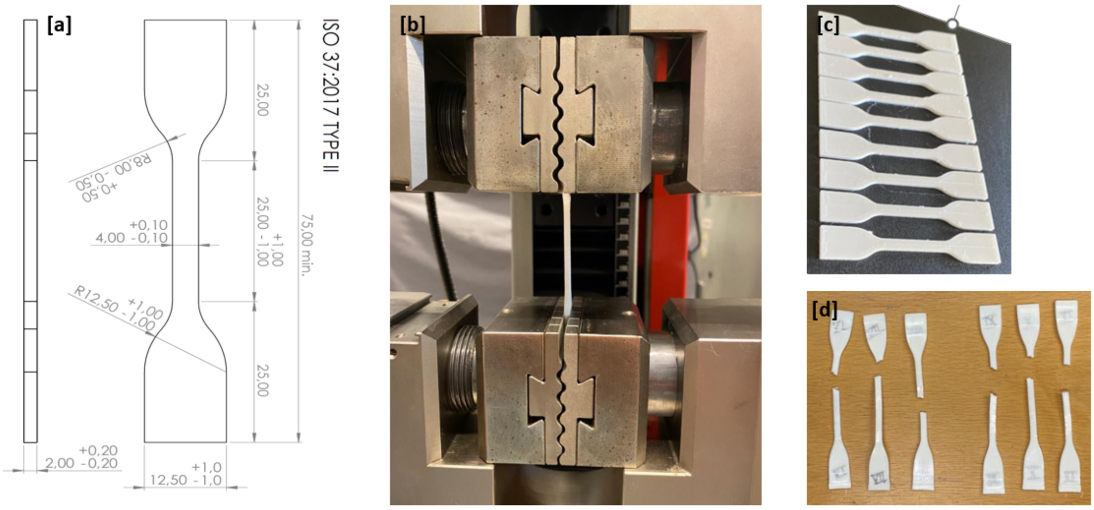

Figure 26: ISO37-2017 specimen type II [a], experimental setup with hydraulic clamps, clamped at 4.0 bar [b]. The additive manufactured specimens [c] and the TPU95A (left) and TPU85A (right) specimens after the tensile tests.

Table 11: Material properties per filament obtained by the tensile tests and compared to the manufacturer.

Property	**TPU85A exp.**	**TPU85A man.**	**TPU95A exp.**	**TPU95A man.**
Young's Modulus [MPa]	13.98	12	25.3	9.4
Ult. Tensile Strength [MPa]	30.69	26	21.66	29
Elongation [%]	681.51	660	404.54	330

to the manufacturer. Furthermore, the Ultimate tensile strength was higher, 30.69 MPa compared to 26 MPa. Finally, the elongation at break of the TPU85A specimen was recorded at 681.51% which was an increase of 3.2%. The breaks occurred in the predefined area and can be seen in Fig. 26d. The recorded mechanical properties of TPU85A were in good agreement with the manufacturer. For the TPU95A specimen, a Young's modulus of almost 25.3 MPa was recorded which is an increase of 169%. Controversially, the Ultimate tensile strength was 21.66 MPa which is 25% lower than the manufacturer. For the elongation, it was almost 405% and thus an increase of 22.6%. The TPU95A specimen did not present agreements with the properties of the manufacturer. This could be due to faulty rupture locations as seen in Fig. 26d another reason could be that the manufacturer used a different standard to define the mechanical properties. The elongation of both specimens differed greatly, for the helmet liner it is desirable to have a high elongation. Therefore, the TPU85A filament with an elongation of 681.51% was chosen to be used for manufacturing the MOM structures and prototype.

4.3 Approach to Investigate Energy Absorption Capabilities of the MOM samples

This section describes a method for collecting data from MOM samples. Moreover, to get a better understanding of energy absorption capabilities and identifying the densification strain (ϵ_d). Quasi-static out-of-plane compression tests were configured by using a ZwickRoell Z5.0kN (Zwick/Roell, Germany) uniaxial testing machine. This machine has a 5 kN load cell with two rigid parallel plates, of which the lower one was fixed, and the upper one could translate in Z-direction. Fig. 28 shows that the samples were centered between the two plates and aligned with the load cell. Regarding the contact between the samples and the plates, no further actions were taken to change the frictional contact. The samples and boundary conditions were simplified and were different

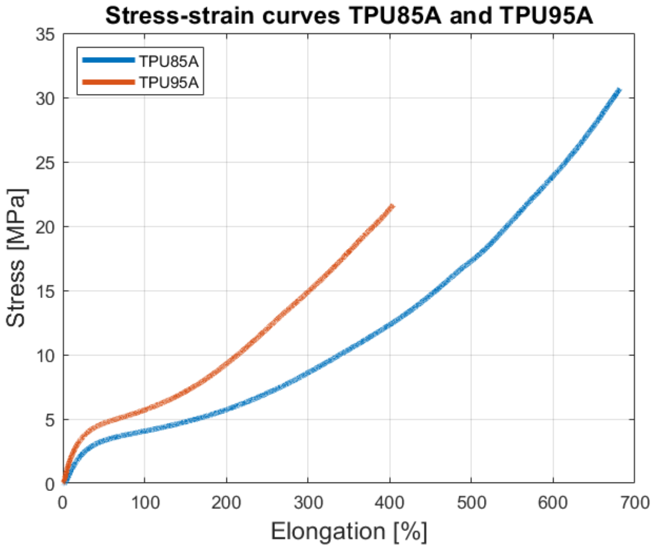

Figure 27: Stress-elongation curves of the TPU85A and TPU95A specimens after tensile testing.

from the final design of the helmet liner in terms of curvature and size. This was done to guarantee that unknown causes do not impact material performance and geometrical parameters. A preload of 5 N was established before the samples were loaded. The loading and unloading rate was adjusted to 25 mm/min to provide excellent contact between the sample and the two parallel compressive plates.

4.3.1 Identifying the Compressive Strain for Testing

Before compressing the samples, it was necessary to identify the compressive strain (ϵ_c). This was done to assure that all samples that will be tested can be compressed up and till their densification. It is the strain describes the maximum strain that will be applied during testing. To define the strain, sample I was cyclic loaded with multiple displacements including 12, 11.5, 11, 10, 9, 8 and 7.5 mm, which corresponds to 80, 76.7, 73.33, 66.7, 60, 53.3 and 50% compressive strain, respectively. A relaxation time of two minutes was implemented between every compression loading. This method was developed by Li et al. [88] and they described how to calculate the onset densification strain (ϵ_d), which marks the start of the densification region.

4.3.2 Calculation of Onset Densification Strain

The recorded data from the cyclic compression tests (the force-displacement curves) of sample I were plotted by using MATLAB version 2022a (The MathWorks, Inc., Natick, Massachusetts, United States). These curves included the loading and unloading of the sample and can be seen in Fig. 29. For this study, only the loading curve was interesting, and therefore these were converted to stress-strain curves. This was done by using equation (11 and 12) to calculate the stress and the strain per loading. Next, it was plotted by using MATLAB as shown in Fig. 30 and by curve fitting those curves, it was possible to integrate them. The integration limits were set from zero up and till the maximum compression strain, to calculate the complete area under the curves, i.e. the complete energy absorption. From here, the EA efficiency was calculated by using equation 15 and was plotted against the maximum stress with the corresponding strain, see Fig. 31a. As described by Li et al. [88], the peaks of the efficiency curves, shown in 31b, indicated the maximum efficiency and the corresponding onset densification strain. The range of the efficiencies was between η= 39.6 - 42.2 % whereas the onset densification strains ranged between ϵ_d= 0.4549 - 0.4722. Finally, these results allowed to define the compression strain for all the tests. This was done by calculating the average onset densification strain of sample I: $(\epsilon_d) = 46.2\%$ which equals to 6.93 mm and is denoted by the black dashed line. This suggested that the compression strain should be set to at least 46.2%. To be sure that the loading curves of all samples are recorded, the compression strain

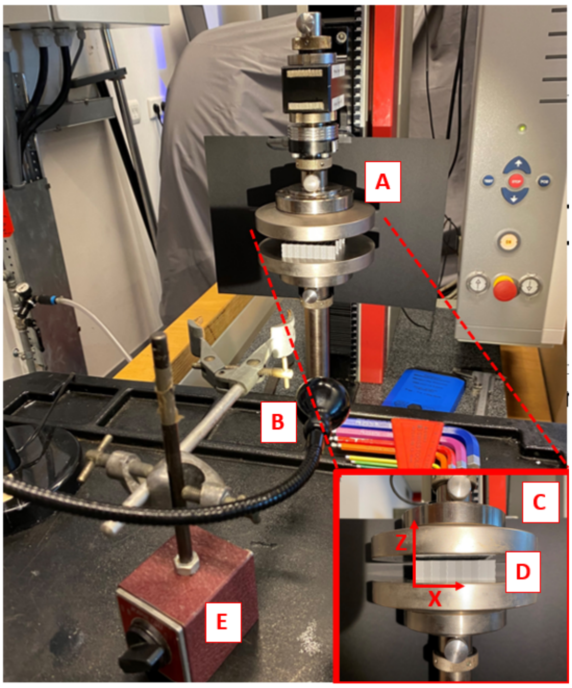

Figure 28: Test setup for quasi-static compression tests: [A] Loading cell, [B] Light source, [C] Compression plates, [D] MOM sample and [E] video setup.

was set to $\epsilon_c = 53.3\%$, which equals to 8 mm displacement. This strain is in agreement with similar studies done with origami structures and base material TPU85A [26, 30]. As described before, the beginning of the densification region is marked by the onset densification strain. Moreover, this value is the limit of the energy absorption capabilities of the MOM structures. Although the MOM structure continues to absorb energy after the ϵ_d, it is not desired as there will be a high amount of stress throughout the structure. The final results of cycling loading of sample I are highlighted in Fig. 32. It can be seen that for the first two cycles, the structure shows softening behaviour, which is common for TPU material [89]. Furthermore, it can be seen that a stabilisation is reached from the third cycle and hence results were recorded from the fourth cycle. This behaviour was also discovered by other researchers and confirmed that the MOM structure was able to recover while providing energy absorption capabilities [90].

4.3.3 Procedure for Quasi-Static out-of-plane Compression Test of all Samples

The samples were compressed out-of-plane (i.e. in the X-direction as shown in 2.3) and as defined in section 3.2.1, each sample was reproduced three times. This was done to ensure the reliability and repeatability of the experimental tests, but also of the printing accuracy. The displacement, i.e. the compression strain was set to 8 mm, $\epsilon_c = 53.33\%$. An overview of all testing conditions is shown in table 12 and all tests were conducted in ambient laboratory conditions. For analysing the mechanical behaviour of the samples, a setup was created to capture photos and videos, see Fig. 28. The load cell measured the force, whereas the displacement was registered by the internal measurement system of the testing machine.

Table 12: Settings for all quasi-static compression tests.

QS Compression Test	**Preload**	**Displacement Rate**	**Total Displacement**	ϵ_c
Zwick Z5.0	5 N	25 mm/min	8 mm	53.33 %

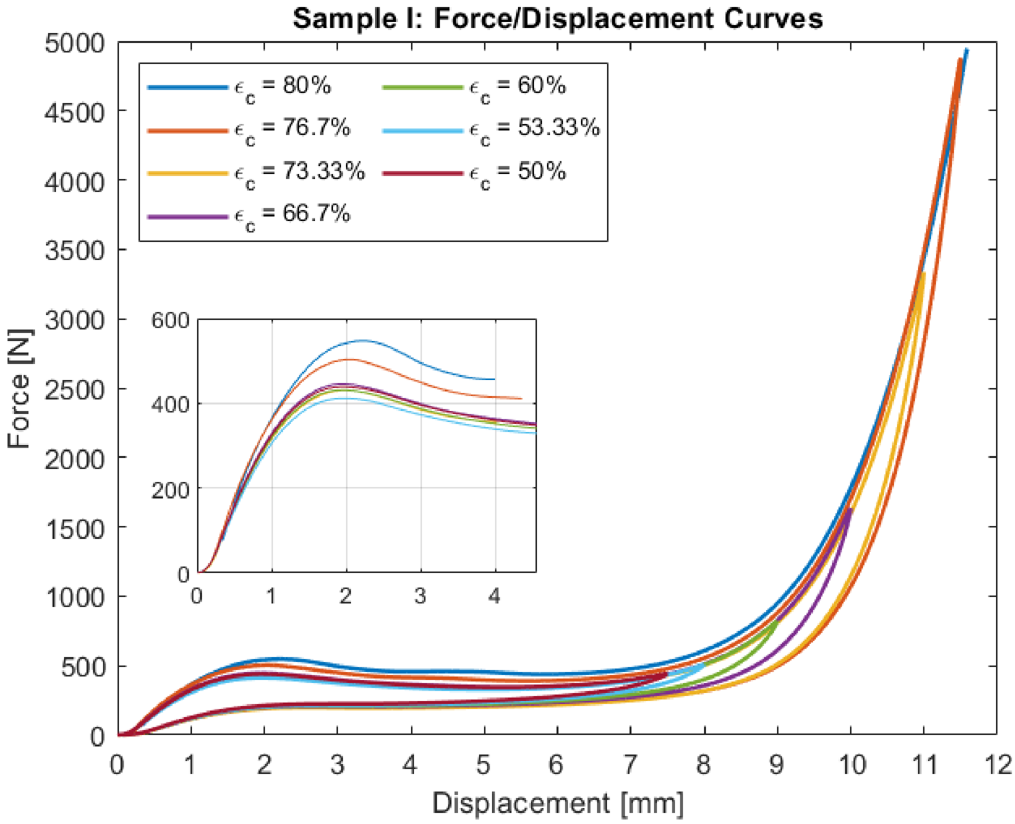

Figure 29: Plot of all force-displacement curves of cyclic loading sample 1 with different compression strains to determine the compression strain.

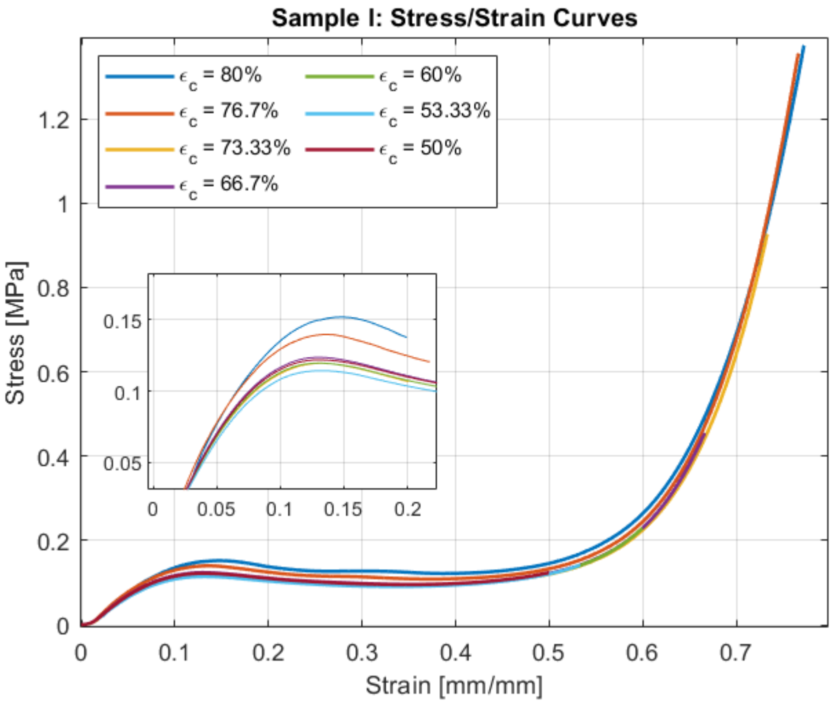

Figure 30: Plot of all stress-strain curves of cyclic loading sample 1 with different compression strains to determine the compression strain.

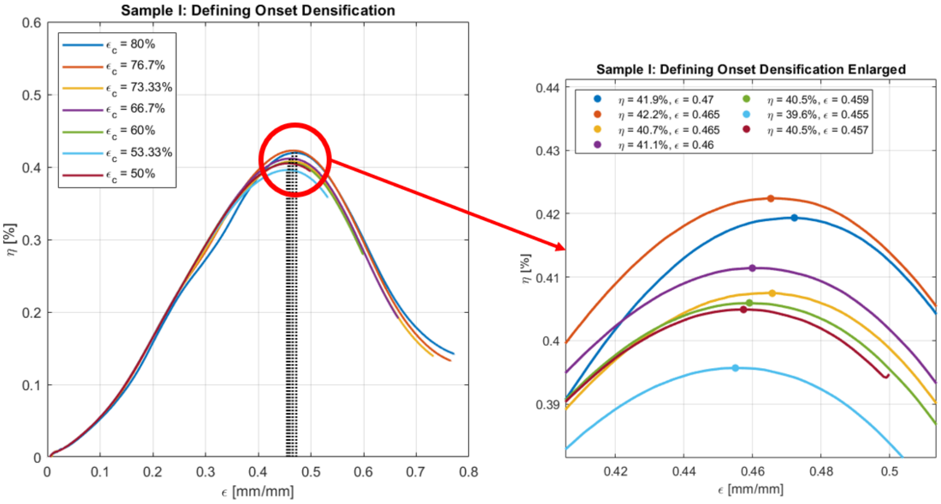

[a] **[b]**

Figure 31: Plot of all EA efficiency-strain curves of cyclic loading sample 1 with different compression strains to determine the onset densification strain [a]. Enlarged plot of maximum EA efficiencies with their corresponding strain of sample 1 with different compression strains [b].

4.3.4 Analyzing of Performance and Data

To select one of the MOM samples, multiple properties such as stiffness, strength, yield stress, stress plateau, onset densification strain, mass and the specific energy absorption must be analyzed. The behaviour of the MOM samples was analyzed during the quasi-static compression and the results will be utilized to create multiple curves such as the stress-strain, energy absorption (EA)-strain and the EA efficiency-strain curves. Before these curves can be analyzed, it is important to know the different regions. In general, three regions can be identified in a force-strain curve, see Fig. 32: the elastic region with the linear slope (I), the plastic region with the plateau (II) and the densification region (III) [30, 88]. In the elastic region, the samples were compressed while the force increases linearly along with the compression strain. At one point, the walls of the MOM structure collapsed due to buckling. From here, a non-linear transition, which includes a peak force, can be seen and marks the end of the elastic region (black dashed line at 2 mm). Inside the plastic region, the strain is increased while the force drops until at one moment it is stabilized and is known as the plateau force inside the elastic region. Finally, the strain reaches a point (the onset densification strain) where the samples are compressed, and the structure undergoes self-contact i.e. the walls are contacting each other. As a result, the force is increased rapidly until the maximum load of 5000 N is reached. As described before, the beginning of the densification region is marked by the onset densification strain (ϵ_d= 46.2%). Moreover, this value is the limit of the energy absorption capabilities of the MOM structures. Although the MOM structure continues to absorb energy after the ϵ_d, it is not desired as there will be a high amount of stress throughout the structure. To compare the MOM structures with other studies, the relative density must be calculated [91]. It is calculated by dividing the density of the MOM (ρ_m structure by the density of the base material (ρ_b). The first one can be calculated by dividing the mass of the MOM structure by the total volume: 60 x 60 x 15 = 0.000054 m^3. In other words, the density per MOM structure differs and thus the relative density as well, see equation (10). Furthermore, the relative density is an important parameter that allows the MOM structures to be compared to other cellular materials with the same relative density.

$$\rho* = \frac{\frac{m_m}{v_m}}{\rho_b} = \frac{\rho_m}{\rho_b} \tag{10}$$

where the m_m is the mass per MOM sample, the v_m the volume of the MOM samples. For composing the stress-strain curves, it was decided to calculate the engineering strain and the stress. This is done because only the original size of the samples is known, i.e. the area of the samples which is equal to 60 x 60 mm = 3600 mm^2. So, the engineering stress is calculated by the following equation (11):

$$\sigma_{eng} = \frac{F}{A_0} \tag{11}$$

where the F is the force measured by the load cell and A_0 the original area of the sample. For calculating the engineering strain, equation (12) was used:

$$\epsilon_{eng} = \frac{\Delta L}{L_0} \tag{12}$$

the ΔL denoted the displacement measured by the internal measurement system and L_0 the height of the sample. After composing the curves, several performance parameters can be calculated: the average stress plateau (σ_{pl}), the energy absorption (EA), specific energy absorption (SEA), the absorption efficiency (η_{EA}). The EA can be described as the maximum work done by the MOM structure up to the limit, i.e. the onset densification strain [74]:

$$EA \;=\; \int_0^{\epsilon_d} \sigma_{eng} d\epsilon_{eng} \tag{13}$$

where the ϵ_d is the onset densification strain and with the EA, the average plateau stress can be calculated according to [92]:

$$\sigma_{pl} \;=\; \frac{1}{\epsilon_d} \int_0^{\epsilon_d} \sigma_{eng} d\epsilon_{eng} \tag{14}$$

The absorption efficiency can be calculated by dividing the complete area up to the compression strain by the maximum stress at the given strain. It can be denoted by the following equation (15):

$$\eta = \frac{1}{\sigma(\epsilon)_{max}} \int_0^{\epsilon} \sigma_{eng} d\epsilon_{eng} \tag{15}$$

Finally, before all tests were conducted, the wall thickness was measured at random locations of the samples. This was done by using a digital caliper. A maximum deviation error of 5% was set to ensure that the wall thickness had no further effect on the performance. In addition, all samples are both numerical and experimental weighted with help of Rhino and a very accurate scale before testing. These values are required to calculate the relative density of the samples. Moreover, visual checks are performed to see if there is any sign of warping, under- or over-extrusion.

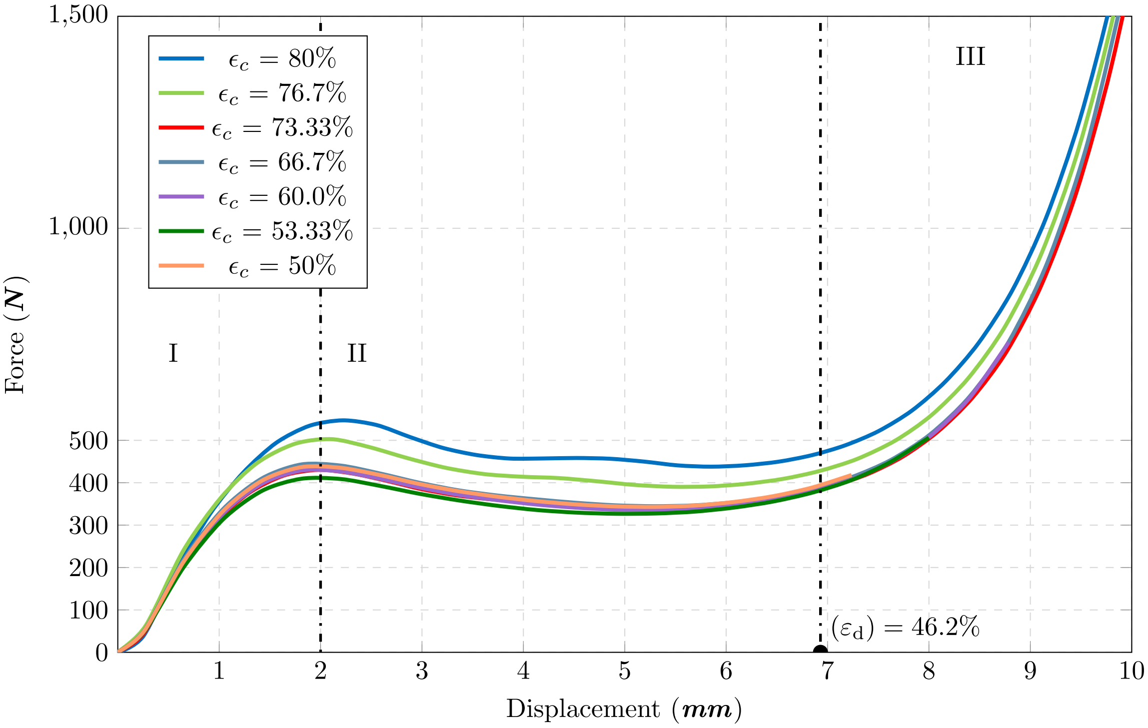

Figure 32: Force-displacement curves of sample I compressed by multiple strains. Three regions are highlighted [I] Elastic region with the linear slope, [II] Plastic region including the plateau and [III] Densification region which starts at the onset densification marked by $\epsilon_d = 46.2\%$.

5 Results and Discussion

In this section, the experimental results are described. These are obtained after achieving the objectives from section 1.2:

1. Develop a design framework to capture the unique shape and dimensions of the human head to define the surface for the helmet liner.

   By using a 3D scanning equipment, the unique shape and dimensions of the human head were recorded. This 3D scan was then imported into Rhinoceros as .STL file to define the head area to be covered by the helmet with help of SubD modelling.

2. Develop a parametric design model to create the Miura-Ori metamaterial structures.

   The Miura-Ori structure was created in Rhinoceros by using the graphical algorithm editor Grasshopper. The model was based on the geometry unit cell and was able to tessellated in all three directions, XYZ. Additionally, it was able to create MOM structures scaled to predefined dimensions.

3. Demonstrate the use of fused deposition modelling for manufacture the Miura-Ori metamaterial samples and final prototype.

   The fused deposition modelling technique was optimized for using thermoplastic polyurethane filament. Several printing parameters were calibrated and optimized to print the samples and, eventually, the prototype.

4. Experimentally test the Miura-Ori metamaterial to investigate the energy absorption capabilities.

   Quasi-static out-of-plane compression tests were conducted, and the recorded data was analyzed by using MATLAB 2022a. Stress-strain curves were obtained and the area beneath the loading curve was calculated to show the energy absorption. By weighing all the samples, the specific energy absorption could be calculated.

5. Use optimisation methods to select the optimal set of geometrical parameters for the Miura-Ori metamaterial.
   Three geometry parameters were chosen, and the optimal set were identified with help of Taguchi's method. Results were analyzed by using MINITAB Version 20. Moreover, the SEA and the S/N ratios were calculated and analysed by performing an ANOVA analysis. A optimal set of parameters was selected.

6. Generate a novel design model to apply the MOM structure to the bicycle helmet liner.

   By using GH, a novel design model was generated to apply the MOM structure to the bicycle helmet liner. The model showed that the structure was scaled to fit within the predefined area. Due to limitations, it was not possible to generate a helmet liner that bonds all the MOM structures. Hence, the helmet liner was constructed from multiple segments that have the MOM.

7. Fabricate a prototype bicycle helmet.

   By optimizing the FDM processing parameters for the TPU85a filament material, high accuracy and quality MOMs were produced. The results of this optimization allowed the manufacturing of two different prototype bicycle helmet, which consist of two parts: the harder outer shell, the MOM helmet liner. The first prototype was designed out of five parts whereas the second prototype was one complete helmet liner.

5.1 Parametric Design Model

The parametric design model that was described in section 3.3 was used to create the MOM structures. After setting the correct input parameters, and utilising the first methodology, the thickness D of 15 mm was perfectly matched. However, the length L and height H of each sample were arbitrary, see table 13. To overcome that problem, the first method was rejected and a new force-fitting methodology was described. This resulted in a perfect match of the desired sample dimensions (60 x 60 x 15 *mm*); and, it had a minor impact on the input parameters. It caused a slight deviation, which can be seen in table 14. To assure that these deviations would not affect the performance of the structures, a maximum deviation limit of 5% was set. With help of equation (7), the deviation expressed in percentages was calculated. The results in table 15 showed that the maximum error for the folding angle was 0.11%, for the dihedral angle it was 3.3% and for the cell wall ratio it was 3.6%. All deviations were under the maximum limit and therefore the parametric design model was validated. It was able to create the correct MOM structures for the experimental tests. In the end, the final results of the parametric design model are illustrated in Fig. 33. It can be seen that all nine samples were successfully created. Furthermore, each sample has its unique MOM structure, based on the input parameters of Taguchi's method and the desired sample dimensions. Further, the number of cells for each sample was different, ranging between 27 up to 92 cells.

Table 13: Overview of the dimensions and cells of the initial MOM samples

Sample	**L [mm]**	**H [mm]**	**D [mm]**	**Cells in Y**	**Cells in Z**	**Cells [-]**
1	57.47	56.55	15	8	3	45
2	58.44	53.34	15	7	3	39
3	57.33	64.33	15	7	4	52
4	57.47	55.69	15	6	3	33
5	62.59	67.98	15	6	4	44
6	58.86	53.15	15	12	4	92
7	59.85	54.82	15	5	3	27
8	62.59	54.79	15	10	3	57
9	58.96	67.23	15	9	4	68

Table 14: Overview of the analyzed geometry parameters of the forced fitting MOM samples.

Sample	(α)	(θ_A)	**(a/b)**	**Cells in Y**	**Cells in Z**	**Cells [-]**
1	9.00	19.99	1.55	8	3	45
2	8.99	35.01	2.04	7	3	39
3	8.99	50.12	2.59	7	4	52
4	9.00	20.00	2.06	6	3	33
5	9.00	36.10	2.43	6	4	44
6	9.00	49.99	1.51	12	4	92
7	8.99	20.00	2.5	5	3	27
8	9.00	36.15	1.45	10	3	57
9	9.00	49.99	2.02	9	4	68

Table 15: Overview of the deviation errors of the analysed geometrical parameters, including the maximum errors.

Sample	**Folding angle** (α)	**Dihedral angle** (θ_A)	**Cell wall ratio (a/b)**
1	0.00%	0.1%	3.3%
2	0.11%	0.0%	2.0%
3	0.11%	0.2%	3.6%
4	0.00%	0.0%	3.0%
5	0.00%	3.1%	2.8%
6	0.00%	0.0%	0.7%
7	0.11%	0.0%	0.0%
8	0.00%	3.3%	3.3%
9	0.00%	0.0%	1.0%
Maximum error	**0.11%**	**3.3%**	**3.6%**

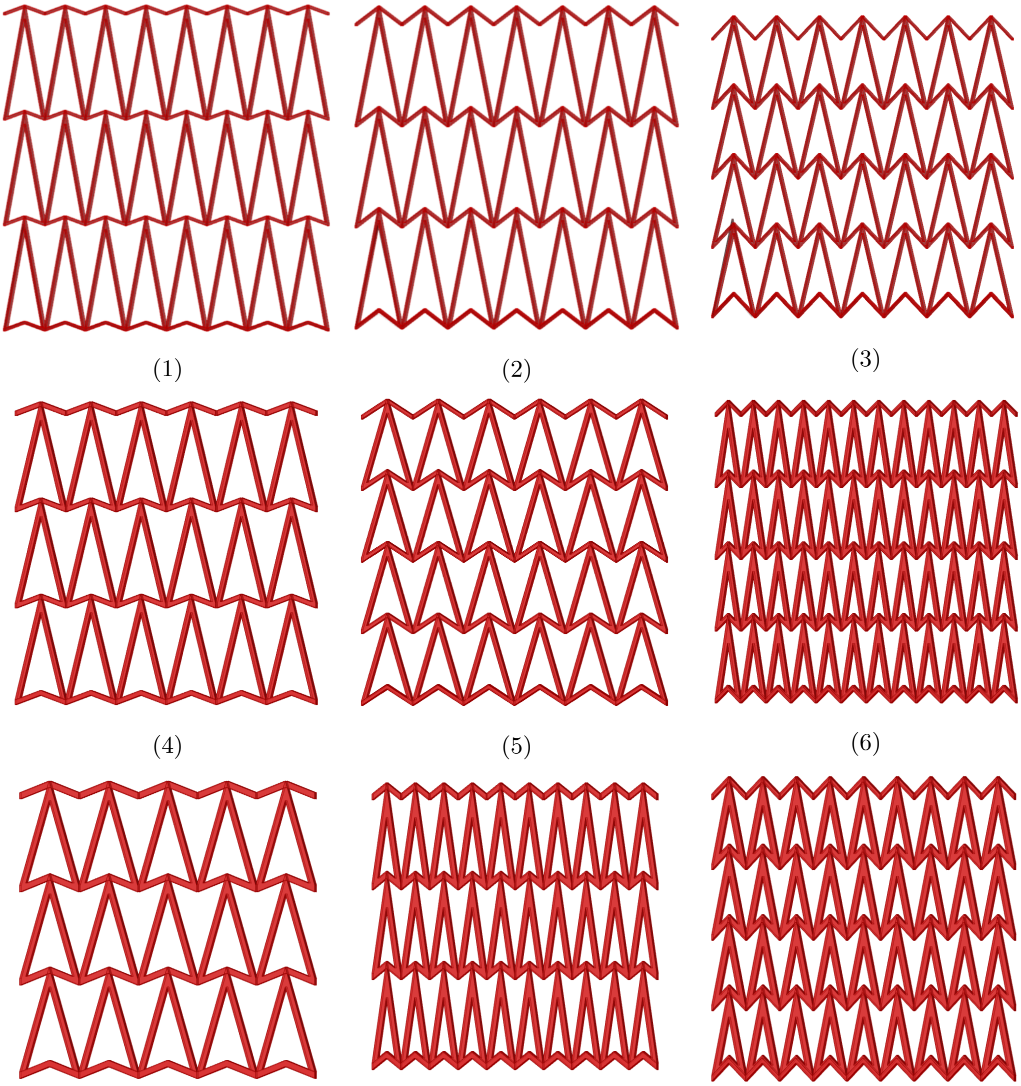

(1) (2) (3)

(4) (5) (6)

(7) (8) (9)

Figure 33: Final result of parametric design model: nine different MOM samples, 60 x 60 x 15 mm. Numbering is according to the sample number 1 - 9.

5.2 Results of FDM Printed Structures

All the samples were additive manufactured three times and each sample was visually checked for under and over extrusion, warping, see Fig. 34. Additionally, the wall thicknesses of each sample were observed. Digital calipers allowed to randomly measure walls within the structure. No major defects were recorded, the cell wall thicknesses stayed within the margin of 5%, see Appendix 7.3.1. This confirmed that the processing parameters of the FDM printer were optimized correctly. Furthermore, in the table 16 below, the results of the numerical weight, the average experimental weight and the average relative density is given per sample. The latter was calculated by using equation (10).

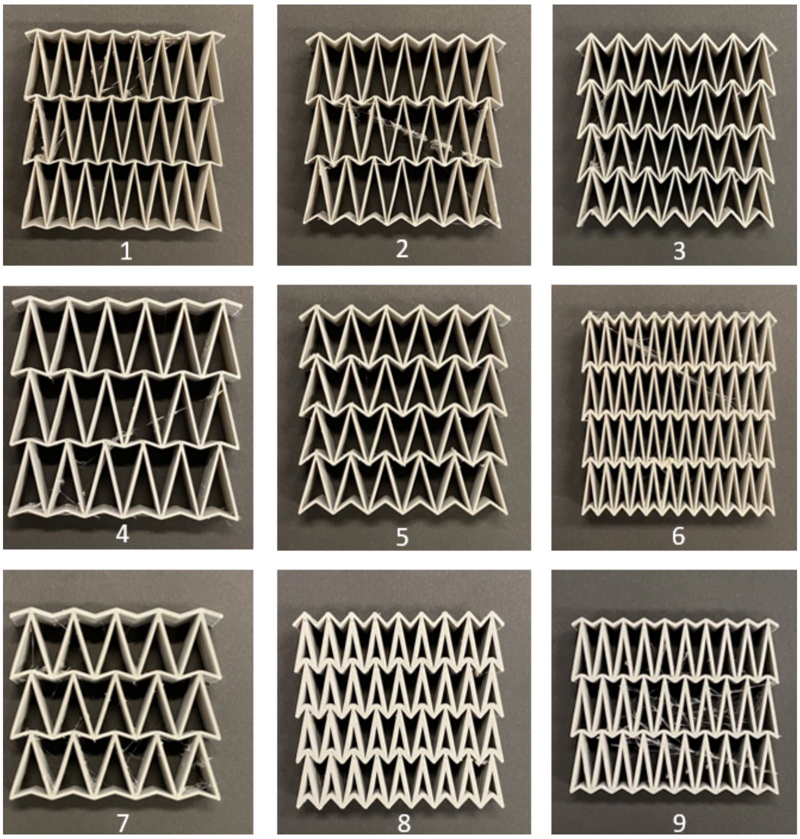

Figure 34: Overview of all nine FDM printed MOM structures 1 - 9.

Table 16: Numerical weight, average experimental weight and the average relative density of all samples.

Sample	**Num. weight [g]**	**Average exp. weight [g]**	**Average rel. density** $[kg/m^3]$
1	8	8.95	0.137
2	7	7.76	0.119
3	9	9.08	0.139
4	10	11.20	0.172
5	12	13.02	0.200
6	18	19.90	0.306
7	13	14.52	0.223
8	22	24.48	0.376
9	21	22.46	0.345

5.3 Experimental Quasi-Static Compression Results

The results of the quasi-static compression tests are presented here. Each sample was reproduced and tested three times. During analysing the results, no significant difference was observed, which concludes that the printing parameters were set correctly. The plots that have been obtained were based on the average data of the experiments. The energy absorption capabilities of the samples were investigated and were based on five properties: the peak stress (σ_p), the average plateau stress (σ_{pl}), the energy absorption (η_{EA}), the energy absorption efficiency (EA) and the specific energy absorption (SEA).

5.3.1 Force-displacement Curves

The first results were the average force N and the displacement mm of the samples. Due to the softening of the samples, the data was recorded after the fourth cycle which was also observed by other studies [30]. The force-displacement curves (FD) were created by using MATLAB version 2022a and are depicted in Fig. 35a. The average of all nine samples were plotted and it can be seen that there is a large range of force responses. Additionally, it is observed that each sample has its loading and unloading curve. The applied compression strain of 53.3% (i.e. 8 mm displacement) ensured that all samples achieved the densification region. Hence, the EA and its efficiency could be determined. To get a better view of the individual FD curves per sample, plots were created which groups the samples per wall thickness. Additionally, the directions of the loading and unloading curves were denoted. In Fig. 35a, the samples with wall thickness 0.4 *mm* were plotted. It was observed that all samples presented similar results; similar inflection points, as well as the initial slope and the peak forces. Interestingly, sample 1 exhibited a higher peak force (210 N) prior to the plateau force whereas sample 2 and 3 presented similar peak forces, 183 N. In addition, sample 1 presented a more quasi-rectangular profile with a smaller force drop and a longer plateau force. In Fig. 35b, the samples with a wall thickness of 0.7 *mm* are shown. Regarding the inflection points, sample 6 presented no clear inflection point or peak force whereas sample 4 and 5 showed similar peak forces and quasi-rectangular profiles. Sample 6 showed characteristics of a quasi-linear profiles [30]. Additionally, sample 6 has a higher peak force with a higher but shorter plateau force than sample 4 and 5. It can be seen that sample 6 reached the densification region at around 5.5 *mm* whereas sample 4 and 5 presented similar loading and unloading curves with densification at around 6-7 *mm*. Finally, in Fig. 35c, the samples with wall thickness 1.0 *mm* were presented. The inflection point for sample 9 was not clearly visible and no clear plateau force was observed, similar to sample 6 it presented a quasi-linear profile. These samples (6 and 9) presented a loading curve that was more gradually with a much shorter or almost no plateau force. Moreover, they went almost directly into densification. Distinct peak forces 850 N and 1950 N were recorded for sample 7 and 8 respectively. Regarding sample 7, the plateau force showed similarities to sample 1 and 4, once more quasi-rectangular profiles were observed. It is worth mentioning that the samples 1,4 and 7 all had the same dihedral angle of 20 *deg* but varied in thickness, cell wall ratio and relative density. Also, their plateau forces showed similar lengths prior to densification. This indicated that a lower dihedral angle caused a longer plateau force before reaching densification, which was also observed by Hanna et al [26]. Regarding the influence of the cell wall ratio (CWR), samples 1,6 and 8 had a CWR of 1.5 and all samples presented a higher initial slope and peak force compared to the samples with a CWR of 2.0 or 2.5. The force-displacement curves showed that the lower dihedral angle, the longer the plateau before densification was. Furthermore, the increase of the wall thickness caused a higher peak force and plateau force whereas increasing the CWR caused a decrease in the peak and plateau forces.

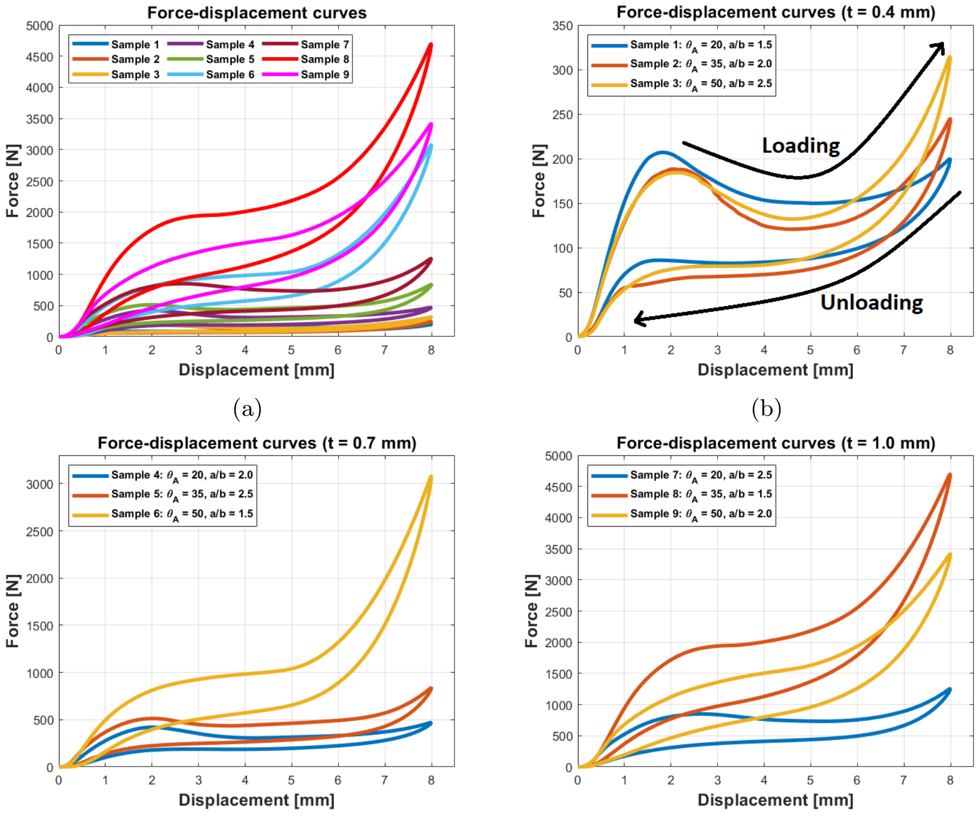

(a) (b)

(c) (d)

Figure 35: Force vs displacement curves of all nine samples [a], divided into three individual plots with different wall thicknesses t = 0.4mm including the directions of the loading and unloading curves [b], t = 0.7mm [c] and t = 1.0mm [d].

5.3.2 Stress-strain Curves

To get a better understanding of the samples, all force-displacement curves were converted to stress-strain curves. Moreover, only the loading curves were converted and are shown in Fig. 36a. The reason for that was mentioned in section 4.3.4; to calculate the energy absorbed per unit volume, the area beneath the loading curve of the stress-strain curve is needed. There were three aspects that could be observed from the curves. First, each curve showed a smooth movement behaviour that has no sudden up- or downwards movements. This indicated that the MOM structures did not undergo any plastic deformation. Furthermore, increasing the relative density caused a decrease in strain to densification; however, the plateau stress increased but decreased in length. This behaviour was noticed by other studies as well [32]. Finally, it was observed that the three regions: elastic region including the linear deformation that ends at the yield stress, plastic region with the plateau stress and the densification starting at the onset densification strain (ODS) [91]. The first property that was observed was the peak stress. In table 17 an overview is given of the peak stress and plateau stress per sample. Once more, to get a better insight on the individual results of the samples, plots were created according to the three thicknesses, 0.4, 0.7 and 1 mm respectively. In general, an uniform, flat and long stress plateau is beneficial. It will result in a higher energy absorption efficiency [93]. Moreover, the optimal structure for the bicycle helmet liner should maximise the energy absorption while minimising the applied stress. In Fig. 36b, the stress-strain curves of samples with a wall thickness of 0.4 *mm* are presented. The highest plateau stress and peak stress was achieved by sample 1 which was caused by the low CWR and dihedral angle. Increasing the CWR and the dihedral angle decreased the peak and plateau stresses but lowered the densification strain. Regarding the densification strain, it is denoted by the black dot. The samples with a wall thickness of 0.7 *mm* were presented in Fig. 36c. It is clear that sample 6 has the highest plateau and peak stress compared to sample 4 and 5. Once more, it was observed that the CWR of 1.5 caused a higher stress peak and plateau. Additionally, an increase of the dihedral angle caused an earlier densification. Regarding the relative density, sample 6 has the highest of the three: 0.306 which is an increase of 78% and 53% compared to sample 4 and 5, 0.172 and 0.200 respectively. The higher relative density could be explained to the number of cells, where sample 6 has the highest number with 92 cells. For that reason, sample 6 presented a shorter distance prior to densification. In Fig. 36d, the results of the samples with wall thickness 1.0 *mm* were depicted. It is clear to see that sample 8 presented the highest peak stress and plateau of all samples and can be observed in table 17. However, as observed at sample 6, it had one of the lowest onset densification strains. This confirmed that the increase of the relative density, increased the peak and plateau stresses but decreased the plateau length prior to densification [94]. An explanation for that could be due to the increase of wall thickness, the unit cells within the MOM structure self-contact faster. As observed at sample 1, 6 and 8, the CWR of 1.5 caused higher peak and plateau stresses. For the dihedral angle, the lower the angle, the lower the peak stress and plateau.

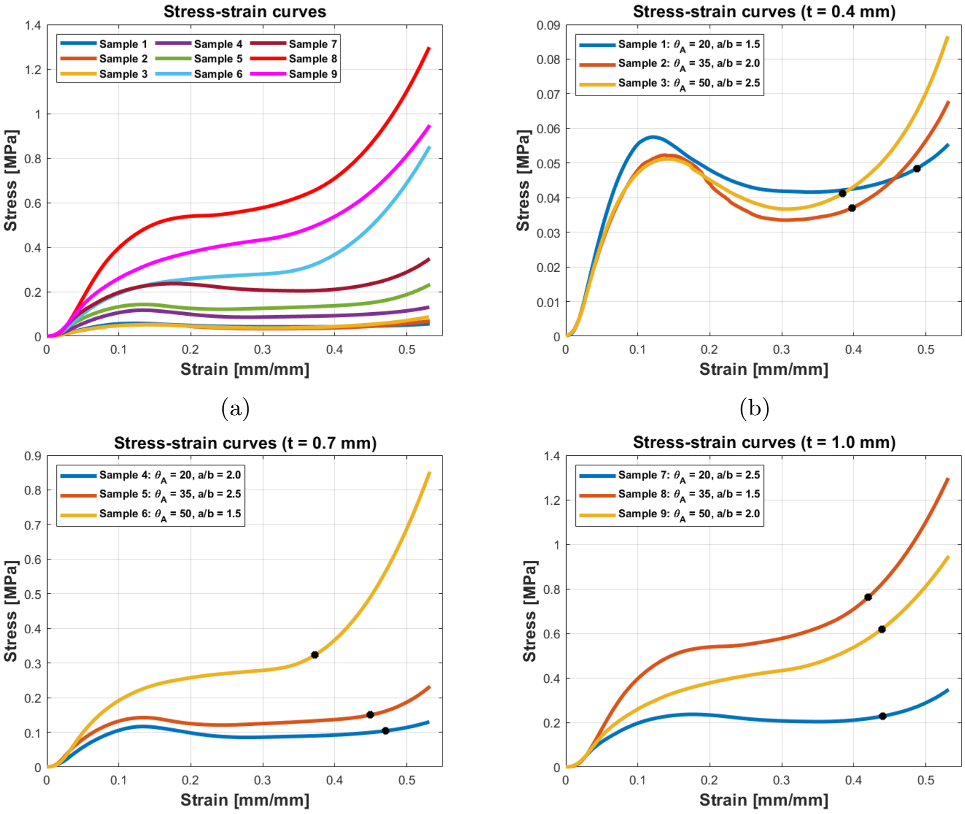

(a) (b)

(c) (d)

Figure 36: Stress-strain curves of all nine samples [a], divided into three individual plots with different wall thicknesses t = 0.4mm [b], t = 0.7mm [c] and t = 1.0mm [d].

To get a better view of the CWR and the cell wall thickness, more plots were created. Keeping the dihedral angle constant, while alternating the wall thickness and the CWR, plots for all samples were created. In Fig. 37a, samples 1,4 and 7 were plotted. It is observed that an increase of the wall thickness, which is an increase in the relative density, caused a higher peak and plateau stress. Furthermore, no significant differences were found between the densification strains. All three samples presented quasi-rectangular profiles. For samples 2,5 and 8 with a dihedral angle of 35 degrees, Fig. 37b was created. Once more, it can be seen that the increase of the relative density caused a higher peak and plateau stress where sample 8 presented a more quasi-linear profile.

Moreover, it had no significant peak stress and presents a good and long stress plateau before densification. Finally, in Fig. 37c, the samples with dihedral angle 50 were depicted. Interestingly, two of the three samples (6 and 9) presented similar results while having different wall thicknesses. Both having a quasi-linear profile but sample 6 has a significant lower densification strain. The stress-strain curves showed three promising candidates, sample 7,8 and 9 which all presented a wall thickness of 1.0 *mm*. All three having similar densification strains, see table 17. Sample 8 and 9 showed a quasi-linear profile whereas sample 7 presented a more quasi-rectangular profile. What is interesting to see is that the stress occurring in sample 8 is almost an increase of 128% compared to sample 7 and 42% compared to sample 9. This means that more stress will be present on the human head, which is undesired. However, due to the larger area beneath the loading curve, sample 8 had a higher energy absorption than sample 7 and 9. Additionally, sample 8 has the highest relative density of 0.376 whereas sample 7 has a relative density of 0.223 and sample 9, 0.345.

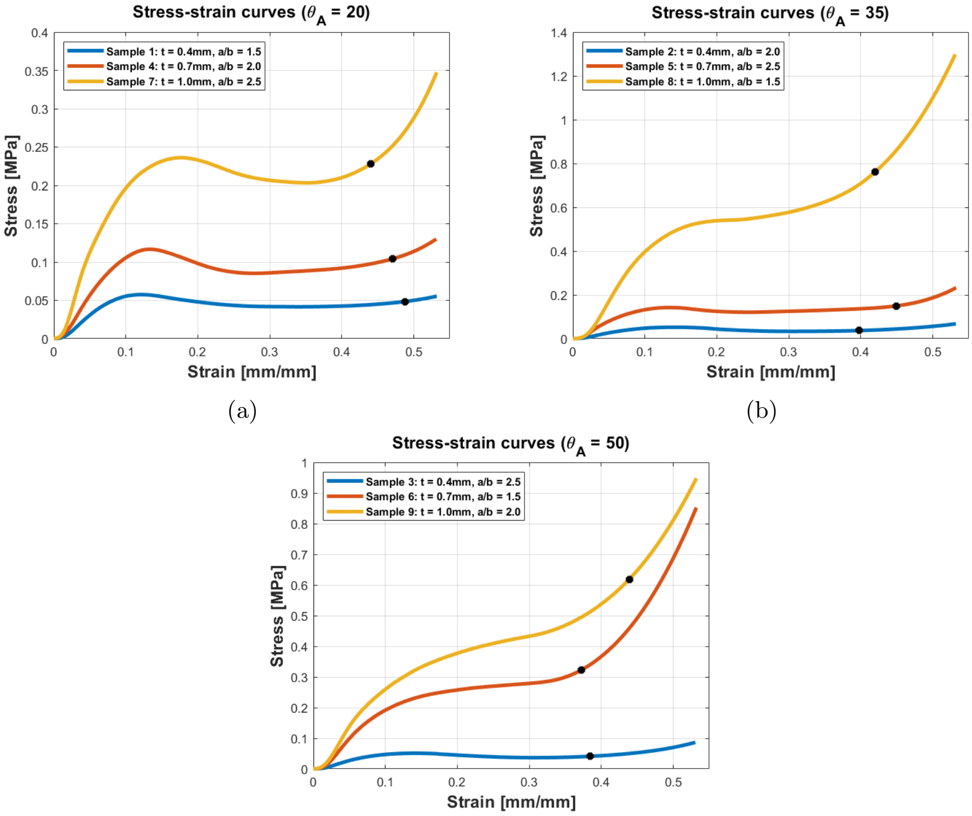

(a) (b)

(c)

Figure 37: Stress-strain curves of all nine samples [a], divided into three individual plots with different dihedral angles, $\theta_A = 20$ (samples 1,4 and 7) [a], $\theta_A = 35$ (samples 2,5 and 8) [b] and $\theta_A = 50$ (samples 3,6 and 9) [c].

5.3.3 Onset Densification Strain

The onset densification strain (ODS) defined the limit of the energy absorption area. As explained in section 4.3.2, the ODS was calculated by using the method described by Li et al. [88]. For the MOM structure, it is beneficial to delay the ODS as long as possible, to extend the plateau stress. Recall that the ODS is defined by the maximum energy absorption efficiency (EAE), which is calculated by equation (15). In Fig. 38a, it can be seen that the ODS per sample varies between 0.38 and 0.49. Additionally, table 18 illustrates a complete overview of all the average ODSs including the maximum EAE. It is interesting to see that although sample 1 presented the lowest peak stress and plateau stress, it has the highest ODS 0.49 and EAE, 42.87%. Furthermore,

Table 17: Performance parameters of all nine samples derived from the stress-strain curves

Sample	ϵ_d [-]	σ_p [MPa]	σpl [MPa]	**EA [J]**
1	0.49	0.0575	0.0426	0.0208
2	0.395	0.0523	0.0366	0.0146
3	0.38	0.0512	0.0380	0.0146
4	0.47	0.1167	0.0870	0.0409
5	0.45	0.1423	0.1181	0.0531
6	0.37	0.2590	0.2170	0.0807
7	0.44	0.2362	0.1906	0.0839
8	0.42	0.5395	0.4759	0.200
9	0.44	0.3808	0.3559	0.1561

sample 8 had the highest peak stress and plateau stress but has a significant lower EAE, 26.21%. This suggests that more volume of the MOM structure is used to absorb energy [93]. Moreover, it showed that a longer stress plateau results in a higher ODS and EAE. As stated before, promising candidates were sample 7,8 and 9. To see what the influences were of the examined geometrical parameters, Fig. 38b was presented. It was observed that by increasing the dihedral angle, both the ODS and EAE decreased. Controversially, regarding the CWR, significant influence was observed on the EAE which boasted to almost 0.4 for CWR 1.5. Furthermore, as observed in other studies, a lower dihedral angle caused a higher efficiency [71, 85].

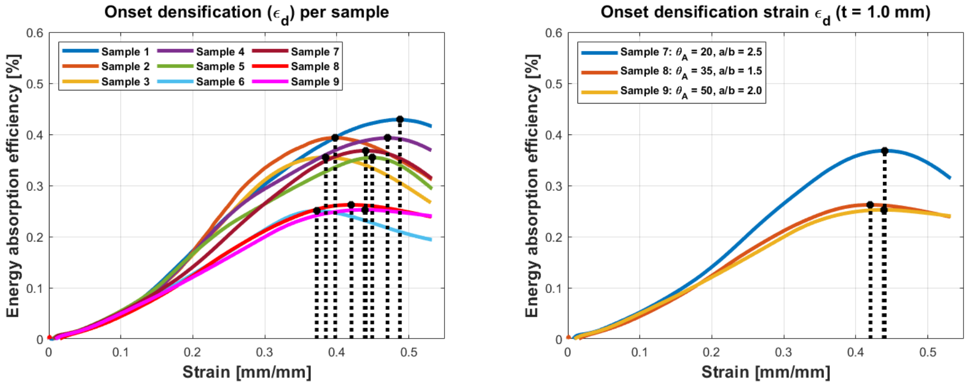

(a) (b)

Figure 38: The onset densification strain per sample 1 -9 [a], the onset densification strain including the maximum efficiency for sample 7,8 and 9 [b].

Table 18: Overview of the calculated onset densification strains and maximum efficiencies per sample.

Sample	**1**	**2**	**3**	**4**	**5**	**6**	**7**	**8**	**9**
ϵ_d [mm/mm]	**0.49**	0.395	0.38	0.47	0.45	0.37	0.44	0.42	0.44
η_{max} [%]	**42.87**	39.33	35.51	39.29	35.44	25.03	36.81	26.21	25.24

5.3.4 Energy Absorption

The data recorded during the quasi-static compression tests were converted to stress-strain curves. To recall, the absorbed energy per unit volume is equal to the area beneath the loading curve of the stress-strain plot and was calculated with equation (13). The ODS accounted for the upper bound, which means that it marked the end of the energy absorption area. In Fig. 39, an example is shown of sample 7 during the quasi-static compression test. The deformation behaviour at strains of 0, 0.18, 0,44 and 0.53 are shown with the corresponding labels. During the strain increase from 0 to 0.18 (path A-B), a linear slope was observed, which is characteristic for the elastic region. At label B, the peak stress was reached and the walls of the MOM started to collapse due to cell wall buckling. This marked the end of the elastic region, and from there a non-linear transition was initiated. At a strain of 0.2, the plastic region started, and it can be seen that the strain continued to increase while the stress dropped until it was stabilised and created the plateau stress. The energy absorption capabilities of the MOM structure are marked by the black-crossed area. This is the area beneath the loading curve up to the ODS of 0.44, see label C. From here, the stress rapidly increased up to the maximum compression strain of 0.53. At label D, it can be seen that the MOM structure is completely densified. After reaching the maximum strain, the unloading process was started and resulted in the unloading curve (path D-E). Interestingly, it does not follow the exact same path as the loading curve, which is commonly seen for TPU material [95]. This suggested that hysteresis was present in the structure, and this behaviour was observed by other studies as well [89, 96, 97]. The area highlighted in red, which is captured by the loading and unloading curve, accounted for the dissipated energy. In addition, the area highlighted in green was responsible for the recovered energy. The total volumetric energy absorbed by sample 7 was 0.084 J/mm^3. In addition, the specific energy absorption (SEA) was calculated and allowed for the normalisation of the EA (i.e. penalizes the mass of the structures), equation (2). The corresponding SEA was 5.78 J/kg. The same approach was used for all other samples, and their plots including deformation mechanisms can be found in appendix 7.3.2. The values of the EA and the SEA per sample is given in table 19. In addition, in Fig. 40a, the volumetric energy absorbed was plotted against the strain where the black dots represent the ODS per sample (i.e. the maximum absorbed energy). A complete overview of the energy absorption and SEA per sample is given in appendix 7.3.2.

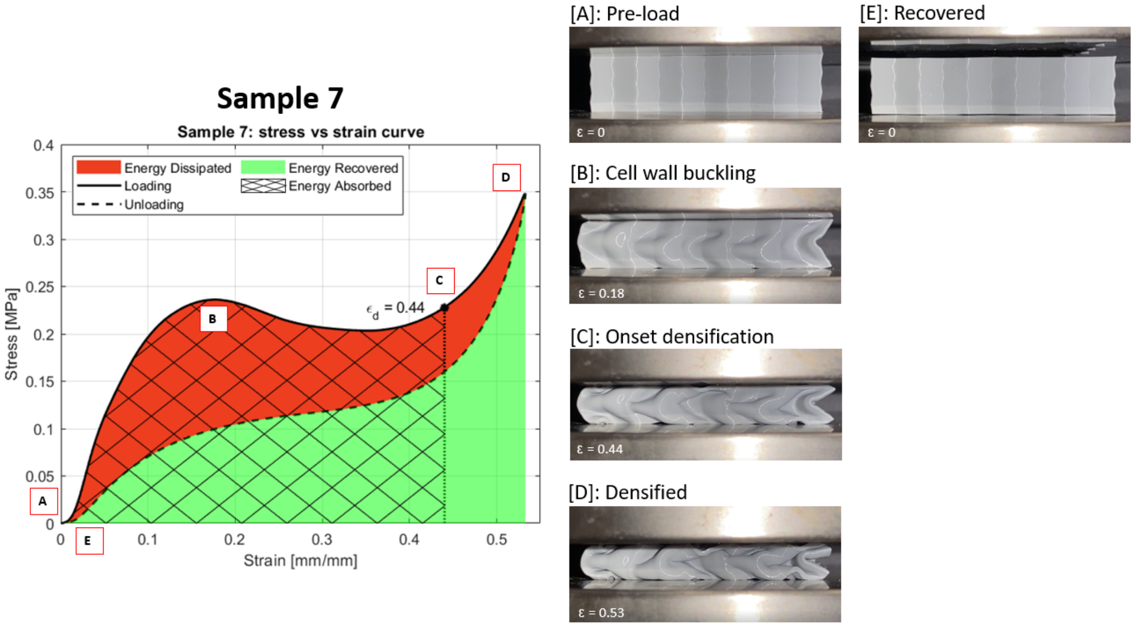

Figure 39: Stress-strain curve of sample 7 including the labels that correspond to the deformation states during the compression test. The 5 N preload [a], cell wall buckling [b], onset densification of the sample (end of energy absorption area) [c], complete densification at the maximum applied strain [d] and the recovery of the structure to its original state [e].

5.3.5 Energy Absorption Efficiency

The maximum efficiency was denoted by a single point on the curves in Fig. 40b. Normally, this value varies between 0-1. However, in reality, no structure can achieve the maximum efficiency of 1. For that to happen, the structure requires to collapsing with infinite stiffness including a

Table 19: Overview of the volumetric and specific energy absorption per sample.

Sample	**1**	**2**	**3**	**4**	**5**	**6**	**7**	**8**	**9**
EA [J/mm^3]	0.021	0.015	0.015	0.041	0.053	0.081	0.084	0.200	0.156
SEA [J/kg]	2.321	1.878	1.612	3.653	4.075	4.056	5.777	8.171	6.951

perfect flat stress plateau while having an ODS of 1.00 [96]. The maximum efficiencies of all nine samples ranged between 0.25 - 0.43. It is worth mentioning that the maximum ODS was 0.49 and therefore, the maximum efficiency is not 1 but 0.49. The highest to lowest efficiency per sample could be ordered as follows: 1-2-4-7-3-5-8-9-6, see table 18. It is interesting to see that the efficiency decreases as the relative density increases, see Fig. 40b. This could be explained with help of the stress-strain curves that were depicted in Fig. 36a. The higher density structures (6,8 and 9) presented a much shorter stress plateau, that were significantly off compared to the 'ideal' compressive profile [96]. Furthermore, in Fig. 40a, it can be seen that the increase in relative density (denoted by the black arrow), resulted in an increase of the energy absorption. Subsequently, a high density resulted in a stiff structure and thus a higher applied stress. The plot depicted in Fig. 41 showed the relation between the maximum applied force (before densification) and the resulting volumetric energy absorption. It was observed that sample 8 exhibited the highest strength followed by sample 9 and 6. Regarding the energy absorption, sample 8 presented the highest followed by sample 9 and 7. It is clear to see that the samples with a wall thickness of 1.0 *mm* present the best strength and the highest energy absorbed. In the end, sample 8 presented the best performance in terms of EA and SEA, 0.200 *J* and 8.171 *J/kg* respectively. Compared to other studies where they investigated TPU honeycomb structures [30, 96], with similar relative densities, 0.21 and 0.22, they absorbed 0.028 and 0.089 *J*. Sample 7 has a relative density of 0.2, similar to the above two structures and absorbed 0.084 *J* which is an increase of 200% compared to the honeycomb structure of [96] and a decrease of 5% compared to the origami honeycomb structure of [30]. This concluded that the MOM structures showed promising results and are competitive with the current honeycomb structures.

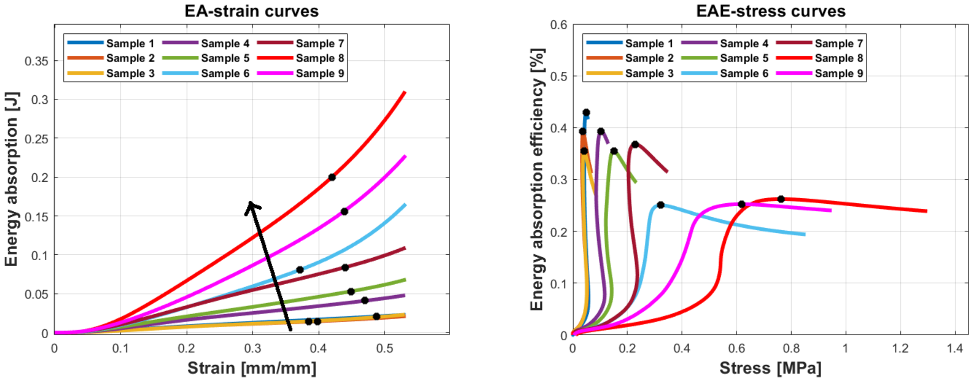

(a)

(b)

Figure 40: Energy absorption-strain curves including the onset densification strains [a] and the energy absorption efficiency-stress curves including maximum efficiency [b].

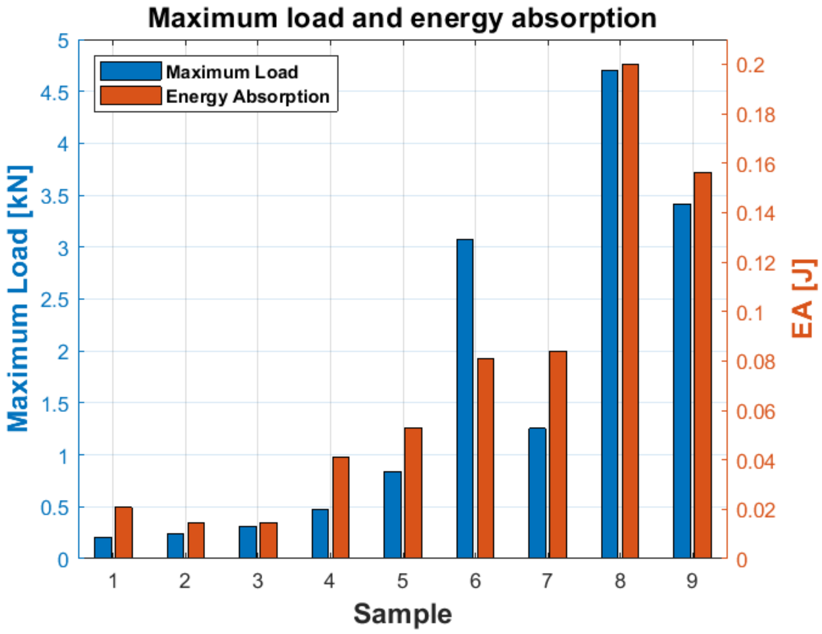

Figure 41: The maximum force applied before densification versus the energy absorbed per sample.

5.4 Taguchi's L9 Results

The MOM samples were manufactured as defined in section 3.2.1 after which they were quasi-static compressed. The objective was to calculate the SEA per sample and in total nine different experiments were conducted. Recall that the 'larger the better' method was selected to get the most out of the reaction, see equation (3). The resulting signal-to-noise (S/N) ratios were statistically studied with help of ANOVA in MINITAB version 20. To check the contribution of the geometrical parameters on the SEA. The average values of SEA and the S/N ratios are shown in table 20. It can be seen that sample 8 was responsible for the highest SEA and S/N ratio, whereas sample 3 showed the lowest for both.

Table 20: Experimental results for all nine samples with their calculated SEA and S/N ratios.

Exp.	**Controllable geometry parameters**			**Experimental results**	**S/N Ratios of results (Larger the Better)**
	t [mm]	θ_A *[deg]*	*a/b [-]*	*Average SEA [J/kg]*	*S/N [dB]*
1	0.4	20	1.5	2.3211	7.3139
2	0.4	35	2.0	1.8774	5.4711
3	0.4	50	2.5	1.6115	4.1446
4	0.7	20	2.0	3.6529	11.2528
5	0.7	35	2.5	4.0747	12.2019
6	0.7	50	1.5	4.0557	12.1613
7	1.0	20	2.5	5.7769	15.2339
8	1.0	35	1.5	8.1710	18.2455
9	1.0	50	2.0	6.9505	16.8403

5.4.1 Effect of Geometrical Parameters on SEA

Three geometrical parameters were selected to investigate their influence on the SEA. In Fig. 42, it was observed that the SEA increased with the increase of the wall thickness. This behavior

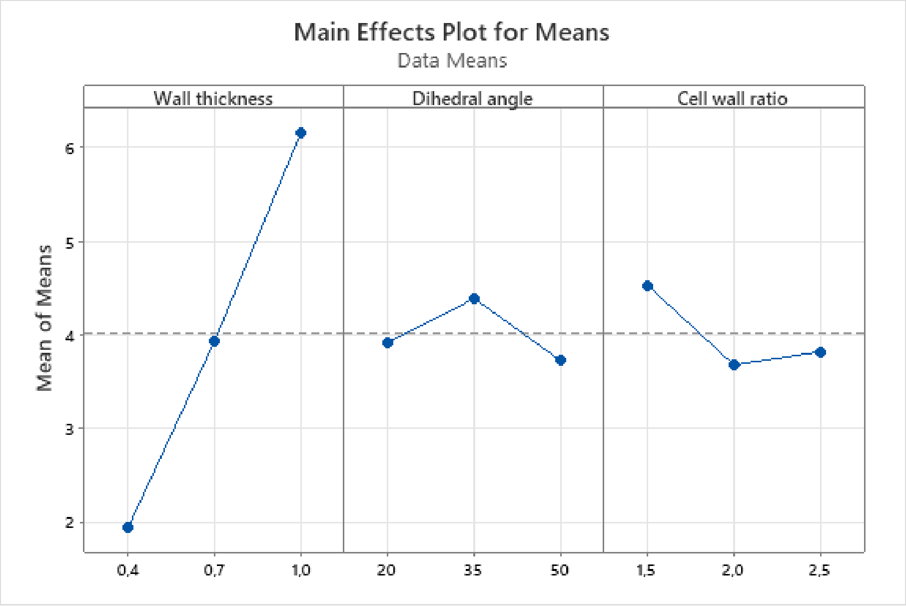

Figure 42: Main effects plot of geometrical parameters on SEA.

was observed by others where the wall thickness lead to an increase of the relative density. The stress-strain curves that were observed in section 5.3.2 showed that the MOM structures with a higher relative density absorbed more energy. This was also observed by other studies done to similar TPU structures [26, 98]. Moreover, a higher relative density was less prone to cell wall buckling as the slenderness was less. Regarding the dihedral angle, it was observed that an angle of 35 degrees was the most optimal. By grouping the samples into three groups: 0.4, 0.7 and 1.0 *mm*, it was noticed that samples two samples out of three (5 and 8) had this angle and presented the highest SEA and S/N ratio within their group. One exception was sample 2 that had the same dihedral angle but not the highest values within the group. This could be explained with the help of table 16, where it was observed that sample 2 had a lower relative density than sample 1. Interestingly, Hanna et al. concluded that a dihedral angle of 20 degrees was the most optimal [26]. However, their objective was different to this study and a larger dihedral angle allowed more unit cells within the plane of the MOM structure, see table 14. An increase of the unit cells resulted in a higher relative density, where a dihedral angle of 35 degrees was concluded to be the optimum. Finally, the effect of the cell wall ratio (CWR) was noticed, with an increase in the ratio causing a drop in the SEA. The ideal CWR was 1.5, which was unexpected. A study done by Zhang et al. [71] concluded that an increase in the CWR would significantly increase the SEA. Constrastingly, the main effects plot and the results in table 20 showed that a CWR of 2.5 was responsible for the lowest SEA within their group. Once more, it can be seen that sample 8 was implemented with the CWR of 1.5 and was one of the highest performers.

5.4.2 Selection of Optimum Geometry Parameters for SEA

The results of the 'Larger the Better' S/N ratios are presented in table 21. Furthermore, in Fig. 43, the main effects plot of S/N ratio for SEA was depicted. To recall, a larger S/N ratio equals to a small difference between the measured and desired output [99]. This indicates that the larger the delta value, the bigger the effect that specific parameter had on the SEA, and the lower the delta, the worse. As a result, it can be observed from the ranking that the wall thickness was number one, the cell wall ratio number two and the dihedral angle number three. In addition, it was observed that the highest mean S/N ratios were achieved by the following selection: a wall thickness of 1.0 *mm*, a dihedral angle of 35 degrees and a CWR of 1.5. These values have been marked in table 21 and correspond to the levels 3,2 and 1, respectively. The optimal selection was further denoted as $t_3 - \theta_2 - a/b_1$.

Table 21: Overview of the mean S/N ratio per level for SEA.

Parameter	Name	Mean S/N Ratio Level 1	Level 2	Level 3	Delta	Rank
t	Wall thickness [mm]	5.643	11.872	**16.773**	11.130	1
θ_A	Dihedral angle [deg]	11.267	**11.973**	10.049	0.924	3
a/b	Cell wall ratio [-]	**12.574**	11.188	10.527	2.047	2

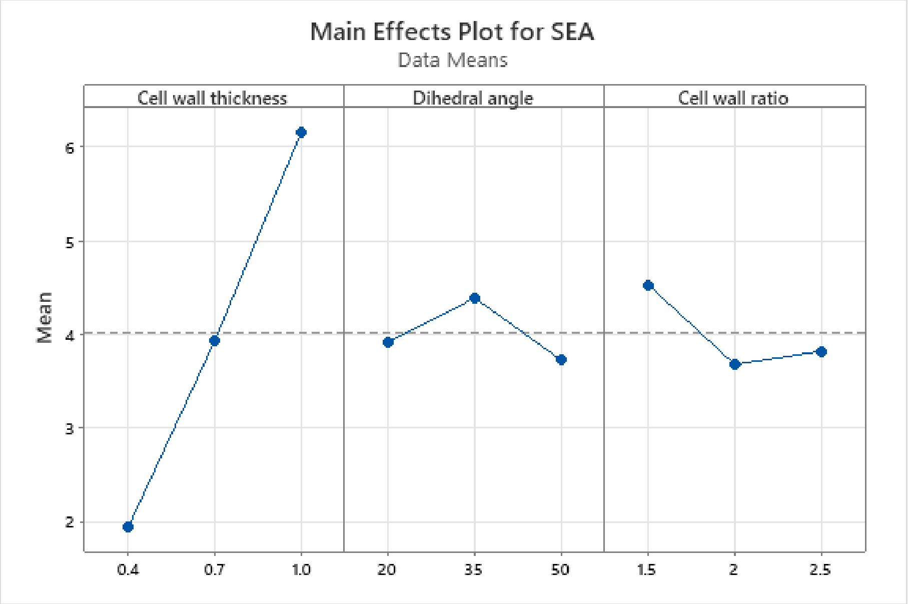

Figure 43: Main effects plot of S/N ratio for SEA.

5.4.3 ANOVA for Specific Energy Absorption

ANOVA was utilized to calculate and understand the contribution of each geometrical parameter to the SEA. The results of the ANOVA are presented in table 22, and it was observed that the SEA was significantly influenced by the wall thickness. The contribution of the wall thickness was 94.83% whereas the dihedral angle and the CWR accounted for 0.7% and 3.33% only. Such a significant contribution of the wall thickness was in agreement with the study done by Hanna et al. [26]. No clear explanation was found for the low contribution of both the dihedral angle and the CWR. Finally, for validating the selection of the optimal geometrical parameters, a confirmation analysis was conducted.

Table 22: ANOVA of specific energy absorption.

Source	DoF	SS	MS	Total contribution [%]
t	2	186.70	93.35	94.83
θ_A	2	1.40	0.7	0.7
a/b	2	6.55	3.275	3.33
Residual Error	2	2.24	1.12	1.14
Total	8	196.88		100

5.4.4 Validation of Selected Geometry Parameters for SEA

Taguchi's method was validated by calculating the predicted S/N ratio that corresponds to the optimal selection of geometry parameters found in section 5.4.2: $t_3 - \theta_2 - a/b_1$. To calculate the predicted S/N ratio, equation (16) was utilized, and both results can be found in table 23. It was observed that the predicted SEA was 7.97 *J/kg*, with an S/N ratio of 18.46. When compared to the experimental results, it is evident that there was an increase of 2.51% for the SEA and an improvement of 0.2 for the S/N ratio. This confirmed that the predicted values were close to the experimental results. Furthermore, it showed a favourable improvement for both the SEA and S/N ratio.

Table 23: Validation of the test results for SEA.

	Optimal geometry parameters	
	Prediction	**Experimental**
Level set	$t_3 - \theta_2 - a/b_1$	$t_3 - \theta_2 - a/b_1$
SEA [J/kg]	7.97	8.17
S/N Ratio [dB]	18.06	18.26
Improvement in S/N ratio [dB]	-0.2	
Percentage difference of SEA	2.51 %	

To further analyse the agreement of the predicted values, a linear regression model was created in MINITAB version 20. The mathematical model for the SEA was developed as a function of the three geometrical parameters: the wall thickness, the dihedral angle and the cell wall ratio. As a result, the following predictive equation (16) was obtained:

$$\mathbf{SEA} = 0.13 + 8.382t + 0.0096\theta_A - 1.028a/b \qquad (\mathbf{R^2} = \mathbf{95.03}\%) \tag{16}$$

where the t is the wall thickness, θ_A is the dihedral angle and a/b the cell wall ratio. Furthermore, the R^2 denoted a value of 95.03% and was known as the coefficient of determination. It is a value between 0 and 1 and measures how well the model can predict the desired outcome [100]. In other words, the closer the value is to 1, the better the fit and therefore the agreement between the predicted and experimental values. The observed value of R^2 suggests that the model can almost perfectly predict the SEA. In addition, a residual plot was created and can be seen in Fig. 44. It is worth mentioning that if the line is straight, the residual errors are normally distributed and the coefficients of the model are significant [99]. The plot depicted in the figure confirmed that the predictive model was indeed significant. In the end, to validate the predictive model, samples of the Taguchi's L9 were randomly selected: 1,4,7 and 9. The results are shown in table 24, and it was observed that there was a strong agreement between both the predictive and experimental results.

Table 24: Predictive and experimental results for randomly selected samples of Taguchi's L9 with the predictive model.

Run	**Experimental SEA [J/kg]**	**Predicted SEA [J/kg]**	**Residuals SEA [J/kg]**	**Error %**
1	2.32	2.25	0.07	3.1
4	3.65	3.55	0.1	2.8
7	5.78	6.05	-0.27	4.5
9	6.95	6.78	0.17	2.5

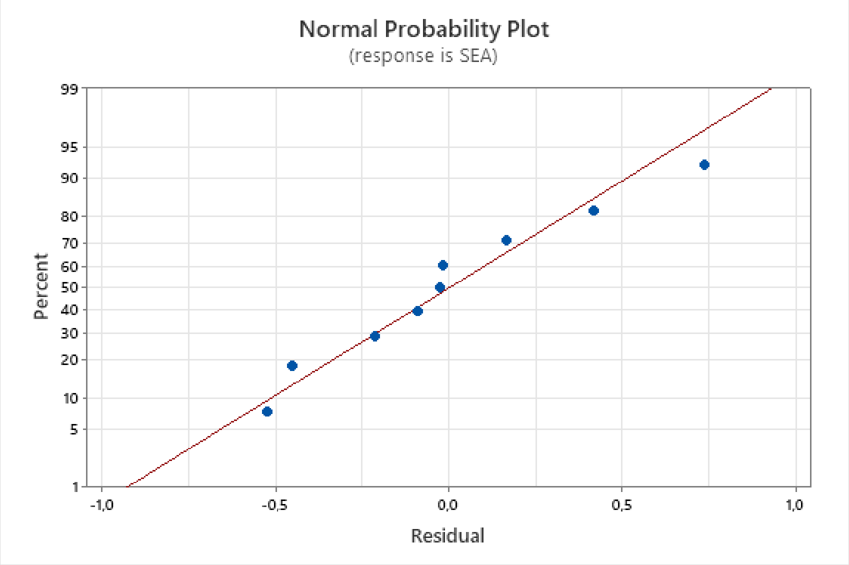

Figure 44: Normal probability plot of the residuals for SEA.

5.5 Results of Helmet Liner Design

The final design for the helmet liner was achieved by using the GH design model described in section 3.4.1. An overview is given in Fig. 45 which depicts the MOM custom-fit bicycle helmet liner and consists of two parts: the outer shell and the MOM liner. It can be seen that the helmet liner follows the shape of the human head. The front view highlights the two ventilation gaps which can also be used to carry the goggles of the user. The other gaps located in the outer shell have no function and are only used to give a better insight of the helmet liner. Moreover, as shown in Fig. 46, the MOM helmet liner really captures the dome-like shape. For manufacturing the prototype of the final design, two types were designed. The objective was to print the helmet liner without the need of supports. Hence, different approaches were defined in section 3.4.2. The first prototype was based on the five segments of the helmet liner: front, top, right, left and back, see

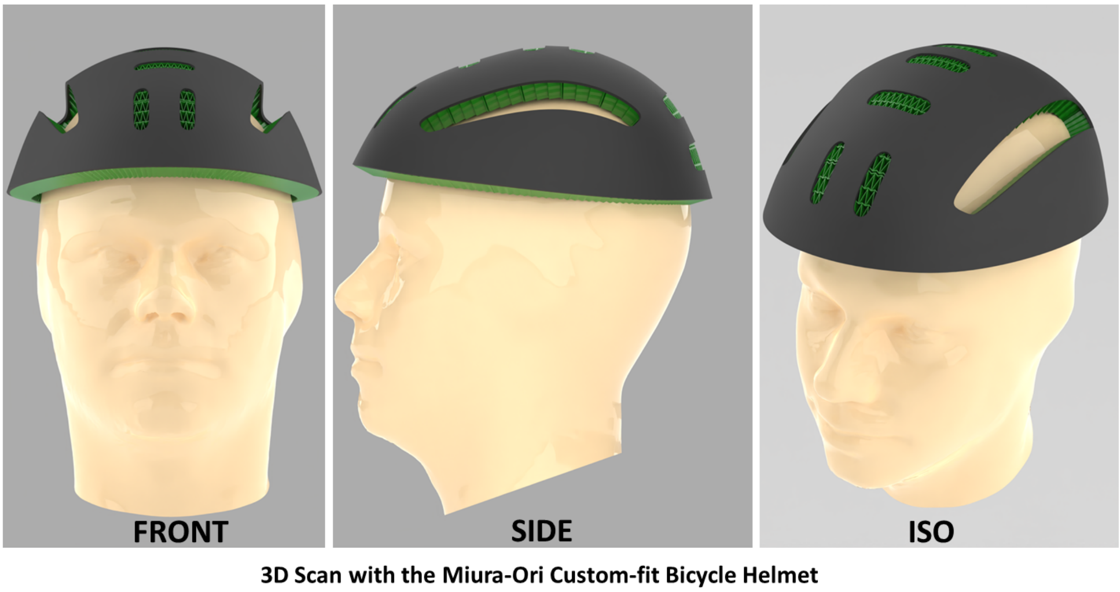

Figure 45: The final design of the Miura-Ori Custom-fit bicycle helmet liner including the 3D scan and the outer shell. Front, side and iso view.

Fig. 47. It can be seen that the MOM was applied to all the flat segments. For applying the MOM, the graded approach was used and allows the MOM to be fitted within the segments. Moreover, the MOM structure is graded which means that the unit cells are scaled to comply with the shape of the segment. All the segments were able to be additive manufactured by using the Creality Ender 5 Pro. The second prototype was was based on the complete helmet liner and trimmed approach. Moreover, the five segments were merged together and formed one uniform helmet liner. The MOM structure was applied according to the GH model and by using the outer perimeter of the design, the MOM structure was trimmed. In fig. 48, it can be seen that the structure was trimmed to fit within the helmet liner surface. Additionally, an outer wall was created to hold the structure together. The complete helmet liner was used for the second prototype where it must be placed inside the outer shell. The complete helmet liner is then formed according to the curvature of the outer shell.

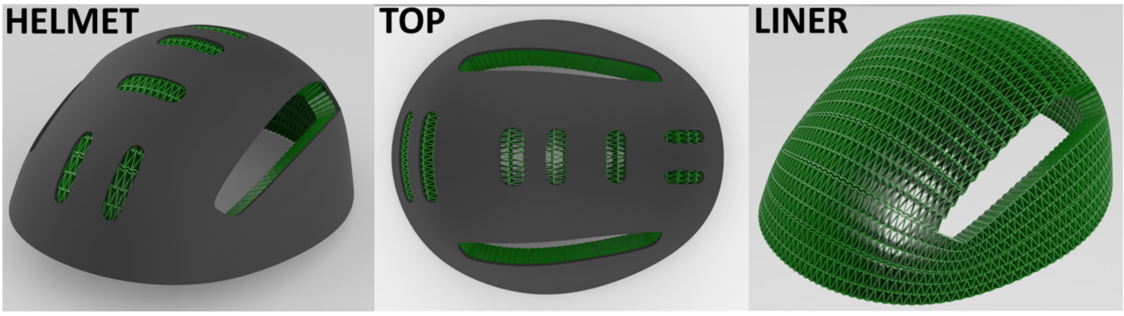

Figure 46: The final design of the Miura-Ori Custom-fit bicycle helmet liner including the outer shell.

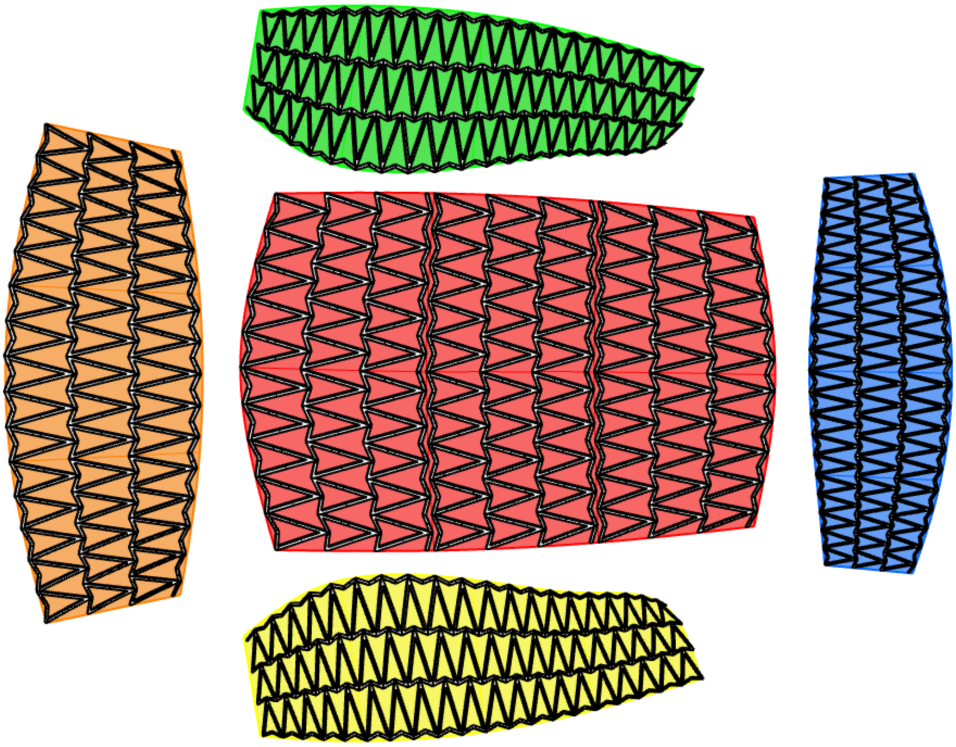

Figure 47: The MOM applied to the five segments of the helmet liner by using the graded approach.

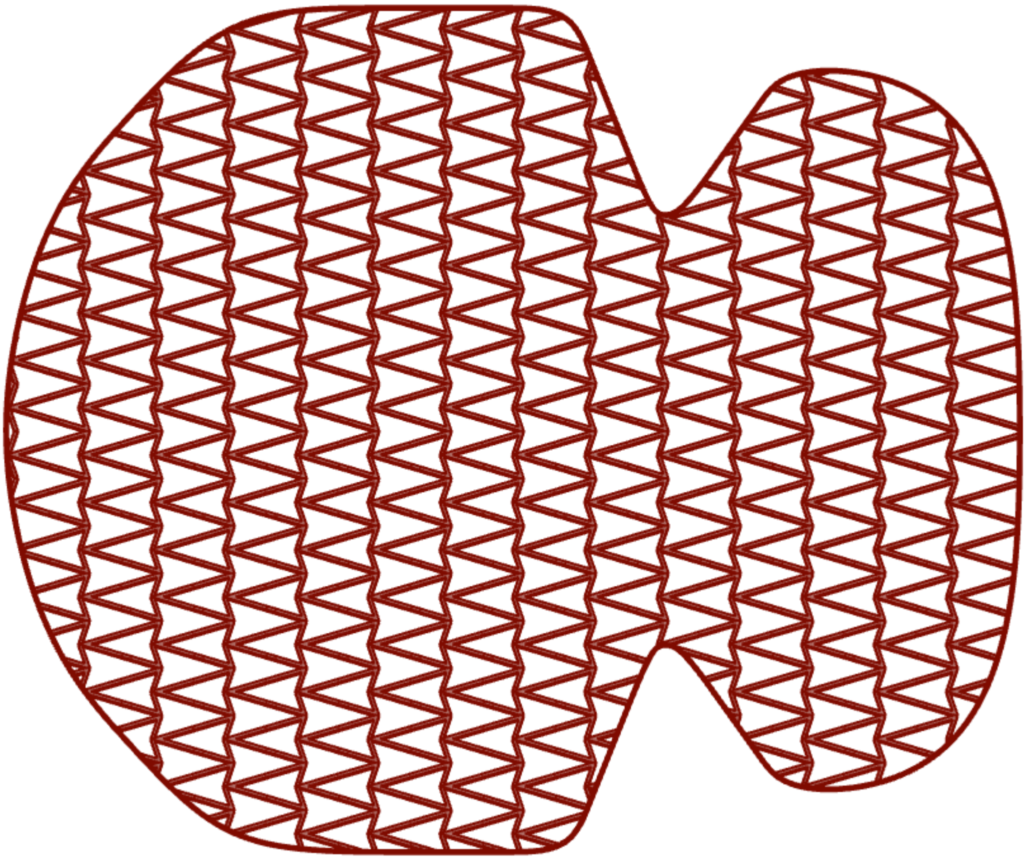

Figure 48: The complete MOM helmet liner based on the trimmed approach.

5.6 Results of Prototype Bicycle Helmet Liner

For the manufacturing of the prototypes, the same technique was used as for the MOM samples. Furthermore, the same optimized printing parameters were used as shown in table 9 in section 3.4.3. The first prototype consisted of five parts that were individually printed, see Fig. 49a. The total printing time was 27 hours and 29 minutes and as shown in table 25, the top part had the longest printing time. Additionally, the individual weights per segment are shown as well. The heaviest part was the top part whereas the lightest part was the front part. The numerical weight was calculated with help of Rhinoceros and the total weight of all the segments was 142 g. For the actual weight, the individual additive manufactured segments were weighted with a digital scale. The total actual weight was 150.9 g. There was a good agreement between the numerical and actual weight, this concluded that the printing parameters were optimized well.

Table 25: Overview of the printing time, numerical weight and actual weight per part of the first prototype.

Segment	**Printing time [h]**	**Numerical weight [g]**	**Actual weight [g]**
Front	4.31	21	24.3
Back	4.52	25	23.1
Top	8.54	48	52.5
Left	5.01	24	25.6
Right	5.01	24	25.4
Total	27.29	142	150.9

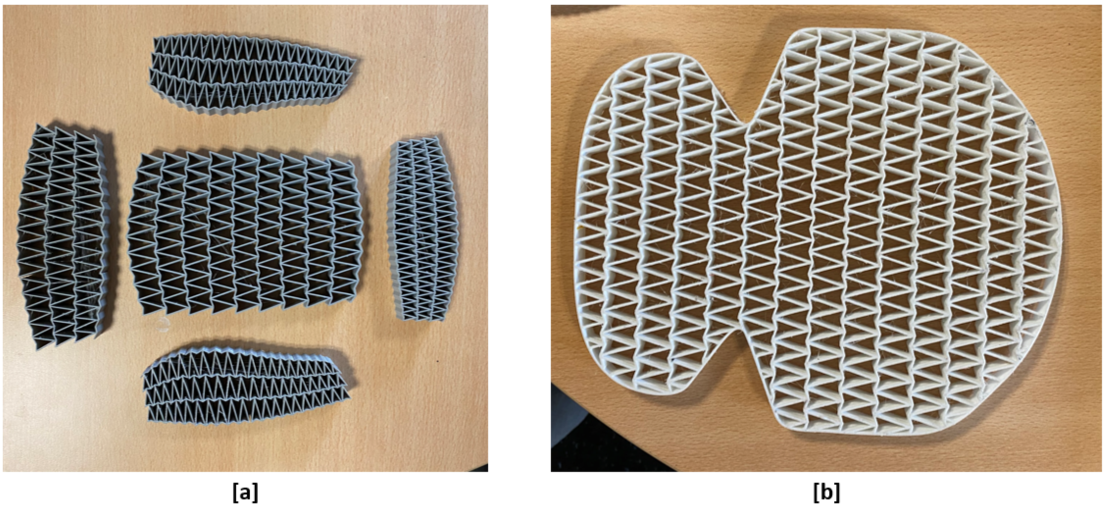
[a] [b]

Figure 49: The additive manufactured prototypes. Prototype 1 [a] and prototype 2 [b].

For the second prototype, the complete helmet liner, the total printing time was 17 hours and 30 minutes, see Fig. 49b. This prototype was externally printed as it was larger than the printing bed of the Creality Ender 5 Pro. The numerical weight was calculated to a total of 230.95 g and after weighing the additive manufactured liner, the total actual weight was 244.45 g.

Table 26: Overview of the printing time, numerical weight and actual weight per part of the second prototype.

Part	**Printing time [h]**	**Numerical weight [g]**	**Actual weight [g]**
MOM Liner	17.5	230.95	244.45
Total	17.5	230.95	244.45

Additionally, an outer shell was additive manufactured but had no influence on the performance. It was only made for illustration purpose only. The results are depicted in Fig. 50, additionally the prototype was mounted inside the shell. This resulted in the complete and final Miura-Ori custom-fit bicycle helmet, see Fig. 51.


[a] [b] [c] [d]

Figure 50: The 3D printed outer shell from PLA, the top view [a], the side view [b], the back view [c] and the isometric view [d].

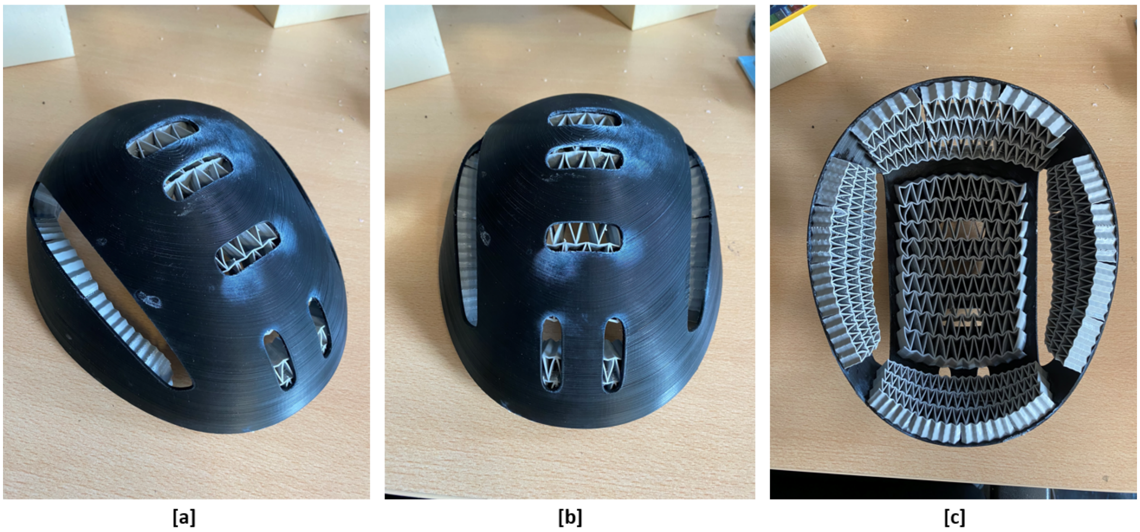

Figure 51: Prototype 1 fitted in the harder outer shell, isometric view [a], back view [b] and inside view [c].

6 Conclusion

This section will offer an overview of the most important research major results. It concludes their contribution and makes recommendations for further research, including limits. The main aim of this thesis was to develop a novel method to improve the fit of bicycle helmets and to design a Miura-Ori metamaterial based helmet liner. A set of objectives were provided to attain these goals:

- Develop a design framework to capture the unique shape and dimensions of the human head.
- Develop a parametric design model to create the Miura-Ori metamaterial structures.
- Demonstrate the use of fused deposition modelling to manufacture Miura-Ori metamaterial samples and final prototype.
- Experimentally test the Miura-Ori metamaterial to investigate the energy absorption capabilities.
- Use optimization methods to select the optimal set of geometrical parameters for the Miura-Ori metamaterial.
- Fabricate a prototype bicycle helmet including a helmet liner.

The current bicycle helmets, based on the head circumference of the headforms, are outdated. The improper fit causes discomfort for most of the users, and therefore the users become more reluctant to wear helmets. The main cause is the incorrect design process, where the sizing does not account for the unique head shapes and dimensions. The solution is to design a custom-fit helmet liner by using reverse engineering and a 3D scanning equipment. In comparison to previous research, this work employs more precise 3D scanning technology, and the proposed design technique is based on several 3D scans that capture the unique form and proportions of the human head. Furthermore, a design model was created where the 3D scan could be imported after which the helmet liner area could be identified. In addition to providing a custom-fit helmet liner, the design showed an approach that could be used by other individuals.

The literature review identified the promising Miura-Ori metamaterial, which presented a large set of geometrical parameters that could be optimized to achieve high specific energy absorption. Moreover, it offered a candidate structure that allowed for optimization to improve its functionality and performance. The structure is generated by stacking the individual Miura-Ori sheets. The obvious solution for that is to use Rhinoceros and the graphical algorithm editor, Grasshopper. Usually, this method is used to create parametric models for complex structures and geometries, but not for Miura-Ori metamaterials. As a result, this study bridged that gap by proposing a parametric design methodology for developing the Miura-Ori metamaterial. The model allows the input of the desired geometrical parameters, after which it generates the individual sheets, A and B. The final structure is realized by stacking the sheets in all three directions, XYZ. The result is a novel parametric design model that enables the generation of the Miura-Ori metamaterial that can be applied for multiple purposes.

Thermoplastic urethane presented several properties that are favourable to act as the base material for the Miura-Ori metamaterial. However, the complex geometry could not be manufactured by conventional methods. Therefore, additive manufacturing was investigated and presented a viable technique called fused deposition modelling. This technique is capable of manufacturing parts while keeping a high accuracy and low manufacturing time. Although the filament is known for years, no optimal printing parameters were found for manufacturing the thermoplastic polyurethane Miura-Ori metamaterial. The literature review showed that little to no studies defined a set of printing parameters. Hence, the printing parameters were optimized to ensure the repeatability and reliability of the Miura-Ori metamaterial samples. The manufactured samples showed dimensions and weights within the accepted range. Additionally, visual checks were done and no warping, under or over extrusion was detected.

Three promising geometrical parameters were selected: wall thickness, dihedral angle and the cell wall ratio, and used in Taguchi's method. This developed nine different Miura-Ori metamaterial samples with the dimensions 60 x 60 x 15 *mm*. To discover the out-of-plane energy absorption capabilities, quasi-static compression tests were conducted. The manufactured samples presented a large performance range and showed more scope for optimization. Strain-softening was observed for the first three cycles, after which it stabilised. The increase of the wall thickness resulted in a higher relative density and made the samples less prone to cell wall buckling. Subsequently, the energy absorption was increased but the efficiency and the onset densification strain were decreased. The highest onset densification strain was 0.49 by sample 1 whereas the recorded absorption efficiencies peaked as high as 0.43 with a maximum energy absorption by sample 8 of 0.200 *J* and a SEA of 8.171 *J/kg*.

The main effect plots presented the most optimal set of geometrical parameters that provided the maximum performance of the Miura-Ori metamaterial. To investigate which geometrical parameters were most influential, in relation to the specific energy absorption, ANOVA analysis was used. The optimal set of parameters is the wall thickness of 1.0 *mm*, the dihedral angle of 35 degrees and the cell wall ratio of 1.5. The ANOVA presented significant contribution of the wall thickness to the specific energy absorption, 94.83%. Followed by the cell wall ratio and the dihedral angle for 0.7% and 3.33% respectively. The high contribution of the wall thickness is in relation with the number of cells. The more cells within the sample, the more volume is filled. As a result, the other parameters presented very low contributions. They were limited to contribute to the SEA. Additionally, via mathematical modelling, a predicted model was created. The model enabled good predictions of the SEA and showed strong agreements compared to the experimental results, with a confidence level of 95.03%.

The prototype bicycle helmet liner consists of an outer shell and the custom-fit Miura-Ori metamaterial helmet liner, with a total weight of the MOM helmet liner of 150.9 gram. Both were additively built successfully using the fused deposition modeling approach using PLA and TPU85a filaments, respectively. The prototype is an accurate depiction of the finished product.

6.1 Recommendations and Future Work

This research presented the possibility for applying the Miura-Ori metamaterial for bicycle helmet liners. Furthermore, a design framework was presented to improve the fit of the helmet by using reverse engineering and 3D scanning equipment. Despite significant attempts to optimize the MOM, there are still recommendations for further development.

6.1.1 Future Work

The area of the human head that should be protected must be better defined. In this work, the area was based on other bicycle helmets, however, it would be useful to discover which areas of the human head are most sensitive to injuries. Although the parametric design model was able to create the MOM structure, there were some limitations. The model used multiple sub-models to apply the MOM structure to the helmet liner. However, it was not able to create one uniform liner. The reason for that was that the quads of the individual surfaces could not be aligned in the same direction. Therefore, in a following study, a parametric design model should be created that enables one uniform helmet liner.

For manufacturing the MOM samples, the FDM technique was utilized. This technique is limited due to the nozzle diameter, 0.4 *mm*. As a result, it was not possible to investigate the possibility of manufacturing smaller MOM structures. A smaller nozzle diameter could manufacture thinner cell walls, and it is believed that via Taguchi's method, in combination with ANOVA, the contribution of the wall thickness could be significantly reduced. Moreover, lower relative densities can be achieved. Another recommendation would be to use another additive manufacturing technique, such as Selective Laser Sintering (SLS). The FDM technique is limited to printing the complete helmet liner, including the curvature. It does not allow the use of supports and therefore, the MOM helmet liner was printed flat, after which the curvature was applied by pressing it into the outer shell. The SLS technique enables the manufacturing of the helmet liner, including the desired curvature, without the need of supports. In addition, this would enable the experimental testing of the curved MOM samples.

Regarding the energy absorption capabilities, quasi-static out-of-plane compression tests were conducted. Although the samples were tested multiple times and enough data was recorded, no tests were done to study the rotational accelerations. For future research, other tests must be conducted, including other testing setups. Tests such as a dynamic impact test or impact loading test offer the possibility to study the behavior better. To see if the MOM structure can stay below the $300g$ acceleration that was defined in the safety standard EN1078. Additionally, according to this standard, a minimum of $55J$ should be absorbed to stay beneath the limit. The total thickness investigated in this work was 15 *mm* however, increasing this thickness could improve the energy absorption capabilities. Although the thickness could improve the energy absorption, it should be noted that increasing the total thickness could significantly change the total weight. Furthermore, it changes the comfort of the helmet.

Tensile tests were conducted to investigate the mechanical properties of TPU85A, however more research must be done to understand the material. Moreover, to better understand the deformation behaviour of the MOM structures. Hence, in future work, hyperelastic model must be created, including the hysteresis effects, to conduct numerical simulations. It would help to understand the mechanical behavior of the samples. The out-of-plane compression tests do not allow to see the inside of the structures and, therefore, it is not possible to see their behavior such as cell wall buckling.

6.1.2 Recommendations

Finally, for choosing the optimal structure, two candidates were identified. The first one does not consider weight optimisation for the bicycle helmet. From the results, both from the quasi-static compression and the ANOVA analysis, it was clear that sample 8 presented the highest EA and SEA, 0.20 *J* and 8.171 *J/kg* respectively. Additionally, the ANOVA results showed that sample 8 had the highest S/N ratio for the SEA, 18.246. However, it was the sample with the highest weight 24.48 *g* and had a maximum efficiency of 26.21% only. In terms of designing a bicycle helmet liner that provides the maximum SEA without any weight restrictions, sample 8 should be considered. Controversially, it is important to keep the weight of the helmet liner as low as possible but providing sufficient energy absorption capabilities. Moreover, to provide room for more optimisations in terms of SEA. From the results, sample 7 presents a much higher efficiency of 36.81%, an ODS of 0.44 and had a much lower weight of 14.52 *g*. The EA and SEA were 0.084 *J* and 5.77 *J/kg*. Sample 7 presented a weight reduction of 40.6% while having a 10% improved energy absorption efficiency. Although it has a much lower EA compared to sample 8, the weight is one of the top drivers for customers to buy a new bicycle helmet. In the end, the total weight should not be higher than the current helmets.

References

[1] "Bicycle helmet history URL: https://helmets.org/history.html."

[2] E. Standards, "BS EN 960:2006 headforms for use in the testing of protective helmets."

[3] R. Ball, C. Shu, P. Xi, M. Rioux, Y. Luximon, and J. Molenbroek, "A comparison between chinese and caucasian head shapes," vol. 41, no. 6, pp. 832–839.

[4] "DEKRA verkehrssicherheitsreport archiv URL: https://www.dekra-roadsafety.com/de/archiv/."

[5] M. Schenk and S. D. Guest, "Geometry of miura-folded metamaterials," vol. 110, no. 9, pp. 3276–3281. Publisher: National Academy of Sciences Section: Physical Sciences.

[6] L. Laker, "Europe doubles down on cycling in post-covid recovery plans,"

[7] R. Buehler and J. Pucher, "COVID-19 impacts on cycling, 2019–2020," vol. 41, no. 4, pp. 393–400. Publisher: Routledge _eprint: https://doi.org/10.1080/01441647.2021.1914900.

[8] C. Malm, J. Jakobsson, and A. Isaksson, "Physical activity and sports—real health benefits: A review with insight into the public health of sweden," vol. 7, no. 5, p. 127.

[9] T. Götschi, J. Garrard, and B. Giles-Corti, "Cycling as a part of daily life: A review of health perspectives," vol. 36, no. 1, pp. 45–71. Publisher: Routledge _eprint: https://doi.org/10.1080/01441647.2015.1057877.

[10] F. Abayazid, K. Ding, K. Zimmerman, H. Stigson, and M. Ghajari, "A new assessment of bicycle helmets: The brain injury mitigation effects of new technologies in oblique impacts," vol. 49, no. 10, pp. 2716–2733.

[11] M. Rizzi, H. Stigson, and M. Krafft, *Cyclist Injuries Leading to Permanent Medical Impairment in Sweden and the Effect of Bicycle Helmets.* Journal Abbreviation: 2013 IRCOBI Conference Proceedings - International Research Council on the Biomechanics of Injury Publication Title: 2013 IRCOBI Conference Proceedings - International Research Council on the Biomechanics of Injury.

[12] C. P. Bogerd, S. Annaheim, P. Halldin, M. Houtenbos, D. Otte, D. Shinar, I. Walker, and R. Willinger, "HOPE: Helmet optimization in europe. the final report of COST action TU1101,"

[13] N. Dodds, R. Johnson, B. Walton, O. Bouamra, D. Yates, F. Lecky, and J. Thompson, "Evaluating the impact of cycle helmet use on severe traumatic brain injury and death in a national cohort of over 11000 pedal cyclists: A retrospective study from the NHS england trauma audit and research network dataset," vol. 9, p. e027845.

[14] W. Peeters, R. van den Brande, S. Polinder, A. Brazinova, E. W. Steyerberg, H. F. Lingsma, and A. I. R. Maas, "Epidemiology of traumatic brain injury in europe," vol. 157, no. 10, pp. 1683–1696.

[15] S. Piland, T. Gould, M. Jesunathadas, J. Wiggins, O. McNair, and S. Caswell, "Protective helmet in sports," pp. 71–121.

[16] S. P. Soe, P. Martin, M. Jones, M. Robinson, and P. Theobald, "Feasibility of optimising bicycle helmet design safety through the use of additive manufactured TPE cellular structures," vol. 79, no. 9, pp. 1975–1982.

[17] E. J. Alfrey, M. Tracy, J. R. Alfrey, M. Carroll, E. D. Aranda-Wikman, T. Arora, J. Maa, and J. Minnis, "Helmet usage reduces serious head injury without decreasing concussion after bicycle riders crash," vol. 257, pp. 593–596.

[18] P. A. Cripton, D. M. Dressler, C. A. Stuart, C. R. Dennison, and D. Richards, "Bicycle helmets are highly effective at preventing head injury during head impact: head-form accelerations and injury criteria for helmeted and unhelmeted impacts," vol. 70, pp. 1–7.

[19] R. D. Ledesma, D. Shinar, P. M. Valero-Mora, N. Haworth, O. E. Ferraro, A. Morandi, M. Papadakaki, G. De Bruyne, D. Otte, and M. Saplioglu, "Psychosocial factors associated with helmet use by adult cyclists," vol. 65, pp. 376–388.

[20] W. H. Organization, *Helmets: A Road Safety Manual for Decision-Makers and Practitioners*. World Health Organization. Google-Books-ID: DcstPwAACAAJ.

[21] A. L. DeMarco, D. D. Chimich, S. J. Bonin, and G. P. Siegmund, "Impact performance of certified bicycle helmets below, on and above the test line," vol. 48, no. 1, pp. 58–67.

[22] T. Ellena, H. Mustafa, A. Subic, and T. Y. Pang, "A design framework for the mass customisation of custom-fit bicycle helmet models," vol. 64, pp. 122–133.

[23] Z. Zhuang, S. Benson, and D. Viscusi, "Digital 3-d headforms with facial features representative of the current US workforce," vol. 53, no. 5, pp. 661–671. Publisher: Taylor & Francis _eprint: https://doi.org/10.1080/00140130903581656.

[24] F. P. Rivara, S. J. Astley, S. K. Clarren, D. C. Thompson, and R. S. Thompson, "Fit of bicycle safety helmets and risk of head injuries in children," vol. 5, no. 3, pp. 194–197.

[25] D.-S. Liu, C.-Y. Chang, C.-M. Fan, and S.-L. Hsu, "Influence of environmental factors on energy absorption degradation of polystyrene foam in protective helmets," vol. 10, pp. 581–591.

[26] B. Hanna, R. Adams, S. Townsend, M. Robinson, S. Soe, M. Stewart, R. Burek, and P. Theobald, "Auxetic metamaterial optimisation for head impact mitigation in american football," vol. 157.

[27] B. R. Krishnan, A. N. Biswas, K. V. Ahalya Kumar, and P. S. Rama Sreekanth, "Auxetic structure metamaterial for crash safety of sports helmet,"

[28] B. J. Ramirez and V. Gupta, "Evaluation of novel temperature-stable viscoelastic polyurea foams as helmet liner materials," vol. 137, pp. 298–304.

[29] K. Wang, Y.-H. Chang, Y. Chen, C. Zhang, and B. Wang, "Designable dual-material auxetic metamaterials using three-dimensional printing," vol. 67, pp. 159–164.

[30] M. Robinson, S. Soe, G. McShane, R. Celeghini, R. Burek, M. Alves, B. Hanna, and P. Theobald, "Developing elastomeric cellular structures for multiple head impacts," vol. 2017-September, pp. 182–189. ISSN: 2235-3151.

[31] A. Jaisingh Sheoran and H. Kumar, "Fused deposition modeling process parameters optimization and effect on mechanical properties and part quality: Review and reflection on present research," vol. 21, pp. 1659–1672.

[32] J.-H. Kim and G.-H. Kim, "Effect of rubber content on abrasion resistance and tensile properties of thermoplastic polyurethane (TPU)/rubber blends," vol. 22, no. 5, pp. 523–527.

[33] J. H. Park and J. R. Lee, "Developing fall-impact protection pad with 3d mesh curved surface structure using 3d printing technology," vol. 11, no. 11, p. 1800. Number: 11 Publisher: Multidisciplinary Digital Publishing Institute.

[34] H. Lee, R.-i. Eom, and Y. Lee, "Evaluation of the mechanical properties of porous thermoplastic polyurethane obtained by 3d printing for protective gear," vol. 2019, p. e5838361. Publisher: Hindawi.

[35] C. Zerpa, M. Liu, and S. Parihar, "AN IMPROVED CYCLING HELMET TECHNOLOGY TO MITIGATE HEAD INJURIES," vol. 38, no. 1, p. 80.

[36] R. Cushman, R. Pless, D. Hope, and C. Jenkins, “Trends in bicycle helmet use in ottawa from 1988 to 1991.,” vol. 146, no. 9, pp. 1581–1585.

[37] J. Abderezaei, F. Rezayaraghi, B. Kain, A. Menichetti, and M. Kurt, “An overview of the effectiveness of bicycle helmet designs in impact testing,” vol. 9, p. 793.

[38] L. T. Chang, G. L. Chang, J. Z. Huang, S. C. Huang, D. S. Liu, and C. H. Chang, “Finite element analysis of the effect of motorcycle helmet materials against impact velocity,” vol. 26, no. 6, pp. 835–843.

[39] P. Siegkas, D. J. Sharp, and M. Ghajari, “The traumatic brain injury mitigation effects of a new viscoelastic add-on liner,” vol. 9, no. 1, p. 3471. Bandiera_abtest: a Cc_license_type: cc_by Cg_type: Nature Research Journals Number: 1 Primary_atype: Research Publisher: Nature Publishing Group Subject_term: Biomedical engineering;White matter injury Subject_term_id: biomedical-engineering;white-matter-injury.

[40] K. T. Thai, A. S. McIntosh, and T. Y. Pang, “Factors affecting motorcycle helmet use: size selection, stability, and position,” vol. 16, pp. 276–282.

[41] “AS/NZS 2063:2020 URL: https://www.standards.org.au/standards-catalogue/sa-snz/consumer/cs-110-1/{designation}.”

[42] “ASTM f1447: Standard specification for helmets used in recreational bicycling or roller skating URL: https://www.astm.org/f1447-18.html.”

[43] “NEN-EN 1078:2012+a1:2012 en URL: https://www.nen.nl/en/nen-en-1078-2012-a1-2012-en-177571.”

[44] “U.s. consumer product safety commission URL: https://www.cpsc.gov/safety-education/safety-guides/sports-fitness-and-recreation-bicycles/which-helmet-which-activity.”

[45] “Snell helmets certification - standard b-95 URL: https://smf.org/standards/pdf/b95rev.pdf.”

[46] A. Alderson, K. L. Alderson, D. Attard, K. E. Evans, R. Gatt, J. N. Grima, W. Miller, N. Ravirala, C. W. Smith, and K. Zied, “Elastic constants of 3-, 4- and 6-connected chiral and anti-chiral honeycombs subject to uniaxial in-plane loading,” vol. 70, no. 7, pp. 1042–1048. Number: 7 Publisher: Pergamon.

[47] K. T. Thai, A. S. McIntosh, and T. Y. Pang, “Bicycle helmet size, adjustment, and stability,” vol. 16, no. 3, pp. 268–275. Publisher: Taylor & Francis _eprint: https://doi.org/10.1080/15389588.2014.931948.

[48] J. Pucher and R. Buehler, “Making cycling irresistible: Lessons from the netherlands, denmark and germany,” vol. 28, no. 4, pp. 495–528. Publisher: Routledge _eprint: https://doi.org/10.1080/01441640701806612.

[49] E. Villamor, S. Hammer, and A. Martinez-Olaizola, “Barriers to bicycle helmet use among dutch paediatricians,” vol. 34, no. 6, pp. 743–747.

[50] C. C. Piotrowski, L. Warda, C. Pankratz, K. Dubberley, K. Russell, H. Assam, and M. Carevic, “The perspectives of young people on barriers to and facilitators of bicycle helmet and booster seat use,” vol. 46, no. 5, pp. 591–598. _eprint: https://onlinelibrary.wiley.com/doi/pdf/10.1111/cch.12791.

[51] J. T. Finnoff, E. R. Laskowski, K. L. Altman, and N. N. Diehl, “Barriers to bicycle helmet use,” vol. 108, no. 1, p. E4.

[52] C. Rissel and L. M. Wen, “The possible effect on frequency of cycling if mandatory bicycle helmet legislation was repealed in sydney, australia: a cross sectional survey,” vol. 22, no. 3, pp. 178–183.

[53] J. Webster, “The perception of comfort and fit of personal protective equipment in sport.”

[54] N. R. Romanow, B. E. Hagel, J. Williamson, and B. H. Rowe, “Cyclist head and facial injury risk in relation to helmet fit: a case-control study,” vol. 34, no. 1, pp. 1–7.

[55] T. L. Teng, C. C. Liang, C. J. Shih, and V. H. Nguyen, “Design and analysis of bicycle helmet with impaxx foam liner,” vol. 706-708, pp. 1778–1781. Conference Name: Mechatronics and Intelligent Materials III ISBN: 9783037857106 Publisher: Trans Tech Publications Ltd.

[56] L. Foster, P. Peketi, T. Allen, T. Senior, O. Duncan, and A. Alderson, “Application of auxetic foam in sports helmets,” vol. 8, no. 3, p. 354. Number: 3 Publisher: Multidisciplinary Digital Publishing Institute.

[57] “WaveCel bicycle helmet URL: https://wavecel.com/.”

[58] s. pakzad, a. shah hoseini, M. Dehghani, and a. b. khalkhali, “Design and analysis of bicycle helmet made of PETg and ABS with honeycomb structure against external impacts using abaqus software,” vol. 14, no. 1, pp. 83–90. Publisher: Islamic Azad University Majlesi Branch _eprint: http://admt.iaumajlesi.ac.ir/article_681380_c095252ee8a5d5b5c7a988649afbf77c.pdf.

[59] J. C. Najmon, D. J. Jacob, Z. M. Wood, and A. Tovar, “Cellular helmet liner design through bio-inspired structures and topology optimization of compliant mechanism lattices,” vol. 6, no. 3, pp. 217–236. Publisher: SAE International.

[60] A. A. Naderi, “Blast resistance of an innovative helmet liner composed of an auxetic lattice structure,” vol. 0. Publisher: Amirkabir University of Technology.

[61] A. L. Wickeler and H. E. Naguib, “3d printed geometrically tessellated sheets with origami-inspired patterns,” p. 0021955X211061838. Publisher: SAGE Publications Ltd STM.

[62] “HEXR’s breakthrough safety test results URL: https://hexr.com/blogs/all/hexrs-breakthrough-safety-test-results.”

[63] T. Y. Pang, T. S. T. Lo, T. Ellena, H. Mustafa, J. Babalija, and A. Subic, “Fit, stability and comfort assessment of custom-fitted bicycle helmet inner liner designs, based on 3d anthropometric data,” vol. 68, pp. 240–248.

[64] “KAV - custom bike and hockey helmets URL: https://kavsports.com/.”

[65] R. Tang, H. Huang, H. Tu, H. Liang, M. Liang, Z. Song, Y. Xu, H. Jiang, and H. Yu, “Origami-enabled deformable silicon solar cells,” vol. 104, pp. 083501–083501.

[66] X. M. Xiang, G. Lu, and Z. You, “Energy absorption of origami inspired structures and materials,” vol. 157, p. 107130.

[67] Y. Hu, Y. Zhou, and H. Liang, “Constructing rigid-foldable generalized miura-ori tessellations for curved surfaces,” vol. 13, no. 1.

[68] N. Turner, B. Goodwine, and M. Sen, “A review of origami applications in mechanical engineering,” vol. 230, no. 14, pp. 2345–2362. Publisher: IMECHE.

[69] P. Jackson, *Folding Techniques for Designers*. Laurence King Publishing.

[70] Y. Mosleh, J. Vander Sloten, B. Depreitere, and J. Ivens, “Novel composite foam concept for head protection in oblique impacts,” vol. 19, no. 10, p. 1700059. _eprint: https://onlinelibrary.wiley.com/doi/pdf/10.1002/adem.201700059.

[71] J. Zhang, D. Karagiozova, Z. You, Y. Chen, and G. Lu, “Quasi-static large deformation compressive behaviour of origami-based metamaterials,” vol. 153-154, pp. 194–207.

[72] J. A. Harris and G. J. McShane, “Metallic stacked origami cellular materials: Additive manufacturing, properties, and modelling,” vol. 185-186, pp. 448–466.

[73] X. Xiang, W. Qiang, B. Hou, P. Tran, and G. Lu, "Quasi-static and dynamic mechanical properties of miura-ori metamaterials," vol. 157, p. 106993.

[74] R. Adams, S. Townsend, S. Soe, and P. Theobald, "Finite element-based optimisation of an elastomeric honeycomb for impact mitigation in helmet liners," vol. 214, p. 106920.

[75] D. Faraci, L. Driemeier, and C. Comi, "Bending-dominated auxetic materials for wearable protective devices against impact," vol. 7, no. 3, pp. 425–435.

[76] S. Li, Z. Xiao, Y. Zhang, and Q. M. Li, "Impact analysis of a honeycomb-filled motorcycle helmet based on coupled head-helmet modelling," vol. 199, p. 106406.

[77] Y. Lv, Y. Zhang, N. Gong, Z.-x. Li, G. Lu, and X. Xiang, "On the out-of-plane compression of a miura-ori patterned sheet," vol. 161-162, p. 105022.

[78] K. Chynybekova and S.-M. Choi, "Flexible patterns for soft 3d printed fabrications," vol. 11, no. 11, p. 1398. Number: 11 Publisher: Multidisciplinary Digital Publishing Institute.

[79] P. Wang, J. Yang, Y. Hu, J. Huo, and X. Feng, "Innovative design of a helmet based on reverse engineering and 3d printing," vol. 60, no. 3, pp. 3445–3453.

[80] M. Sokovic and J. Kopac, "RE (reverse engineering) as necessary phase by rapid product development," vol. 175, no. 1, pp. 398–403.

[81] R. Mendřický and O. Langer, "Influence of the material on the accuracy of optical 3d digitalisation," vol. 2019, pp. 2783–2789.

[82] E. Dimas and D. Briassoulis, "3d geometric modelling based on NURBS: a review," vol. 30, no. 9, pp. 741–751.

[83] M. N. Islam and A. Pramanik, "Comparison of design of experiments via traditional and taguchi method," vol. 15, no. 3, pp. 151–160. Publisher: World Scientific Publishing Co.

[84] R. K. Roy, *Design of Experiments Using The Taguchi Approach: 16 Steps to Product and Process Improvement.* John Wiley & Sons. Google-Books-ID: 6zq3c3FaCq8C.

[85] J. A. Harris and G. J. McShane, "Impact response of metallic stacked origami cellular materials," vol. 147, p. 103730.

[86] M. Mehrpouya, T. Edelijn, M. Ibrahim, A. Mohebshahedin, A. Gisario, and M. Barletta, "Functional behavior and energy absorption characteristics of additively manufactured smart sandwich structures," vol. n/a, p. 2200677. _eprint: https://onlinelibrary.wiley.com/doi/pdf/10.1002/adem.202200677.

[87] "ISO 37:2017 URL: https://www.iso.org/cms/render/."

[88] Q. Li, I. Magkiriadis, and J. Harrigan, "Compressive strain at the onset of densification of cellular solids," vol. 42, pp. 371–392.

[89] H. Qi and M. Boyce, "Stress-strain behavior of thermoplastic polyurethanes," vol. 37, pp. 817–839.

[90] M. León-Calero, S. C. Reyburn Valés, Marcos-Fernández, and J. Rodríguez-Hernandez, "3d printing of thermoplastic elastomers: Role of the chemical composition and printing parameters in the production of parts with controlled energy absorption and damping capacity," vol. 13, no. 20, p. 3551. Number: 20 Publisher: Multidisciplinary Digital Publishing Institute.

[91] L. J. Gibson and M. F. Ashby, *Cellular Solids: Structure and Properties.* Cambridge Solid State Science Series, Cambridge University Press, 2 ed.

[92] Q. Cheng, J. Yin, J. Wen, and D. Yu, "Mechanical properties and energy absorption performance of 3d-printed hierarchical structures based on sierpinski triangles."

[93] A. Belbasis, F. Fuss, B. Hazel, and M. Schlegel, *Foam mechanics: evaluating performance based on energy absorption at optimal strain.*

[94] S. Xu, J. H. Beynon, D. Ruan, and G. Lu, "Experimental study of the out-of-plane dynamic compression of hexagonal honeycombs," vol. 94, no. 8, pp. 2326–2336.

[95] M. Wang, D. Shan, Y. Liao, and L. Xia, "Investigation of inelastic behavior of elastomeric composites during loading–unloading cycles," vol. 75, no. 2, pp. 561–568.

[96] S. R. G. Bates, I. R. Farrow, and R. S. Trask, "3d printed polyurethane honeycombs for repeated tailored energy absorption," vol. 112, pp. 172–183.

[97] B. Hu, M. Li, J. Jiang, and W. Zhai, "Development of microcellular thermoplastic polyurethane honeycombs with tailored elasticity and energy absorption via CO2 foaming," vol. 197, p. 106324.

[98] S. Townsend, R. Adams, M. Robinson, B. Hanna, and P. Theobald, "3d printed origami honeycombs with tailored out-of-plane energy absorption behavior," vol. 195, p. 108930.

[99] S. Potta and C. D, "Modeling and optimization of sustainable manufacturing process in machining of 17-4 PH stainless steel," vol. 134.

[100] A. Di Bucchianico, "Coefficient of determination (r2)," in *Encyclopedia of Statistics in Quality and Reliability*, John Wiley & Sons, Ltd. _eprint: https://onlinelibrary.wiley.com/doi/pdf/10.1002/9780470061572.eqr173.

7 Appendices

7.1 Parametric Design Models

7.1.1 Model: Sheet A

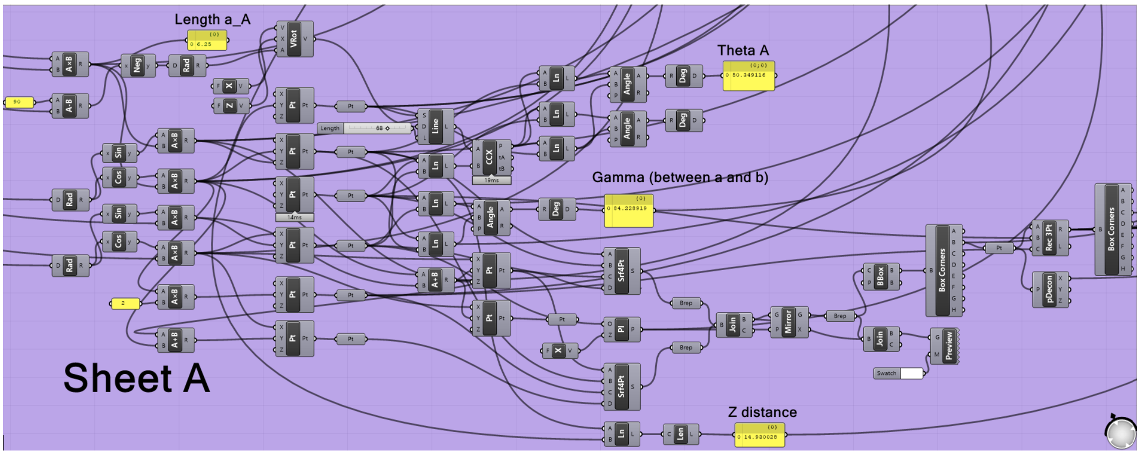

Figure 52: Generation of sheet A within parametric model.

7.1.2 Model: Sheet B

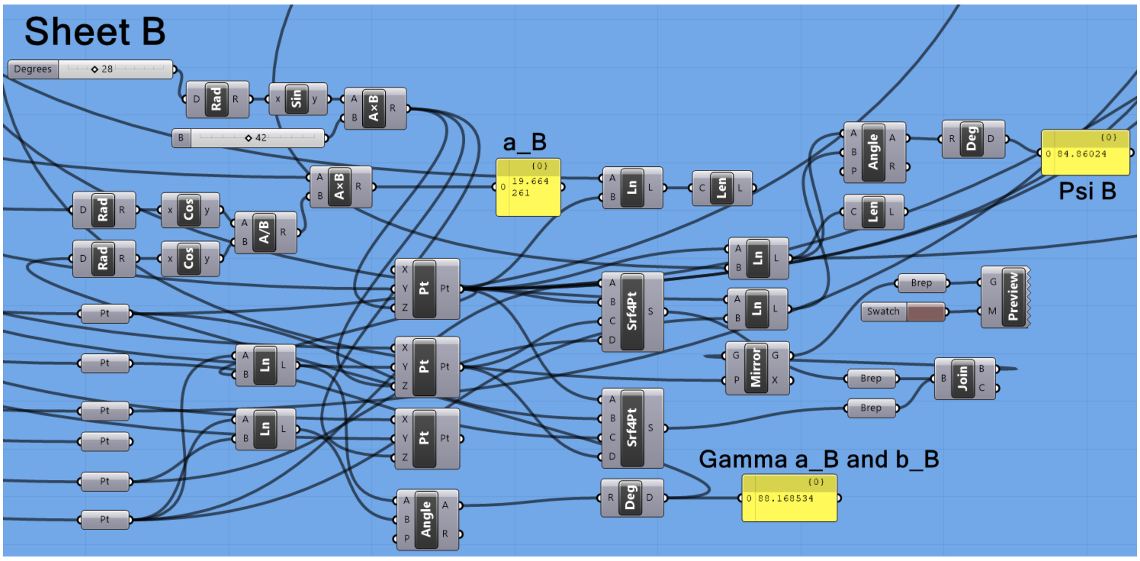

Figure 53: Generation of sheet B within parametric model.

7.1.3 Model: MOM Generation

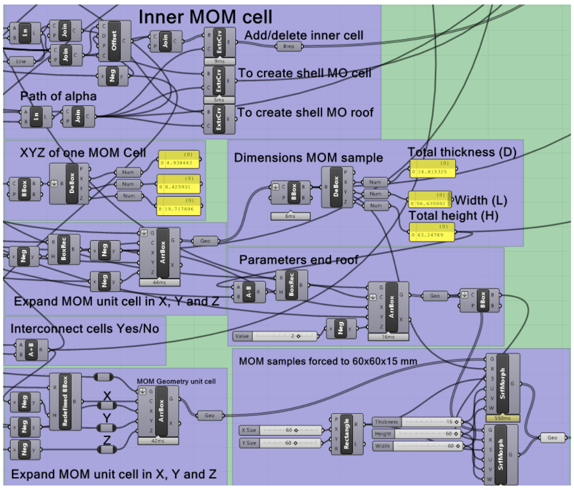

Figure 54: Generation of MOM structure within parametric model.

7.1.4 Model: Analysis and Validation of Geometry Parameters

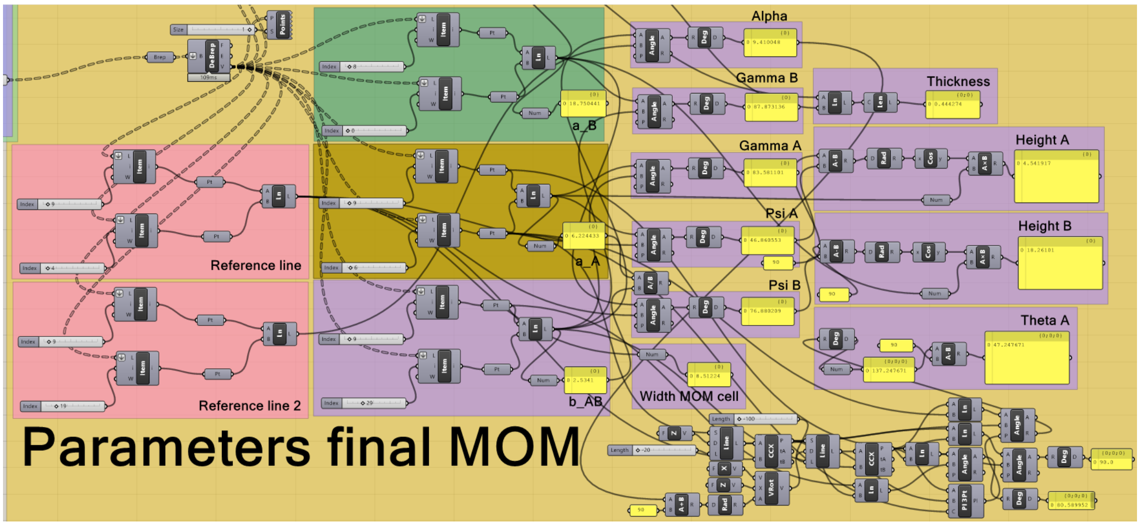

Figure 55: Sub-model that is responsible for analysing the geometry parameters.

7.1.5 Model: Morphing the MOM Structure onto the Helmet Liner

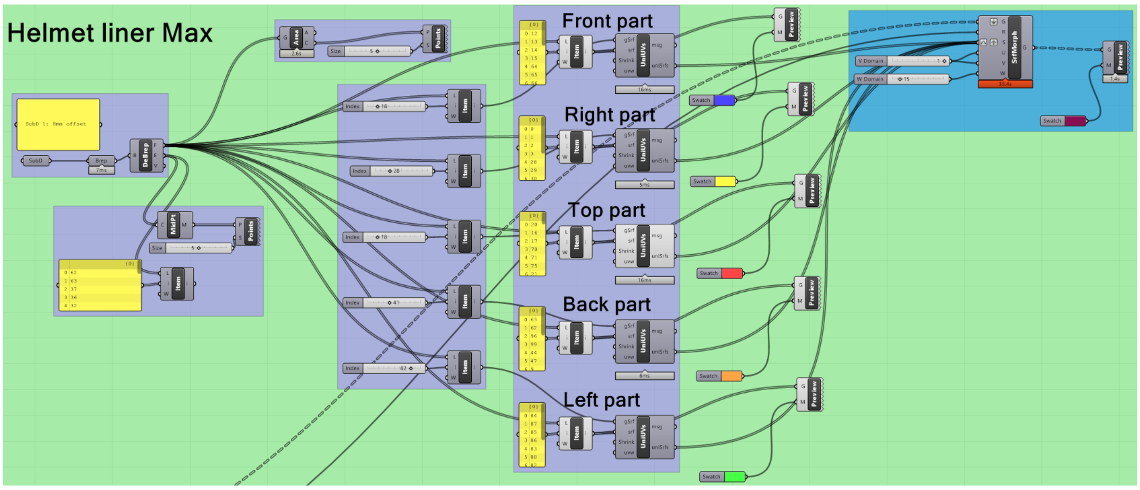

Figure 56: Sub-model that is responsible for dividing the helmet liner in individual surfaces after which their axes are unified. Also, responsible for the surface morphing.

7.1.6 Complete Model

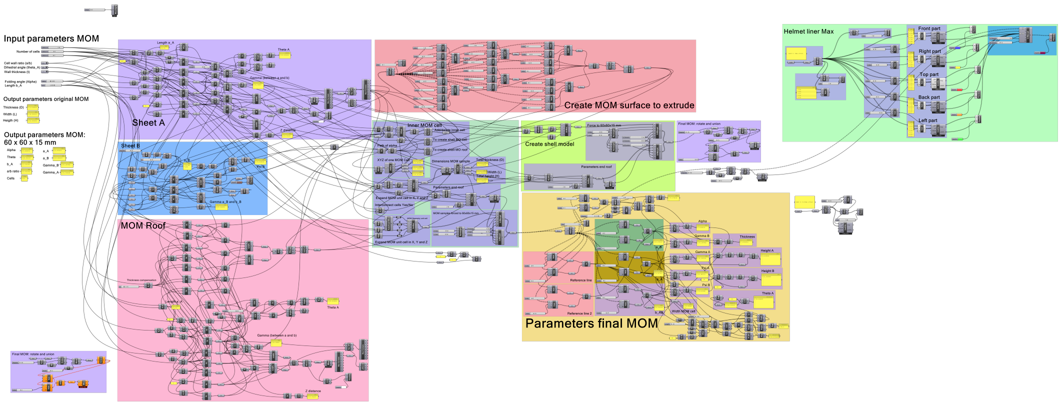

Figure 57: The complete Grasshopper model including all the sub-models.

7.2 Creatily Ender Pro 5

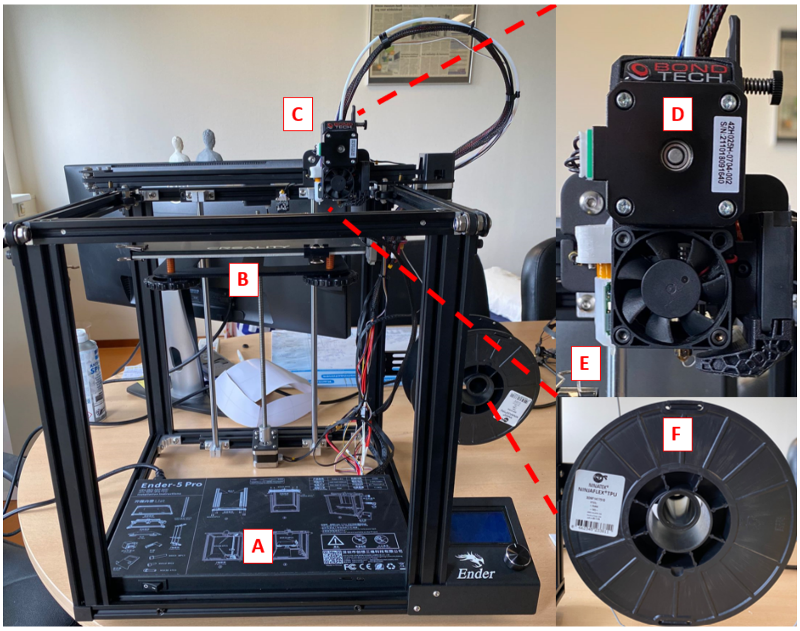

Figure 58: The complete FDM setup including the frame [a], the heated printing bed [b], the direct drive system [c], BondTech DDX V3 [d], the BLTouch autoleveler [e] and the filament spool [f].

7.3 3D Printed Miura-Ori Metamaterial Structures

7.3.1 Average thickness and weight of all 27 samples

Table 27: Overview of all 27 samples that have been quasi-static compressed.

Sample	**Avg. t [mm]**	**Weight [g]**	**EA [J]**	**SEA [J/kg]**
1.1	0.44	8.88	0.021	2.364
1.1	0.42	8.82	0.019	2.317
1.3	0.48	9.15	0.025	2.732
2.1	0.45	7.9	0.017	2.152
2.2	0.43	7.67	0.014	1.825
2.3	0.43	7.7	0.0145	1.883
3.1	0.49	9.17	0.0165	1.799
3.2	0.48	9.01	0.0145	1.609
3.3	0.48	9.07	0.015	1.687
4.1	0.77	11.7	0.042	3.589
4.2	0.72	10.9	0.04	3.669
4.3	0.74	11	0.041	3.727
5.1	0.76	12.82	0.052	4.056
5.2	0.78	12.95	0.045	3.474
5.3	0.81	13.3	0.06	4.511
6.1	0.82	20.6	0.09	4.369
6.2	0.81	20.1	0.085	4.229
6.3	0.77	19	0.07	3.684
7.1	1.03	14.9	0.09	6.040
7.2	0.99	14.5	0.084	5.793
7.3	0.98	14.1	0.08	5.673
8.1	1.1	25.15	0.24	9.542
8.2	1.08	24.3	0.21	8.642
8.3	1.06	23.95	0.2	8.351
9.1	1.15	23.1	0.017	7.359
9.2	1.06	21.9	0.015	6.849
9.3	1.10	22.35	0.0158	7.069

7.3.2 Energy Absorption Diagrams

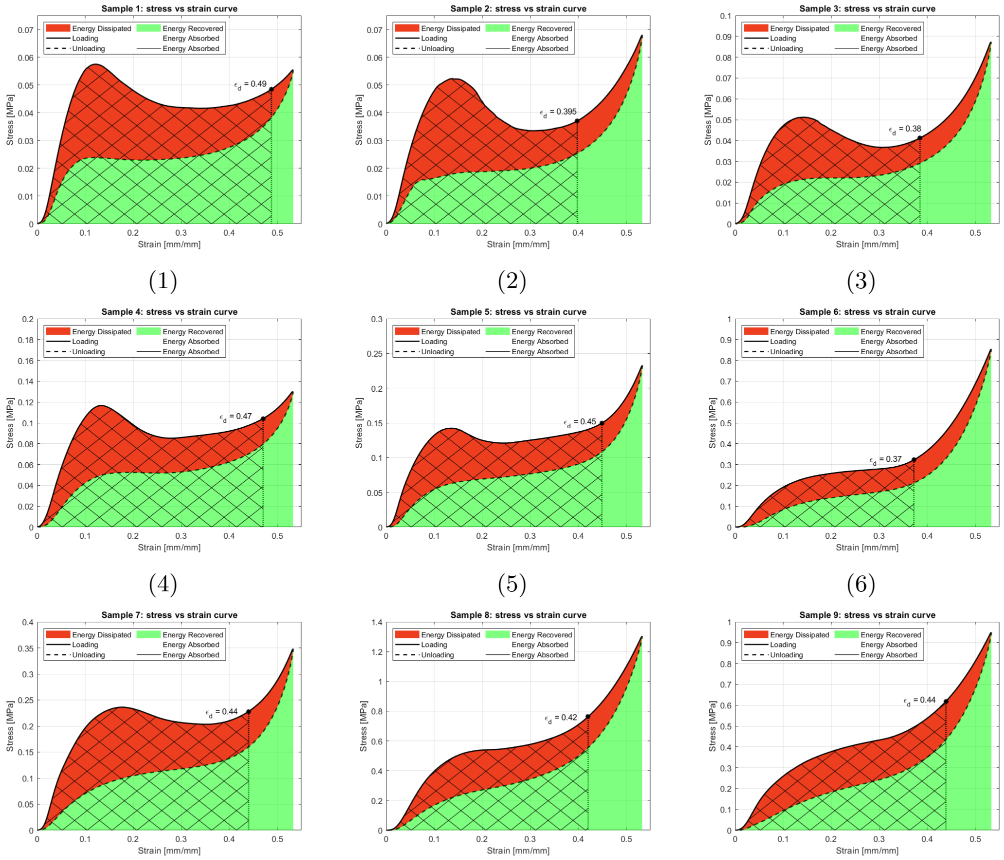

(1) (2) (3)

(4) (5) (6)

(7) (8) (9)

Figure 59: Final result of the energy absorption diagrams per sample 1 -9, including the hysteresis, energy dissipated (red) and energy recovered (green). Numbering is according to the sample number 1 - 9.

7.4 Deformation mechanisms of all samples

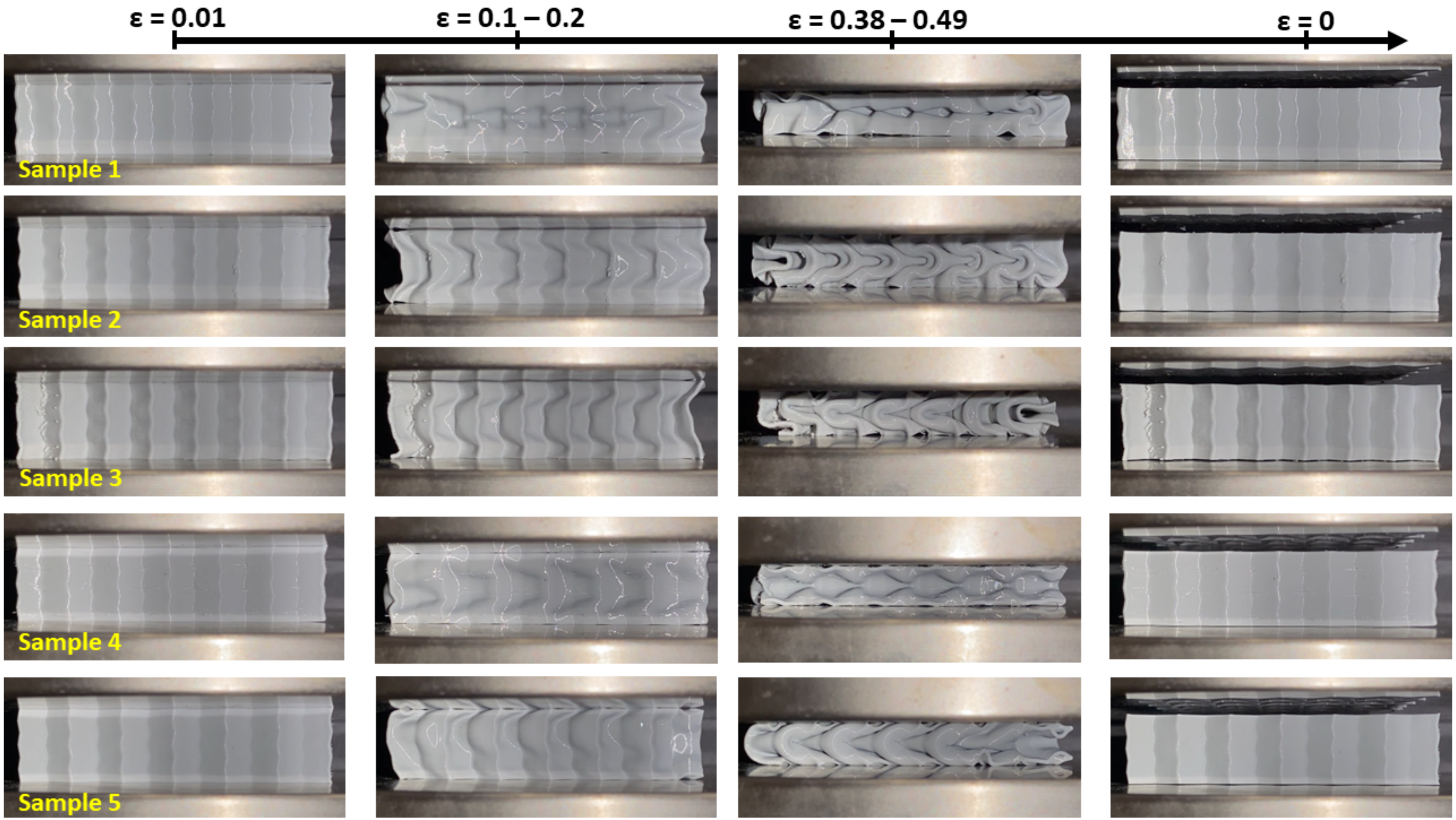

Figure 60: Overview of samples 1 to 5 with their deformation patterns at the preload, cell wall buckling and densification.

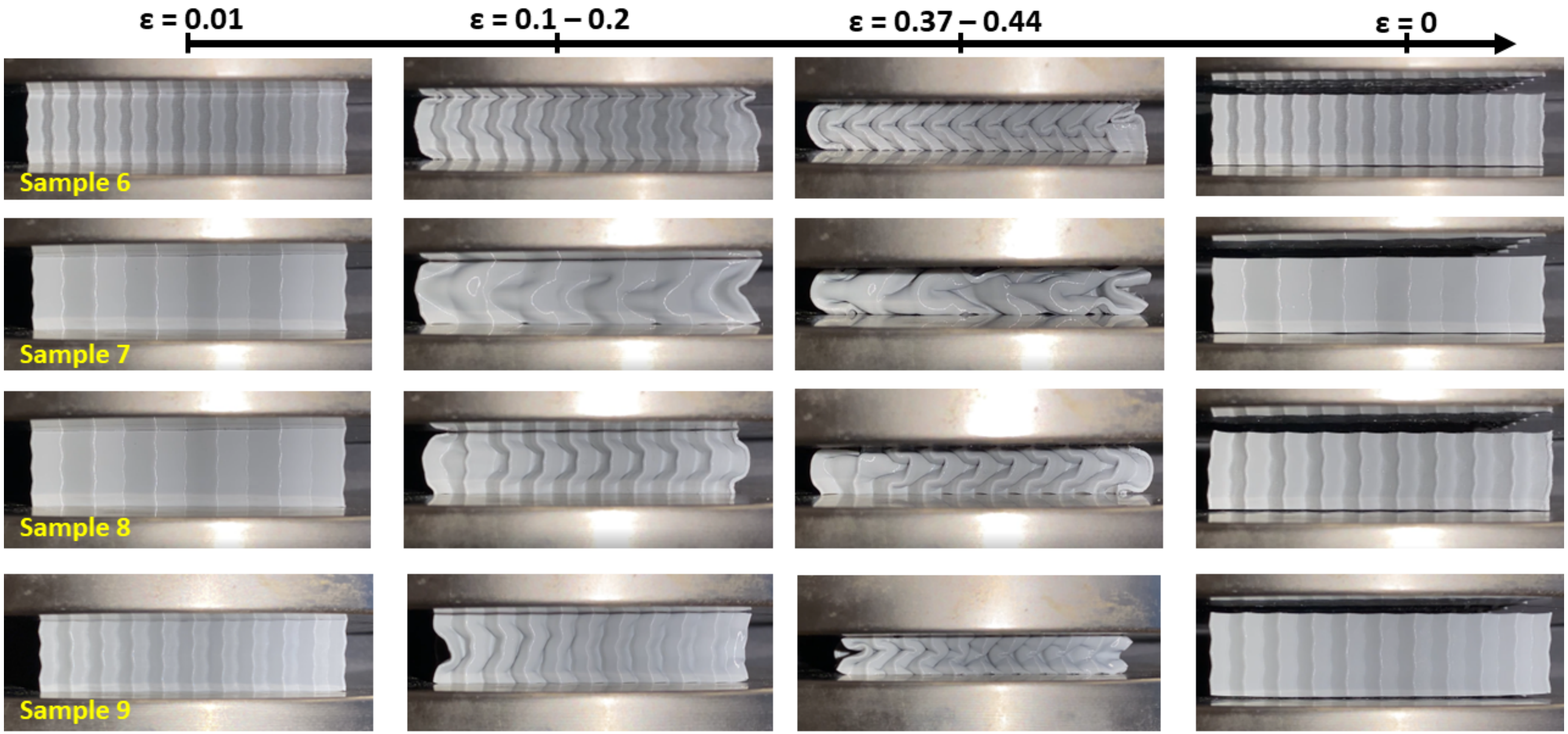

Figure 61: Overview of samples 6 to 9 with their deformation patterns at the preload, cell wall buckling and densification.